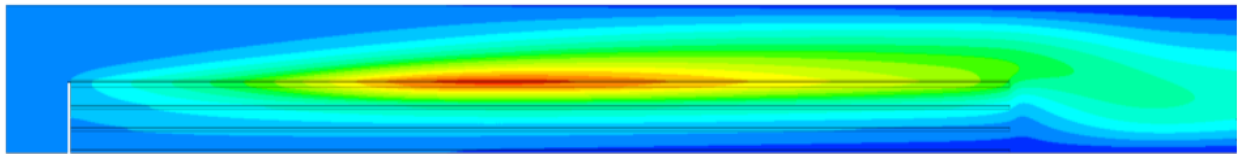




CHALMERS
UNIVERSITY OF TECHNOLOGY



Thermal control of a lab-scale in-situ reactor for soot oxidation

Cross-divisional Master's thesis in Applied Mechanics

ANNIKA BIRO
REBECCA ERIKSSON

MASTER'S THESIS 2016:55

**Thermal control of a lab-scale
in-situ reactor for soot oxidation**

Cross-divisional Master's thesis in Applied Mechanics

ANNIKA BIRO
REBECCA ERIKSSON



CHALMERS
UNIVERSITY OF TECHNOLOGY

Department of Applied Mechanics
Division of Combustion and Division of Fluid Dynamics
CHALMERS UNIVERSITY OF TECHNOLOGY
Gothenburg, Sweden 2016

Thermal control of a lab-scale in-situ reactor for soot oxidation
Cross-divisional Master's thesis in Applied Mechanics
ANNIKA BIRO
REBECCA ERIKSSON

© ANNIKA BIRO, REBECCA ERIKSSON, 2016.

Supervisors:

Jonas Sjöblom, Division of Combustion
Henrik Ström, Division of Fluid Dynamics

Examiners:

Sven B. Andersson, Division of Combustion
Srdjan Sasic, Division of Fluid Dynamics

Master's Thesis 2016:55
Department of Applied Mechanics
Division of Combustion and Division of Fluid Dynamics
Chalmers University of Technology
SE-412 96 Gothenburg
Telephone +46 31 772 1000

Cover: Temperature contour plot for soot oxidation reaction in the reactor set-up for the open flow case simulations.

Typeset in L^AT_EX
Printed by Chalmers reproservice
Gothenburg, Sweden 2016

Thermal control of a lab-scale in-situ reactor for soot oxidation
Cross-divisional Master's thesis in Applied Mechanics
ANNIKA BIRO
REBECCA ERIKSSON
Department of Applied Mechanics
Chalmers University of Technology

Abstract

CFD simulations were coupled with lab-scale experiments to study steep temperature increases (thermal fronts) during thermal regeneration of a diesel particulate filter (DPF) via soot oxidation. The study investigated the conditions under which these fronts appear. A more well-defined open-flow system in contrast to a wall-flow system as in DPFs was used for practicality reasons.

An open-flow reactor was developed and soot oxidation experiments were carried out, using Printex-U and a synthetic gas mixture. Different operating conditions were used to provoke thermal fronts in the reactor. A peak of high temperature was observed, which is dependent on the conditions used.

Input data from the experiments was used to develop a 2D CFD model and verification was done via comparison with a numerical study. The validity of the model was assessed via the ability of the model to predict the temperature profile obtained from the experiments. Kinetic expressions for non-catalytic oxidation for both diesel soot and Printex-U were evaluated. The soot reaction rate in the simulations is found to be very sensitive to kinetic parameters. The obtained CFD model is able to predict soot oxidation at low reaction rates. However, at high reaction rates numerical instabilities occur due to large gradients in the domain. Reasons for this can be oversimplification of the soot layer, but also the use of a very large time step.

A thermal front that moves across the substrate during soot oxidation as reported by other studies (numerical and experimental) could not be obtained. It is found that oxygen depletion or soot depletion is needed in order to observe a moving thermal front which was not achieved under the experimental conditions used in this work. Mass transfer simulations suggest that mass transfer limitations are the main reason for this. Through coupling of the experimental and numerical results the placement of the thermocouples in the reactor is found to be very important to get a representative temperature measurement.

It is finally concluded that the open-flow configuration cannot be used to predict the behavior of a DPF configuration.

Keywords: Thermal fronts, Particulate Matter, Soot oxidation, DPF, Open flow substrate, 2D CFD model.

Acknowledgements

We would like to thank our supervisors Jonas Sjöblom and Henrik Ström for giving us the opportunity to work on this exciting and challenging cross-divisional project. We are very grateful for your continuous guidance and encouragement during our thesis as well as for the inspiring weekly discussions. It was most helpful that you were ready to help at any time and we feel that we learned a lot during this thesis. Also, we would like to express our gratitude to the staff of the combustion division for their great support during development of the experimental set-up; especially Robert Buadu, Timothy Benham, Alf Magnusson and Daniel Härensten. Finally, we thank our friends and family for their support and for always believing in us.

Annika Biro and Rebecca Kalembe Eriksson

Gothenburg, June 2016

Contents

List of Figures	xiii
List of Tables	xix
0.1 Abbreviations and symbols	xx
0.1.1 Abbreviations and chemical symbols	xx
0.1.2 Symbols	xx
1 Introduction	1
1.1 Background	1
1.1.1 Exhaust gas	2
1.1.2 Particulate matter	2
1.1.3 Synthetic soot	5
1.1.4 Particulate filters and regeneration	5
1.1.5 Intrinsic kinetics vs Global kinetics	8
1.2 Aim	8
1.3 Limitations	8
2 Theory	11
2.1 Experiments	11
2.1.1 Space Velocity	11
2.2 Simulation	12
2.2.1 Governing equations	12
2.2.2 Pressure drop and the porous media model	15
2.2.3 Determination of the viscous resistance coefficients	16
2.3 Soot oxidation kinetics	18
2.3.1 Soot oxidation reaction kinetics	18
2.3.2 Non-catalyzed soot oxidation kinetics	19
2.3.3 Catalyzed soot oxidation kinetics	20
2.4 Mass transfer effects	22
2.4.1 Mass transfer effects in monolithic reactors	22
2.4.2 Determination of Sherwood number from simulations	22
3 Methods	25
3.1 Experiments	25
3.1.1 Reactor and other equipment	25
3.1.2 General Experiment set-up	28
3.1.3 Leak proof test	29

3.1.4	Flow experiments	29
3.1.5	Soot oxidation experiments	30
3.1.6	DPF experiment	32
3.2	Simulation	33
3.2.1	Modelling of the gas mixture	33
3.2.2	Modelling of the influence of soot consumption on porosity and viscous resistance	33
3.2.3	Modelling of the soot oxidation reaction	36
3.2.4	Treatment of the heat release from the reaction	37
3.2.5	Preliminary simulation of Sarli and Benedetto (2015) for ver- ification of the model	38
3.2.6	Development of a 2D open flow model	41
3.2.7	Mass transfer effects in the reactor	43
4	Results and Discussion	45
4.1	Experimental results	45
4.1.1	Soot experiment 1	45
4.1.2	Soot experiment 2	49
4.2	Reproduction of the 2D model of Sarli and Benedetto (2015)	50
4.2.1	Analysis of the flow field	50
4.2.2	$k_s = 1$ and $k_s = 0$	51
4.2.3	$k_s = 5$	52
4.3	The 2D open flow model	56
4.3.1	Simulation of soot oxidation experiment 1	56
4.3.2	Mass transfer effects	63
5	Conclusion and outlook	71
	Bibliography	75
A	Appendix A	I
A.1	Thermocouples	I
A.1.1	Zero degree calibration	I
A.1.2	100 degree calibration	I
A.2	Mass flow controllers	II
A.3	CO ₂ /CO gas analyzers	III
A.3.1	Calibration procedure CO/CO ₂ analyzer	IV
B	Appendix B	VII
B.1	Experimental set-up description	VII
C	Appendix C	XVII
C.1	Result from the flow experiments	XVII
D	Appendix D	XXI
D.1	Calculation for mass of soot used	XXI
E	Appendix E	XXIII

E.1	Calculation for gas mixture flow rate	XXIII
F	Appendix F	XXV
F.1	Results from the DPF experiment	XXV
G	Appendix G	XXVII
G.1	Gas mixture thermal conductivity	XXVII
G.2	Gas mixture viscosity	XXVII
H	Appendix H	XXIX
H.1	Additional graphs soot experiment 1	XXIX
I	Appendix I	XXXIII
I.1	Resulting plots from experiment 3	XXXIII
J	Appendix J	XXXV
J.1	Sherwood number calculation	XXXV
J.1.1	0.7408 m/s case	XXXV
J.1.2	15.3 m/s case	XXXVI
J.1.3	0.224 m/s case	XXXVII
K	Appendix K	XXXIX
K.1	Space Velocity calculation for open flow case	XXXIX

List of Figures

1.1	The diesel particulate filter is part of the exhaust gas after-treatment (EATS) of e.g. trucks with an heavy duty diesel engine. Other devices in the EATS are represented as empty boxes since they will not be considered further in this thesis. In the lower part of the picture it is shown that the filter is a monolith that has many small channels that are alternately blocked at the ends.	1
1.2	Structure of a diesel particle (adapted from Van Setten et al. (2001))	3
1.3	Engine exhaust particle size distribution showing mass and number based concentration (Van Setten et al., 2001)	4
1.4	Example of an integrated DPF in the exhaust after-treatment (adapted from Konstandopoulos and Papaioannou (2008)). DOC is a diesel oxidation catalyst and DeNOx is a nitrogen oxide removal device. . . .	5
1.5	Principle of a wall-flow monolith	6
3.1	200 /12 cpsi codierite monolith and zoomed-in view of channels in the monolith.	26
3.2	Reactor view from the outlet. The steel casing is 12 mm x 12 mm x 153 mm and the dimensions of the cut monolith substrate inside are 153 mm(= 6 in) x 12 mm x 6 mm.	26
3.3	Front view of the oven	27
3.4	Flow diagram showing the insulated experimental set-up.	28
3.5	Thermocouple placement in the substrate outlet	28
3.6	Thermocouple placement view from side and bottom of the reactor. The red arrow indicates the flow direction.	29
3.7	Soot applied on the top surface of the substrate. No soot is put into the channels.	31
3.8	Viscous resistance against porosity for the cake	35
3.9	Viscous resistance against porosity for the filter	36
3.10	Schematic drawing of the geometry for the preliminary simulation after Sarli and Benedetto (2015)	38
3.11	Monitor points for recording the temperature in the cake and in the filter made in accordance with Sarli and Benedetto (2015). The points are where the crosses are, where f stands for filter and c stands for soot cake.	40
3.12	Scheme of the model geometry for the experiments	41

3.13	Monitor points for recording the temperature in the substrate. The points are in the middle of the crosses and they correspond to the thermocouple placement in the experiments.	42
4.1	Temperature measured during soot oxidation in experiment 1. Note that there are axial differences in temperature also at the start of the soot oxidation. They show the same pattern and are about the same magnitude as after the soot oxidation (around 600 s).	47
4.2	Relative temperature increase during soot oxidation in experiment 1 .	48
4.3	Production of CO and CO ₂ during soot oxidation in experiment 1 (Peak for CO reconstructed)	48
4.4	Temperature measured during soot oxidation in experiment 2. Only a part of the data is shown to highlight the peaks at the start of the soot oxidation when oxygen is turned on (at approx. 180 s).	49
4.5	Vectors of velocity coloured by velocity magnitude in <i>m/s</i> for the preliminary simulation (scaled in y direction). Red is high velocity, blue is low velocity.	50
4.6	Plot of temperature predicted in the wall of the filter vs time for case $k_s = 1$. Reproduced temperature plot (left) and temperature plot reported by Sarli and Benedetto (2015) (right)	51
4.7	Soot conversion vs flow time for $k_s=1$ and $k_s=0$ case. Reproduced soot conversion plots (left) and and soot conversion plots reported by Sarli and Benedetto (2015) (right)	52
4.8	Temperature registered at the monitor points in the filter for $k_s = 5$ case, using an explicit formulation of the source term, with temperature limited to 1300 K and updating the flow field every ten time steps.	53
4.9	Contour plots for temperature and oxygen mass fraction for $k_s = 5$ case.	53
4.10	Soot conversion calculated from soot mass concentration registered at the monitor points in the filter and cake for $k_s = 5$ case, using an explicit formulation of the source term, with temperature limited to 1300 K and updating the flow field every 10 time steps.	54
4.11	Vectors of velocity coloured by velocity magnitude in <i>m/s</i> for the simulation of the soot oxidation experiment 1 (domain scaled in y direction). A zoomed in version of the inlet (left) and outlet (right) is also given. Red indicates highest velocity and dark blue is lowest. .	57
4.12	Temperature (in °C) predicted at the monitor points in the substrate (T _c) during soot oxidation simulation using Diesel soot kinetics . . .	58
4.13	Temperature (in °C) predicted at the monitor points in the substrate (T _c) during soot oxidation simulation using Printex-U kinetics (left) and temperature measured during the experiments (right).	60
4.14	Mass concentration of soot as registered in monitor points in the soot cake (C) during soot oxidation simulation using Printex-U kinetics . .	61
4.15	Reaction rate in the cake along the substrate length plotted for different points in time.	61

4.16	Contour plots for temperature (in K) and O ₂ concentration in the first two seconds of flow. It can be seen that at 1 s the soot is already reacting homogeneously along the substrate length.	62
4.17	Contour plots for temperature (in K) and O ₂ concentration for different points in time. Note the different scale in comparison to the previous picture. The red zone in the temperature plot for 25 s represents all temperature above 1200 K; the highest obtained temperature is 1673 K and is situated in the middle of the substrate.	63
4.18	Contour plot showing the fully developed velocity profile in the 0.7408 ms^{-1} steady state simulation case. The red zone in the contour plot represents the highest velocity (2.17 ms^{-1}) while the dark blue zone represents zero velocity.	65
4.19	Contour plot showing flow field of O ₂ in the 0.7408 ms^{-1} steady state simulation case. The red zone in the contour plot represents maximum mass fraction of oxygen (0.168) while the dark blue zone represents the lowest oxygen mass fraction (0.0)	65
4.20	Contour plot showing flow field of O ₂ at the inlet during the 0.7408 ms^{-1} steady state simulation case. The red zone in the contour plot represents maximum mass fraction of oxygen (0.168) while the dark blue zone represents the lowest oxygen mass fraction (0.0)	65
4.21	Contour plot showing flow field of O ₂ at the outlet during the 0.7408 ms^{-1} steady state simulation case. The red zone in the contour plot represents maximum mass fraction of oxygen (0.168) while the dark blue zone represents the lowest oxygen mass fraction (0.0)	65
4.22	Contour plot showing the developing velocity profile in the 15.3 ms^{-1} steady state simulation case. The red zone in the contour plot represents the highest velocity (52.98 ms^{-1}) while the dark blue zone represents zero velocity.	67
4.23	Contour plot showing the flow field of O ₂ developed in the 15.3 ms^{-1} steady state simulation case. The red zone in the contour plot represents maximum mass fraction of oxygen (0.168) while the dark blue zone represents the lowest oxygen mass fraction (0.0).	67
4.24	Contour plot showing flow field of O ₂ at the inlet in the 0.7408 ms^{-1} steady state simulation case. The red zone in the contour plot represents maximum mass fraction of oxygen (0.168) while the dark blue zone represents the lowest oxygen mass fraction (0.0).	67
4.25	Contour plot showing mass fraction of O ₂ at the outlet during the 15.3 ms^{-1} steady state simulation case. The red zone in the contour plot represents maximum mass fraction of oxygen (0.168) while the dark blue zone represents the lowest oxygen mass fraction (0.0).	67
4.26	Contour plot showing the fully developed velocity profile in the 0.224 ms^{-1} steady state simulation case. The red zone in the contour plot represents the highest velocity (0.665 ms^{-1}) while the dark blue zone represents zero velocity.	68

4.27	Contour plot showing the flow field of O ₂ developed during the 0.224 $m.s^{-1}$ steady state simulation case. The red zone in the contour plot represents maximum mass fraction of oxygen (0.168) while the dark blue zone represents the lowest oxygen mass fraction (0.0).	68
4.28	Contour plot showing the flow field of O ₂ developed at the inlet during the 0.224 $m.s^{-1}$ steady state simulation case. The red zone in the contour plot represents maximum mass fraction of oxygen (0.168) while the dark blue zone represents the lowest oxygen mass fraction (0.0).	69
4.29	Contour plot showing the flow field of O ₂ developed at the outlet during the 0.224 $m.s^{-1}$ steady state simulation case. The red zone in the contour plot represents maximum mass fraction of oxygen (0.168) while the dark blue zone represents the lowest oxygen mass fraction (0.0).	69
A.1	Working principle Mass-flow controller (Bronkhorst, 2016)	II
B.1	Assembling of the experimental set-up at the inlet	VIII
B.2	Thermocouple inserted and fastened at the the thermocouple entrance.VIII	
B.3	Thermocouple placement in the substrate outlet	IX
B.4	Thermocouple placement view from side and bottom of the reactor. The red arrow indicates the flow direction.	IX
B.5	Thermocouple in the reactor outlet holder adjusted to different lengths. X	
B.6	Reactor substrate inserted into the reactor outlet holder.	X
B.7	Reactor substrate inserted into the reactor casing	XI
B.8	Thermocouple entrance at the outlet(top) and inlet(bottom)	XII
B.9	Reactor set up fastened and glued to the reactor holders with reactor surface thermocouples attached	XII
B.10	Reactor set up at the inlet	XIII
B.11	Reactor set up with all thermocouples attached	XIV
B.12	Reactor set up with all thermocouples attached including view of oven and Lab-view box	XIV
B.13	Insulated reactor set-up	XV
B.14	Flow diagram showing the experiment set-up used	XVI
C.1	Pressure drop flow experiment	XVII
C.2	Temperature flow experiment	XVIII
C.3	Zoomed temperatures for flow experiment, showing radial and axial differences	XIX
D.1	Side view of one filter showing inlet/outlet channels (top), back view of inlet/outlet channels (bottom)	XXI
F.1	Temperature plots for thermocouples in a DPF substrate	XXV
F.2	Pressure drop in a DPF substrate. The sensor was broken so that the reading is erroneous for this experiment. However it can be seen as a qualitative result.	XXVI

H.2	Ratio $\text{CO}/(\text{CO}+\text{CO}_2)$ taken between 147 and 360 seconds during soot oxidation and average.	XXIX
H.1	Development of the axial temperature profile during the thermal front	XXX
H.3	Pressure drop measured during soot oxidation (plot starts after the correct synthetic air concentration is reached, before the pressure drop is constant around 615 Pa).	XXXI
I.1	Pressure drop during soot oxidation in experiment 3	XXXIII
I.2	Temperature during soot oxidation in experiment 3	XXXIV
I.3	CO and CO_2 during soot oxidation in experiment 3	XXXIV

List of Tables

1.1	Exemplary composition of diesel soot particle from a heavy duty diesel engine during heavy duty transient cycle (adapted from Kittelson (1998))	4
2.1	Parameters for non catalyzed Diesel soot oxidation (Darcy et al., 2007) and non catalyzed Printex-U oxidation (Neeft et al., 1997) . . .	19
2.2	Parameters for slow soot oxidation described by Darcy et al. (2007) .	20
2.3	Parameters for fast soot oxidation as described by Darcy et al. (2007)	21
3.1	Experiment conditions used for different soot oxidation experiment runs conducted	30
3.2	Values for viscous resistance, permeability, initial porosity, porosity after oxidation and grain size/pore size for soot cake and filter	35
3.3	Mesh parameters and mesh quality aspects for the preliminary simulation.	38
3.4	Solid material properties for the preliminary simulation (Sarli and Benedetto (2015))	39
3.5	Inlet boundary conditions and initial conditions from Sarli and Benedetto (2015). Velocity is given at inlet temperature 813 K while SV is given at standard conditions	39
3.6	Mesh parameters and mesh quality aspects for the simulations of the experiment	41
3.7	Solid properties cordierite	42
3.8	Inlet and initial conditions used in the steady state simulation	43
A.1	Temperature correction factors for thermocouples for $0^{\circ}C$ reading . .	II
A.2	Temperature correction factors for thermocouples for $100^{\circ}C$ reading	II

0.1 Abbreviations and symbols

0.1.1 Abbreviations and chemical symbols

Abbreviation	Meaning
CO	Carbon monoxide
CO ₂	Carbon dioxide
CFD	Computational fluid dynamics
DOC	Diesel oxidation catalyst
DeNO _x	Device to remove nitrogen oxides
DPF	Diesel particulate filter
EATS	Exhaust after-treatment system
H ₂ O	Water
HC	Gaseous hydrocarbons
MFC	Mass flow controller
N ₂	Nitrogen
NH ₃	Ammonia
NO _x	Nitrogen oxides (nitrogen oxide NO and nitrogen dioxide NO ₂)
O ₂	Oxygen
PM	Particulate matter
SiC	Silicon carbide

0.1.2 Symbols

Symbol	Meaning
A	Pre-exponential factor
a	Reaction order of oxygen
A_{shell}	Area of cake layer
α	Permeability
b	Reaction order of carbon
β	Forchheimer coefficient
C	Concentration
C_2	Inertial resistance factor
C_{MFC}	Conversion factor
c_p	Specific heat capacity
D_{AB}	Binary diffusion coefficient
d_h	Hydraulic diameter
$D_{i,m}$	Mass diffusivity of species i in mixture m
d_p	Grain diameter/Pore size
D_T	Thermal diffusion coefficient
ΔP	Pressure drop
E	Total energy
E_a	Activation energy
ϵ	Porosity
F	Molar flow rate
$f_w(\epsilon)$	Hydrodynamic interaction function

Symbol	Meaning
$f(x_{O_2})$	Function for dependency of soot oxidation reaction on oxygen partial pressure
$g_w(\epsilon)$	Correction factor for mass transfer to a single particle
$\Delta_f H_R^0$	Heat of reaction
$\Delta_f H^0$	Heat of formation of reactants/products
\vec{J}_i	Diffusive mass flux
k	Thermal conductivity
K	Kuwabara's hydrodynamic factor
k_c	Mass transfer coefficient
k_{eff}	Effective thermal conductivity
k_f	Thermal conductivity fluid
K_{MFC}	Constant for gases in the MFC
Kn	Knudsen number
k_r	Reaction rate constant
k_{solid}	Thermal conductivity solid
k_s	Factor for theoretical kinetic study of Sarli and Benedetto (2015)
Le	Lewis number
m	Mass
μ	Fluid viscosity
MW	Molecular weight of the gas mixture
N	Diffusive flux
N_{AS}	Total number of active carbon sites
n_i	Thickness of the porous zone in the model in the i th direction
p	Pressure
Ψ_m	Mass flow rate
Q	Volumetric flow rate
q	Transferred heat
r	Reaction rate
R	Gas rate constant
R_c	Radius of a spherical unit collector
R_2	Radius of the boundary around a spherical unit collector
R_i	Net rate of production of species through chemical reaction
r_p	Particle radius
ρ	Density
ρ_f	Fluid density
ρ_s	Solid density
s	Surface concentration of carbon active sites
S_a	Total surface area
$S_{a,0}$	Initial surface area
SCF	Stokes Cunningham factor
Sh	Sherwood number
S_h	Energy source term

Symbol	Meaning
S_i	Source term for addition of species due to dispersed phase or external sources
S_m	Mass source term
S_{mom}	Momentum source term
SV	Space velocity
T	Temperature
$\bar{\tau}$	Stress tensor
v	Velocity
$ v $	Velocity magnitude
ν_i	Atomic diffusion volume of species i
V	Volume
V_{signal}	Voltage signal
VF	Volume fraction
w	Filter wall thickness
x_{O_2}	Partial pressure of oxygen
Y_i	Local mass fraction of species i
Z	Instantaneous mass concentration of soot
Z_0	Initial mass concentration of soot
$Z_{total,0}$	Initial total mass concentration of soot
$Z_{total,t}$	Total mass concentration of soot at time t

1

Introduction

1.1 Background

Exhaust gas from internal diesel engine combustion has been reported to contain particulate matter (PM) as one of the products from incomplete combustion. Emissions from the tail pipe of the engine therefore release PM among other pollutants to the atmosphere that have adverse effects to both the environment and human health. PM of particle size smaller than 2.5 microns penetrates deep into the lungs on inhalation where they deposit. Therefore exposure to this fine PM results into various heart and lung related health problems such as lung cancer, decreased lung function in children and asthma among others. In addition, PM affects air quality since it reacts with ozone in the atmosphere to form smog thus resulting into decreased visibility (EPA, 2001; Bennett, 2010; UNEP, 2009).

Due to these negative aspects attributed to PM, its emission to the atmosphere has to be reduced. This is achieved through the use of diesel particulate filters (DPF) in exhaust gas after treatment.

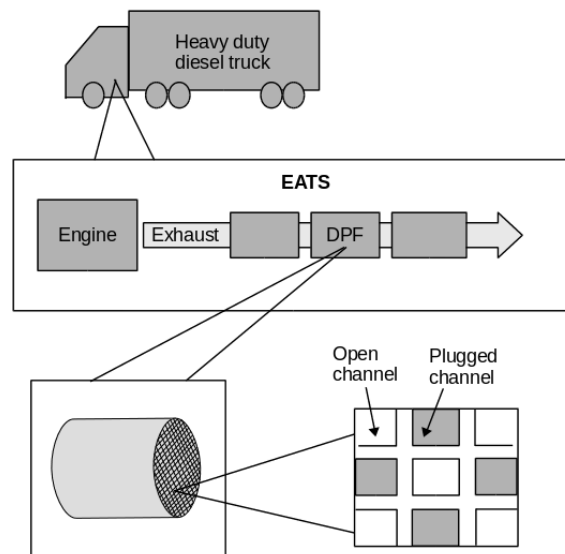


Figure 1.1: The diesel particulate filter is part of the exhaust gas after-treatment (EATS) of e.g. trucks with an heavy duty diesel engine. Other devices in the EATS are represented as empty boxes since they will not be considered further in this thesis. In the lower part of the picture it is shown that the filter is a monolith that has many small channels that are alternately blocked at the ends.

DPFs are ceramic monolithic reactors made up of thousands of square parallel channels that filter out and trap PM from exhaust gas (see Figure 1.1). The trapped PM accumulates in the filter resulting into an increase in the pressure drop across the filter. This increases back-pressure of the diesel engine thus reducing its efficiency. The filter therefore is regenerated through soot oxidation in order to decrease pressure drop. The exhaust gas temperature of diesel engines is generally not high enough for complete soot oxidation; in order to achieve complete soot oxidation either the temperature in the filter is increased (active regeneration), or catalysts are used to lower the ignition temperature of the soot (passive regeneration). In many diesel engines a combination of both methods is used (Konstandopoulos et al., 2000).

If the regeneration rate of the filter is not high enough, soot accumulates in the filter. This affects engine performance leading to uncontrolled regeneration characterised by rapid combustion of the soot in the overloaded filter. During this event thermal fronts of high temperature can appear, which can be moving upstream and/or downstream in the filter. These may cause local peaks of high temperature which may compromise the durability of the DPF due to thermal stress and possible destruction of the catalyst. The appearance of the thermal fronts is dependent on the operating conditions of the filter, for example on soot loading, flow rate, oxygen concentration as well as temperature and catalyst activity. A good control system is therefore required to avoid too high temperatures and still achieve fast regeneration of the filter (Koltzakis et al., 2007; Van Setten et al., 2001; Chen et al., 2009).

In order to design the control system, models are required to accurately predict the temperature in the filter during regeneration. In this study therefore, a mathematical model that can predict the temperature profile developed during DPF regeneration will be developed.

1.1.1 Exhaust gas

Exhaust gas from the engine exiting at the tailpipe is formed as a result of combustion of the fuel (which is composed of mainly hydrocarbons) with the atmospheric air during engine operation. Depending on the air to fuel stoichiometric ratio, engine compression and engine ignition, this combustion will either produce toxic gases; CO, HC, NO_x or non toxic gases; O₂, H₂O, CO₂ or both (Hatch, 2012). The exhaust gas from a typical diesel engine also contains part of the rejected heat (28%) that was not originally converted to useful work by the engine (Bennett, 2009). The temperature for most heavy duty diesel engines exhaust gas is thus reported between 250 °C and 450 °C (Twigg, 2007).

1.1.2 Particulate matter

PM makes up the solid part of the exhaust gas. It is formed due to incomplete combustion of diesel fuel that occurs as a result of non-uniform mixing of the diesel fuel in air (Bennett, 2010). Diesel PM is made up of a low reactive carbonaceous part and the highly reactive organic fraction (Darcy et al., 2007). The latter which is also known as the Soluble Organic Fraction is soluble at exhaust gas temperatures higher than 350 °C. Furthermore, Van Setten et al. (2001) reports the diesel particle

to be composed of elemental carbon (also called primary soot particles) that have hydrocarbons, sulphuric acid droplets and inorganic ash adsorbed on their surface. The fraction of these components in the particle is dependent on fuel composition, engine (engine type, age and mode of operation) and fuel additives among others. Historically, the sulphuric acid droplets in the diesel particle originate from organic sulphur in the fuel. Sulphuric acid droplets and inorganic ash contribution in the diesel particle is lower in small engines as compared to big engines that are run on heavy fuel oil. Modern diesel fuels have very little sulphur levels with permitted fuel sulfur level at < 10 ppm in Europe. Therefore sulphur emission is no longer a big issue for road transportation emissions. However, the issue is still problematic on great oceans and in developing countries, such as China and Iran.

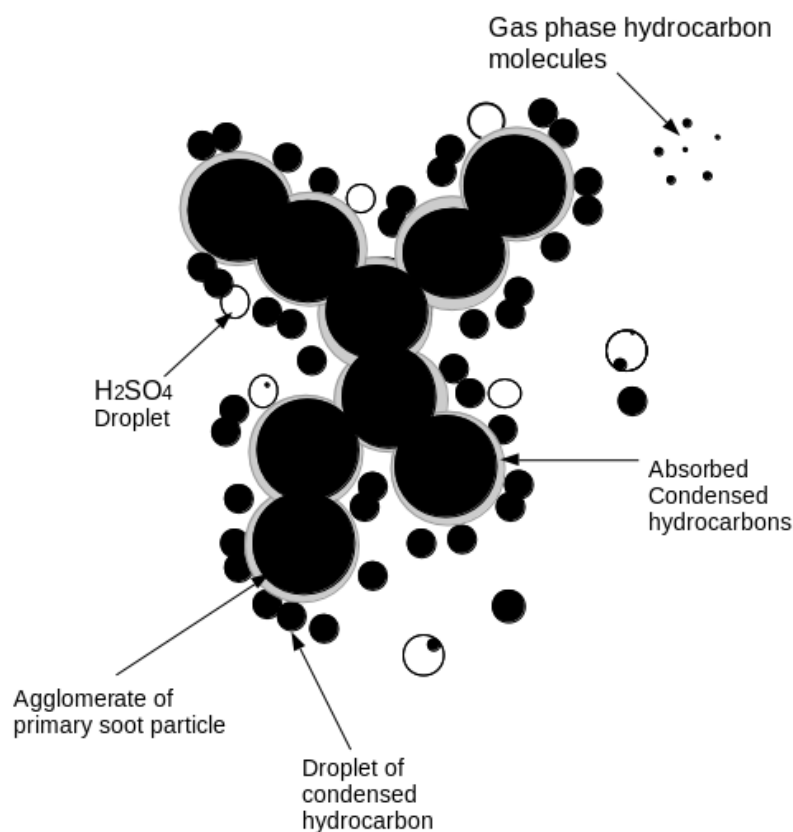


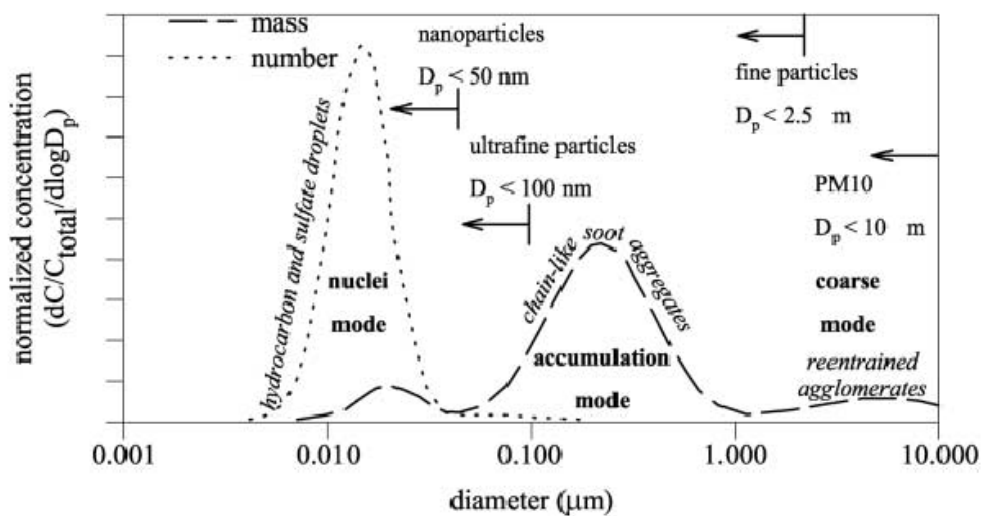
Figure 1.2: Structure of a diesel particle (adapted from Van Setten et al. (2001))

It is important to know both the composition and morphology of the diesel PM since these determine both the types of structures that form in the Diesel Particulate Filter (DPF) and the soot oxidation potential (Konstandopoulos and Papaioannou, 2008). The composition of diesel particles from a heavy duty diesel engine during heavy duty transient cycle is reported to contain mainly elemental or solid carbon; an example is shown in Table 1.1. This shows a complex mixture of inorganic and organic compounds which may be found in either gaseous or solid phase (Kittelson, 1998).

Table 1.1: Exemplary composition of diesel soot particle from a heavy duty diesel engine during heavy duty transient cycle (adapted from Kittelson (1998))

Carbon	Unburnt oil	Sulphate and water	Ash and others	Unburnt fuel
41 %	25%	14%	13%	7%

Exhaust particulate emissions have a broad size distribution: they are reported to be a mixture of relatively large particles in the coarse mode (diameter $> 10 \mu\text{m}$), fine particles (diameter $< 2,5 \mu\text{m}$), ultra fine particles (diameter $< 0.1 \mu\text{m}$) and finally nanoparticles (diameter $< 50 \text{ nm}$). Figure 1.3 shows a typical particle size distribution weighted by both number of particles and mass which is proportional to particle diameter. The different concentrations give two high peaks: a peak for the number of particles is obtained in the nucleation mode while a peak for mass concentration is obtained in the accumulation mode. The nucleation mode is characterised by a large number of fine particles and thus a high peak for the number concentration. These fine particles have a small diameter and thus low mass indicated by the low peak of mass concentration. In the accumulation mode however, particles become bigger in size due to surface growth and particle coagulation, furthermore, no nucleation occurs here, the accumulation mode is thus characterised by large particles (indicated by a peak in the mass concentration) that are few in number (indicated by a decrease in the number concentration). From this it is concluded that diesel PM is composed of numerous small particles having very little mass (as indicated by the peak of number distribution at nucleation mode), relatively large particles (indicated by the peak of mass distribution in the accumulation mode) and some coarse particles (Van Setten et al., 2001).

**Figure 1.3:** Engine exhaust particle size distribution showing mass and number based concentration (Van Setten et al., 2001)

1.1.3 Synthetic soot

The complex nature of diesel PM in terms of composition and size distribution has been presented. Because of this complexity, only the solid carbon content of PM is considered during mathematical modeling of diesel PM (Lakshminarayanan and Aghav, 2010). In addition, volatile components are disregarded during PM modelling since most of these volatile components are effectively removed from the exhaust gas by diesel oxidation catalysts upstream. Furthermore, the ash components are also omitted in the modelling of PM oxidation since they do not burn. Commercial model compounds of soot are therefore used to represent diesel soot during diesel soot oxidation experiments. An example of such commercial model compounds is Printex U; this is used since it has oxidation kinetics that are similar to soot. Printex-U is reported to be composed of elemental carbon, which takes up the largest percentage (93 %). The rest of the composition is made up of oxygen, hydrogen, nitrogen and sulphur. This is in contrast to diesel soot particles that could contain some ash (J. Jung and Chun, 2008). In this study, Printex-U is used as a model for soot; it is however referred to as 'soot' in this study.

1.1.4 Particulate filters and regeneration

Diesel particulate filters (DPFs) are part of the exhaust after-treatment system in vehicles and machines. A possible integration is shown in Figure 1.4: In this case the DPF is implemented between the diesel oxidation catalyst (DOC) and a NO_x removal device (DeNO_x). Here, the DOC removes carbon monoxide (CO), gas phase hydrocarbons and soluble organic fraction whereas the DeNO_x device removes nitrous oxides (DieselNet, 2012; Konstandopoulos and Papaioannou, 2008). These devices will not be further discussed since they are not the subject of this thesis. The exact implementation of a DPF depends on the method of particle removal and on the type of filter regeneration if required.

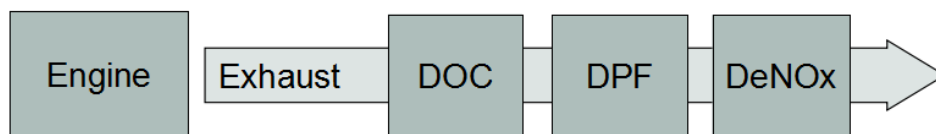


Figure 1.4: Example of an integrated DPF in the exhaust after-treatment (adapted from Konstandopoulos and Papaioannou (2008)). DOC is a diesel oxidation catalyst and DeNO_x is a nitrogen oxide removal device.

Particle removal

Particles can be removed from the exhaust gas by different methods. In flow-through catalysts the exhaust gas flows through an open monolith and the particles are oxidized by an oxidation catalyst deposited in the monolith channels. When using this method, sulphuric acid formation can be a problem, depending on the temperature of the exhaust gas. Hence, the type of catalyst used has to be tailored to the engine cycle at hand to avoid too high total particle mass leaving the system

due to formation of sulphuric acid droplets. A more common way is to trap the particles first using deep-bed filtration or surface-filtration. The difference between these two filtration methods lies in the pore size of the material. For deep bed filtration, ceramic foams and woven ceramic fibers with large pores or openings are often used, where the soot particles penetrate into the material and are trapped there (Van Setten et al., 2001). However, in most applications wall-flow monoliths (e.g. DPFs) are used which belong to the surface filtration methods. In wall-flow monoliths, the channels are alternately plugged at the end so that the flow has to move through the porous walls of the filter, as shown in Figure 1.5. Some particles penetrate into the filter wall, but some particles are too big to penetrate far into the material and are collected on the surface where they accumulate and form a layer. This soot layer is also formed because the filter wall has a limited capacity to take up soot. The layer is called soot cake and also acts as a filter itself. Wall-flow monoliths are very compact and have a high filtration efficiency due to trapping of the soot particles. They are typically made from cordierite or silicon carbide, where silicon carbide has better properties to withstand high temperatures in the filter. These two materials also differ in their production methods: Silicon carbide is composed of many granules that are pressed together whereas the pores in cordierite are produced by reaction (Van Setten et al., 2001; Konstandopoulos and Papaioannou, 2008). According to Konstandopoulos (2003), clean, unloaded, commercial DPFs have an average porosity of 50 percent and a pore size in the range between 10-30 micrometers (Konstandopoulos, 2003).

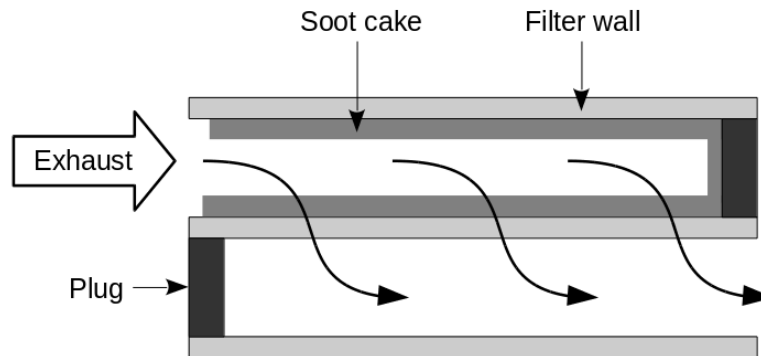


Figure 1.5: Principle of a wall-flow monolith

Regeneration methods

The particles collected in the DPF have to be removed periodically because they lead to an increased pressure drop over the filter and hence to adverse effects on engine performance. In the worst case the filter can become clogged. Regeneration of the filter is commonly achieved by oxidizing the soot in the filter. It is difficult to control the regeneration of soot because the operating conditions of the diesel engine are not constant but depend on the current engine load and this makes prediction of the regeneration progress difficult (Van Setten et al., 2001). For example, the location and number of ignition points in the filter as well as the resulting temperature was found to vary depending on the operating conditions. Key operating conditions are

oxygen concentration, exhaust temperature, soot loading and flow rate (Chen et al., 2009).

The temperature needed to initiate the soot oxidation and maintain the reaction at sufficient rates is greater than 650°C , which is much higher than the exhaust gas temperature. To ensure that oxidation occurs and to prevent soot accumulation in the filter due to insufficient regeneration two common methods exist: energy can be added to the filter system or a catalyst can be used to lower the activation energy of the soot oxidation reaction. The former method is called active regeneration while the latter method is called passive regeneration. A combination of both methods is often used (Konstandopoulos et al., 2000).

Examples of active regeneration include engine measures such as raising the exhaust gas temperature via combustion of post-injected fuel or throttling, as well as external measures such as electric heating (Konstandopoulos and Papaioannou, 2008). Since the reaction is activated by temperature only, the process is also referred to as thermal regeneration (Sarli and Benedetto, 2015).

Passive regeneration can be achieved using fuel-borne catalysts or by coating the filter with a catalyst. It is also possible to use a catalyst to create a more reactive species than oxygen that will react with the soot. This is commonly done by converting nitrogen oxide (NO) from the exhaust into nitrogen dioxide (NO_2). Passive regeneration has the advantage that it requires no additional energy and that the soot is continuously oxidized, even at moderate exhaust gas temperatures ($250\text{-}550^{\circ}\text{C}$) (Konstandopoulos and Papaioannou, 2008).

When control is insufficient and favorable conditions are created in the filter, spontaneous regeneration may occur. This could be as a result of the exhaust gases reaching the required activation temperature to ignite the soot in the filter. A self-sustaining thermal front will propagate through the reactor, leading to very high local temperatures that can damage the filter and shorten its lifetime (Van Setten et al., 2001). This may occur for example in catalyzed filters when the temperature is too low for regeneration over an extended period thus resulting in soot accumulation in the filter. In case the temperature in the filter increases again at other driving conditions, this may ignite the soot leading to the above mentioned thermal fronts (Van Setten et al., 2001). Studies propose that the soot which is in contact with the catalyst ignites first and in this process heat required to sustain the oxidation reaction is generated (Sarli and Benedetto, 2015). The risk of this happening is especially high when a vehicle with a high soot loading in the filter operates at a high engine load first and then drops to idle mode. The high engine load leads to high exhaust temperatures that can ignite the soot while the low flow in idle state does not cool the filter sufficiently. In order to avoid thermal runaways like this, catalytic filters are often combined with an active control system which is triggered when the amount of collected soot in the filter becomes too high. Another advantage of combining both active and passive methods is the lower reaction temperature and hence energy savings (Konstandopoulos and Papaioannou, 2008; Van Setten et al., 2001).

1.1.5 Intrinsic kinetics vs Global kinetics

Soot oxidation kinetics can be described either via intrinsic kinetics or by global kinetics. In the case of intrinsic kinetics, soot oxidation is described on the lowest possible scale; here the reaction pathways of the reaction between the reactants and products are described in detail. This involves a comprehensive description of the reaction steps and identification of the rate limiting step. In order to develop a soot oxidation model on an intrinsic scale one would therefore require input for rate constants of all the elementary reactions. In addition, intrinsic kinetics describe reactions occurring on the surface of the material: i.e. the adsorption of oxygen on the active carbon sites is considered for the case of non-catalyzed soot oxidation. On this level of kinetics, factors such as the size, orientation, impurity concentration, type and location of the crystallite play a major role in the reactivity of the carbon material since they determine the number of active carbon sites present for the reaction. These are therefore put into consideration during formulation of the reaction mechanism for the carbon-oxygen reaction. Therefore description of soot oxidation on an intrinsic level presents its own challenge due to the complexity of the soot particle itself. An alternative to this is the use of global kinetics to describe soot oxidation. Here the many elementary reactions in the reaction pathway are approximated to a single reaction mechanism where by the rate expression used is only dependent on global variables, i.e. gas phase concentration and gas phase temperature, thus evading the complexity that comes with intrinsic kinetics (Neeft et al., 1997; Sampara, 2008; Van Setten et al., 2001).

1.2 Aim

The aim of this work is to investigate the combustion of soot in the DPF of a heavy duty diesel engine exhaust after-treatment system by studying the propagation of thermal fronts in a lab-scale system. The focus will be on an open substrate configuration rather than a DPF configuration. Experiments will be coupled with simulations in order to develop a 2D CFD model that can predict the temperature profile in an open flow soot oxidation reactor. An open-flow, experimental reactor set-up for soot oxidation will be developed and soot oxidation experiments using synthetic soot will be conducted. The commercial CFD software ANSYS Fluent will then be used to develop the 2D CFD model using input from experimental runs. The reactor set-up and the CFD model will be used to identify and analyze the experimental conditions that provoke the occurrence of thermal fronts in the reactor.

1.3 Limitations

This work is limited to fundamental studies on soot oxidation in a lab-scale reactor, using substrates cut from commercial monolithic substrates. The focus on an open flow configuration offers the advantage of a more well-defined flow in contrast to the DPF configuration, which makes studies on the complex interaction of several

transport phenomena as well as chemical kinetics easier and more accurate. It is also easier to use an open configuration for in-situ studies due to a lower resulting pressure drop, hence the open flow configuration is regarded as an acceptable compromise between relevance and significance. Synthetic soot (Printex-U) instead of actual diesel soot particles will be used and a gas mixture will be used instead of diesel exhaust gas. For the sake computational efficiency, a 2D CFD model is chosen over a 3D CFD model; this can affect the accuracy with which the thermocouple placement in the experiment can be reproduced in the model.

2

Theory

In this chapter, the theory behind the methods used in this study will be presented. The concept of space velocity will be described, as well as governing equations for the flow simulation. Since the flow in DPFs under typical conditions is laminar and laminar flow conditions are achieved in the experimental set-up, only theory on laminar flow will be presented. Furthermore, theory about pressure drop and the porous media model used will be given, as well as theory on how the permeability of the substrates used is estimated. The soot oxidation kinetics that will be used in the simulations will be presented and finally, theory on mass transfer effects will be presented.

2.1 Experiments

2.1.1 Space Velocity

Space velocity (SV) is defined as the measure of the time the exhaust gases take in the reactor. It can be used to determine reactor performance in reducing emissions. Space Velocity may be used to determine the conversion efficiency of the reactor since it determines the residence time the pollutants take in the reactor. In the case for short residence time, the reaction of the pollutants is insufficient and thus resulting into decreased conversion efficiency of the reactor. Space velocity (SV) has the units of the reciprocal of the residence time of the pollutants in the reactor and is calculated via the expression given in Equation 2.1.

$$SpaceVelocity = \frac{Q}{V_r} \quad (2.1)$$

where Q is the volumetric gas flow rate at standard conditions in m^3/h . V_r is the reactor volume in m^3 calculated on the basis of the outside dimensions i.e. diameter and length of the reactor. Equation 2.1 gives the space velocity for the reactor in dimensions of $1/h$ (Heck et al., 2009; Mollenhauer and Tschöke, 2010; DieselNet, 2000).

2.2 Simulation

2.2.1 Governing equations

Fluid flow in the domain is modelled by solving a set of governing equations. These are equations of fluid motion derived on the basis of fundamental physics laws; conservation of mass, conservation of momentum and conservation of energy. The number of equations solved depends on both heat transfer and species transport to the flow. In addition, governing equations are solved dependant on whether the flow is compressible or incompressible. For laminar flow regimes, continuity and momentum equations are solved. In addition, the energy equation is solved for flow cases that involve heat transfer. A species conversation equation is solved in case species in the fluid mix or react. These equations are described below in detail (Pletcher et al., 2012; ANSYS, 2013).

Continuity equation

This is a fluid flow equation derived by applying the conservation of mass law on fluid flow. In this case it is assumed that the fluid is flowing in an infinitesimal fixed control volume. The differential form of the continuity equation is therefore written as in Equation 2.2.

$$\frac{\partial \rho}{\partial t} + \nabla \cdot (\rho \vec{v}) = S_m \quad (2.2)$$

Where ρ is the density of the fluid, t represents time while \vec{v} is the velocity vector for the fluid flow. The first term on the left represents the change in density per time in the control volume, the second term represents the flux of mass across the surface surrounding the control volume and S_m is a source term that represents addition of mass to the control volume. In cases where no mass is added to the fluid, S_m is set to zero. Equation 2.2 is valid for compressible flows while some modification is required for incompressible flows where the first term is set to zero. Furthermore, for incompressible single-phase flows, ρ is also taken out from the divergence term. (Pletcher et al., 2012; ANSYS, 2013).

Momentum equation

The momentum equation used in describing fluid flow is derived from Newton's second law of motion and is written as in Equation 2.3.

$$\frac{\partial}{\partial t}(\rho \vec{v}) + \nabla \cdot (\rho \vec{v} \vec{v}) = -\nabla p + \nabla \cdot (\bar{\bar{\tau}}) + S_{mom} \quad (2.3)$$

Here, p is the pressure, $\bar{\bar{\tau}}$ represents the stress tensor. The first term on the left represents the accumulation of momentum in the control volume while the second term on the left represents the convective transfer of momentum across the surface of the control volume. The first term and second term on the right describe surface forces acting on the fluid element, here the first term gives the distribution of the pressure from a surrounding fluid acting on the surface of the fluid element while the

second term on the right represents the gradient of the stress tensor which gives the external stresses exerted on the fluid element. S_{mom} is the momentum source term that gives the contribution of both internal and external forces on the acceleration of the fluid element (Pletcher et al., 2012; ANSYS, 2013). The source term can for example account for pressure drop across a porous medium as it is the case in this work. Further details will be given in Section 2.2.2.

Energy equation

An energy equation is solved in case heat is transferred in the domain. Heat can be transferred in the domain through conduction, convection or radiation. In this study, only heat transfer due to conduction and convection will be considered. Heat transferred is modeled through a general energy transport equation given by Equation 2.4.

$$\frac{\partial E}{\partial t} + \nabla(E\vec{v}) = S_h + \nabla(\bar{\bar{\tau}}\vec{v}) - \nabla q \quad (2.4)$$

Where E is the total energy per unit volume, S_h is the energy source term and q is the heat transferred in the domain. The first term on the left gives the rate of increase of the total energy per unit volume while the second term gives the total loss of energy from the control volume through convection. The rate of heat produced in the control volume due to internal sources is given by the first term on the right. The second term on the right represents work done on the control volume by the surface forces while the third term on the right gives the loss of heat through conduction across the control volume surface which is modeled through Fourier's law of heat transfer by conduction as shown in Equation 2.6.

$$q = -k\nabla T \quad (2.5)$$

Here, k is the coefficient of thermal conductivity and T represents temperature. From Equation 2.4, energy equation is thus given by Equation 2.6 (Johnson, 2016; Pletcher et al., 2012; ANSYS, 2013).

$$\frac{\partial}{\partial t}(\rho E) + \nabla \cdot (\vec{v}(\rho E + \bar{\bar{\tau}})) = \nabla \cdot (k\nabla T) + S_h \quad (2.6)$$

Equation 2.6 is modified for flow in porous media. For modelling heat transfer in the porous zone, one option is to assume thermal equilibrium between the porous medium and the fluid flowing through it. Then an effective thermal conductivity for the porous media (k_{eff}) is used in the first term on the right instead of k. k_{eff} is given by Equation 2.7.

$$k_{eff} = \epsilon k_{fluid} + (1 - \epsilon)k_{solid} \quad (2.7)$$

Here, k_{fluid} is the fluid phase thermal conductivity, k_{solid} is the solid phase thermal conductivity and ϵ is the porosity. Furthermore, the transient term in equation 2.6 is also modified when modelling flow in porous media. Here the transient term is modified to include the thermal inertia of the solid on the fluid. In this study

both flow in porous media and species transport are considered, therefore an energy equation taking into account both porous media and species transport is given here (See Equation 2.8).

$$\frac{\delta}{\delta t}(\epsilon\rho_f E_f + (1 - \epsilon)\rho_s E_s) + \nabla \cdot (\vec{v}(\rho_f E_f + \bar{\tau})) = S_h + \nabla \cdot [k_{eff}\nabla T - (\sum_i h_i \vec{J}_i)] \quad (2.8)$$

Here, ρ_f and ρ_s give the density of the fluid and solid respectively, h_i gives the enthalpy of the i th species and \vec{J}_i is the diffusion mass flux vector of species i due to concentration and temperature gradients in the domain. E_f and E_s represents the total energy per unit volume for the fluid phase and solid phase respectively while $\sum_i h_i \vec{J}_i$ gives the transport of enthalpy due to species transport.

Species conservation equation

Chemical reactions can occur in the bulk, on the wall surface or in porous zones. In case chemical reactions occur in the domain, the mixing and transport of species in the domain has to be modeled. This is done by solving a species conservation equation that accounts for convection, diffusion and reaction source of the species. A species conservation equation used to model mixing and transport of species is as given in Equation 2.9

$$\frac{\partial}{\partial t}(\rho Y_i) + \nabla \cdot (\rho \vec{v} Y_i) = -\nabla \cdot (\vec{J}_i) + R_i + S_i \quad (2.9)$$

Here, R_i represents the net rate of production of species i due to the chemical reaction while S_i represents the addition of species from external sources. Y_i represents the local mass fraction of species i in the domain. Equation 2.9 is solved for $N-1$ species and the species conservation for the N th species is then solved through a species balance. \vec{J}_i represents the diffusion mass flux vector of i due to concentration and temperature gradients in the domain (ANSYS, 2013). \vec{J}_i can be calculated using Fick's law and is given by Equation 2.10.

$$\vec{J}_i = -\rho D_{i,m} \nabla Y_i - D_{T,i} \frac{\nabla T}{T} \quad (2.10)$$

$D_{T,i}$ and $D_{i,m}$ are the thermal diffusion coefficient and mass diffusion coefficient for species i in the mixture respectively. This equation is strictly valid as long as the mixture composition is not changing or the mass fractions of all species except the carrier gas is much smaller than 1. In this thesis, it is assumed that the composition of the gas stays approximately constant and the carrier gas concentration is much higher. Hence, $D_{i,m}$ will be calculated with Equation 2.10. To determine the mass diffusion coefficients for each species, unity Lewis number is assumed (Equation 2.11), which results in Equation 2.12 for $D_{i,m}$.

$$Le_i = \frac{k}{\rho C_p D_{i,m}} = 1 \quad (2.11)$$

$$D_{i,m} = \frac{k}{\rho C_p} \quad (2.12)$$

Le_i is the Lewis number for mixture species i , k stands for thermal conductivity of the mixture, ρ is the density of the mixture, c_p is the specific heat capacity of the mixture and $D_{i,m}$ is the mass diffusivity of species i in the mixture. The Lewis number relates thermal diffusivity to mass diffusivity and it is appropriate to assume it as unity if the molar weights of the mixture component are not very different (ANSYS, 2013). In this case it is considered as appropriate. For simplification purposes, the thermal diffusion (second part on the right hand side of Equation 2.10) or Soret effect is ignored in this work.

2.2.2 Pressure drop and the porous media model

Pressure drop over a monolith

According to Konstandopoulos et al. (2000), the pressure drop of a monolithic DPF loaded with soot may be divided in four parts, as shown in Equation 2.13.

$$\Delta P = \Delta P_{filterwall} + \Delta P_{soot} + \Delta P_{inletchannel} + \Delta P_{outletchannel} \quad (2.13)$$

The first term on the right is the pressure drop across the filter wall, this can be described by Darcy's law for pressure loss due to viscous forces over a porous region. Darcy's law is modified by the Forchheimer term in case of high porosity or high flow rates. The Forchheimer term can usually be neglected for typical extruded ceramic filters. Equation 2.14 shows both Darcy's law and Forchheimer term, where μ is the gas viscosity, α the Darcy permeability, \vec{v} the velocity in the channel and w the thickness of the filter. β is the Forchheimer coefficient (Konstandopoulos and Papaioannou, 2008).

$$\Delta P_{filterwall} = \frac{\mu}{\alpha} \vec{v}w + \beta \rho \vec{v}^2 w \quad (2.14)$$

The second term in Equation 2.13 is the pressure drop across the soot cake, which can be described by Darcy's law as well. The last two terms in Equation 2.13 account for pressure drop in the inlet and outlet channels of a DPF. They are dependent on the flow field and the cross-sectional area of the inlet and outlet channel. They account for the pressure drop due to friction at the channel walls, the effect of the soot cake layer and inertial effects that occur when the flow enters or leaves the channels (Konstandopoulos et al., 2000; Konstandopoulos and Papaioannou, 2008).

The porous media model

The soot cake and the filter wall will be represented in the CFD model by porous zones. Porous zones are treated as fluid zones. The pressure drop is represented by a source term which acts as a sink in the fluid momentum equation and consists of two parts: the viscous contribution and the inertial contribution, where the inertial part is similar to the Forchheimer term mentioned above. For a simple homogeneous porous medium, the source term can be represented as in Equation 2.15 (ANSYS, 2013).

$$S_{mom,i} = -\left(\frac{\mu}{\alpha}v_i + C_2\frac{1}{2}\rho|v|v_i\right) \quad (2.15)$$

In this equation, $S_{mom,i}$ is the momentum source term for the i th dimension. In the first part of the right hand side, μ stands for the fluid viscosity and \vec{v}_i is the velocity in the i th dimension. This is the viscous contribution to the source term. The second part is the inertial contribution, C_2 being the inertial resistance factor, ρ the fluid density and $|v|$ the velocity magnitude. As mentioned for the Forchheimer term, the second part is only important at high flow velocities. In this case, the pressure drop is usually proportional to velocity and hence the inertial resistance factor is assumed to be zero. The remaining source term is Darcy's law and the pressure drop is computed by ANSYS Fluent as in Equation 2.16. (ANSYS, 2013)

$$\nabla p_x = \sum_{j=1}^3 \frac{\mu}{\alpha_j} v_j \Delta n_x \quad (2.16)$$

∇p_x is the pressure drop in the x direction, v_j are the velocities in the x,y and z direction and n_x is the actual thickness of the porous zone in the model in x-direction. Only the equation for the x-direction of the porous zone is shown, but depending on the dimensions of the domain the equation is calculated also in y and z direction. Since the volume blockage that is physically present is not represented in the model, by default FLUENT uses and reports a superficial velocity inside the porous medium to ensure continuity of the velocity vectors across the porous medium interface. It can be chosen if the physical velocity shall be used instead. When using the superficial velocity formulation, it is calculated via the volume flow rate and porosity is not accounted for in the convection and diffusion terms of the transport equations. The superficial velocity formulation does determine the overall pressure drop over the porous zone well, but it is not accurate in predicting the increase in velocity through a porous zone. Superficial velocity will be used in this work.

2.2.3 Determination of the viscous resistance coefficients

Konstandopoulos (2003) report that the permeability of DPFs as well as the permeability of soot cakes is dependent on the porosity of the medium and can be calculated via Equation 2.17. ϵ stands for porosity, $f_w(\epsilon)$ is a factor called the hydrodynamic interaction function, d_p stands for a characteristic dimension of the porous medium and SCF is the Stokes-Cunningham factor.

$$\alpha = f_w(\epsilon)(d_p)^2 SCF(d_p) \quad (2.17)$$

In analogy to Sarli and Benedetto (2015), it is chosen to use the Kuwabara function for the hydrodynamic interaction function, out of three possibilities given by Konstandopoulos (2003). The reason for this can be found in an earlier publication of Konstandopoulos and Johnson (1989): They evaluate different models for particle capture in filtration theory and conclude that a packed bed model like Kuwabara would be the most appropriate to represent flow through a porous monolith wall. This conclusion is based on the manufacturing process of typical ceramic filters,

which are made via extrusion of ceramic powders: it is assumed that the initial packing of the ceramic powder is maintained. (Konstandopoulos and Johnson, 1989) The Kuwabara model was developed for particle collection, but in this work it will be used to model the decrease in viscous resistance under filter regeneration in both the filter and the soot cake.

The Kuwabara function is derived from the solution for the flow field around a packed bed of spheres found by Kuwabara (1959). This solution is valid for creeping flow and is based on defining a spherical boundary around each sphere (unit collector) in order to take the effect of neighboring collectors into account. Kuwabara (1959) assumes that the velocity at the sphere surface is zero and that the vorticity at the spherical boundary is zero. He also reports that an accurate volume fraction (VF) for the packed bed would be as shown in Equation 2.18.

$$VF = \frac{R_c^3}{R_2^3} \quad (2.18)$$

Here, R_c is the radius of the collector and R_2 is the radius of the spherical boundary. Lee and Gieseke (1979) conclude from Kuwabara's publication that the Kuwabara's hydrodynamic factor can also be written as in Equation 2.19.

$$K = 1 - \frac{9}{5}VF^{\frac{1}{3}} + VF - \frac{1}{5}VF^2 \quad (2.19)$$

From these findings, Tardos et al. (1976) conclude a correction factor ($g_w(\epsilon)^3$) for mass transfer to a single sphere in a packed bed using the Kuwabara flow model to account for the effect of neighboring spheres on the flow field around a sphere (Equation 2.20).

$$g_w(\epsilon)^3 = \frac{\epsilon}{(2 - \frac{9}{5}(1 - \epsilon)^{1/3} - \epsilon - \frac{1}{5}(1 - \epsilon)^2)} \quad (2.20)$$

Concluding from the previous results, Konstandopoulos and Johnson (1989) derive their hydrodynamic interaction function $f_w(\epsilon)$ (Equation 2.21).

$$f_w(\epsilon) = \frac{2(2 - \frac{9}{5}(1 - \epsilon)^{1/3} - \epsilon - \frac{1}{5}(1 - \epsilon)^2)}{9(1 - \epsilon)} \quad (2.21)$$

This function is used in Equation 2.17 in order to calculate the change in permeability in dependence of the porosity. The characteristic dimension that appears in the equation is the grain size or the pore size of the filter. The Stokes Cunningham factor accounts for free molecular effects and slip-flow, dependent on the Knudsen number that relates the mean free path of a molecule to the pore size of a medium. However, Konstandopoulos and Papaioannou (2008) report that these effects are usually not observed in uncoated DPFs and then the SCF is equal to 1. For soot cakes however, the SCF is regarded as important and it can be calculated via the Knudsen number as in Equation 2.22. Here the Knudsen number (Kn) relates the mean free path of the gas molecules to the particle diameter of the soot particles (Konstandopoulos et al., 2002).

$$SCF = 1 + Kn(1.257 + 0.4e^{-1.1/Kn}) \quad (2.22)$$

2.3 Soot oxidation kinetics

In this section soot oxidation kinetics used in the project will be presented. Here the reader will be introduced to modelling the kinetics of soot oxidation in general and thereafter details of catalyzed and non catalyzed soot oxidation kinetics will be presented

2.3.1 Soot oxidation reaction kinetics

In describing the soot oxidation reaction kinetics, a kinetic model proposed by Van Setten et al. (2001) can be used to describe the oxidation rate of carbonaceous materials as given in Equation 2.23.

$$r = N_{AS}k_r f(x_{O_2}) \quad (2.23)$$

Where r is the rate of reaction, N_{AS} is the total number of active carbon sites and k_r is the temperature dependent reaction rate constant. $f(x_{O_2})$ is a function giving the dependency of the rate of soot oxidation reaction to the reactant partial pressure. The temperature dependent reaction rate constant k_r is given by the Arrhenius equation (Equation 2.24).

$$k_r = Ae^{-E_a/RT} \quad (2.24)$$

Here, A is the pre-exponential factor, R is the gas rate constant, T is the absolute temperature and E_a is the activation energy.

The total number of active carbon sites is given by Equation 2.25.

$$N_{AS} = s \frac{S_a}{S_{a,0}} \quad (2.25)$$

s is the surface concentration of the active sites present on the carbon particle, S_a is the total surface area (TSA) and $S_{a,0}$ is the initial surface area. However, the linear proportionality in Equation 2.25 is an over-simplification; therefore a better way to model the number of active sites would be through active site area (ASA) instead of using the total surface area. The linear proportionality in Equation 2.25 would hold in this case. Generally however, Equation 2.25 is used to derive kinetic models since ASA is difficult to measure or predict. In describing the intrinsic kinetics of soot oxidation, different models have been suggested in order to describe the $S_{a,0}$. Models like the shrinking core model have been suggested; this model assumes $S_{a,0}$ to be proportional to the outer surface area of the spherical carbon particle. An expression for the total surface area is derived using the shrinking core model as a function of conversion and the soot reaction order ($b=2/3$) as shown in Equation 2.26. Where r_p represents the radius of the spherical carbon particle.

$$\frac{S_a}{S_{a,0}} = \frac{4\Pi r_p^2}{4/3\Pi r_p^3} = 3r_p^{2/3} = (1 - Conversion)^b \quad (2.26)$$

However, for highly porous soot particles Equation 2.26 falls short since it does not predict the reaction accurately due to the changing $S_{a,0}$ as the reaction commences.

This shows yet again the complexity that comes with describing soot oxidation kinetics on an intrinsic level since apart from the non-unified models that are used to describe $S_{a,0}$, soot presents yet another challenge since it changes as the reaction commences. From Equations 2.24, 2.25 and 2.26 the reaction rate equation (2.23) is then described as in Equation 2.27 (Neeft et al., 1997; Van Setten et al., 2001).

$$r = Ae^{-E_a/RT} x_{O_2}^a (1 - Conversion)^b \quad (2.27)$$

From 2.27, Darcy et al. (2007) derived an Equation for diesel soot oxidation as given in Equation 2.28.

$$r = Ae^{-E_a/RT} x_{O_2}^a Z_0 \left(\frac{Z}{Z_0}\right)^b \quad (2.28)$$

Here Z_0 and Z are initial and instantaneous mass concentration of soot in kg/m^3 respectively while $\frac{Z}{Z_0}$ gives the concentration of carbon in terms of conversion.

2.3.2 Non-catalyzed soot oxidation kinetics

In the cases where the soot oxidation process occurs in the absence of a catalyst, carbon reacts with oxygen to form both carbon monoxide and carbon dioxide in molar ratio that changes with temperature. From Equation 2.28, Darcy et al. (2007) describes the oxidation rate for the non-catalyzed soot oxidation as shown in Equation 2.29.

$$r_{noncatalyzed} = Ae^{-E_a/RT} x_{O_2}^a Z_{total,0} \left(\frac{Z_{total,t}}{Z_{total,0}}\right)^b \quad (2.29)$$

Here, $Z_{total,0}$ denotes the initial total mass concentration of soot whereas $Z_{total,t}$ is the instantaneous mass concentration of soot at time t . a and b are parameters for the reaction orders of Oxygen and Carbon respectively. All parameters for the non-catalyzed soot oxidation reaction rate are given in Table 2.1. Here parameters are given for both diesel soot oxidation (Darcy et al., 2007) and Printex-U oxidation Neeft et al. (1997).

Table 2.1: Parameters for non catalyzed Diesel soot oxidation (Darcy et al., 2007) and non catalyzed Printex-U oxidation (Neeft et al., 1997)

	A [s^{-1}]	Ea [kJ/mol]	a	b
Diesel soot	8.5×10^7	164	0.9	0.5
Printex-U	1.26×10^7	168	0.9	0.73

The model described in Equation 2.29 is valid for non-catalyzed soot oxidation processes occurring at oxidation temperature lower than 650 °C in the case for Diesel soot oxidation parameters while for the case of Printex-U oxidation parameters, the model is valid at oxidation temperature lower than 520.85 °C. In the case for Diesel soot oxidation, the model describes the reaction rate of the low reactive part of diesel soot. However, at temperatures lower than 550 °C the reaction rate of the highly reactive Volatile Organic Fraction of soot has to be put into consideration (Darcy

et al., 2007). In this study, the model described in Equation 2.29 is applied on non isothermal soot oxidation reaction occurring at 650 °C. The reaction results in temperatures higher than 650 °C, hence applying the described kinetics may affect the accuracy of the model. Furthermore, only the reaction rate of the low reactive diesel soot is considered, the reaction rate of the Volatile Organic Fraction is not considered since a soot oxidation temperature of 650 °C that is well above 550 °C is used. Here its assumed that all Volatile Organic Components decompose at this high temperature.

2.3.3 Catalyzed soot oxidation kinetics

Soot oxidation can also occur with the aid of a catalyst. Here the catalyst improves selectivity for O₂ and CO is oxidized by the catalyst to CO₂. In deriving a kinetic model for catalytically aided soot oxidation, contact between soot particles and the catalyst plays a major role. Here according to Darcy et al. (2007), presence of a catalyst results into two distinct soot oxidation processes; fast and slow oxidation which occur at different soot conversion rates. From this the total reaction rate for catalytic soot oxidation is deduced (Equation 2.30).

$$r_{total} = r_{slow}(Z_{total}) + r_{fast}(Z_{catalyzed}) \quad (2.30)$$

Here, r_{total} is the total reaction rate for the catalyzed soot oxidation, r_{slow} is the reaction rate for the slow soot oxidation, r_{fast} is the reaction rate for the fast soot oxidation while $Z_{catalyzed}$ is the mass concentration of soot in contact with the catalysed. At high conversion levels, when contact between soot and catalyst is non-existent, a slow oxidation process involving all the carbon sites occurs. The reaction occurs between soot and molecular oxygen independent of the catalyst. Slow oxidation reaction rate is described as in Equation 2.31.

$$r_{slow} = Ae^{-E_a/RT} x_{O_2}^a Z_{total,0} \left(\frac{Z_{total,t}}{Z_{total,0}} \right)^b \quad (2.31)$$

The parameters used in Equation 2.31 are given by Darcy et al. (2007) as shown in Table 2.2.

Table 2.2: Parameters for slow soot oxidation described by Darcy et al. (2007)

A [s^{-1}]	E _a [kJ/mol]	a	b
6.05×10^7	161	0.7	0.8

On the other hand, at low conversion levels contact between soot and catalyst exists. In this case, soot oxidation occurs in the form of fast oxidation and only involves carbon sites that are in contact with the catalyst. Fast oxidation reaction kinetics are described as in Equation 2.32.

$$r_{fast} = Ae^{-E_a/RT} x_{O_2}^a Z_{catalyzed,0} \left(\frac{Z_{catalyzed,t}}{Z_{catalyzed,0}} \right)^b \quad (2.32)$$

Where $Z_{catalyzed,0}$ and $Z_{catalyzed,t}$ are the initial and instantaneous mass concentration of soot in contact with the catalyst respectively. Darcy et al. (2007) describes the parameters used in Equation 2.32 are given by Table 2.3.

Table 2.3: *Parameters for fast soot oxidation as described by Darcy et al. (2007)*

A [s^{-1}]	Ea [kJ/mol]	a	b
1.19×10^{10}	119	0.3	0.8

2.4 Mass transfer effects

2.4.1 Mass transfer effects in monolithic reactors

Flow in open monolith reactors used in engine after-treatment has been reported to be mainly laminar and therefore species are transferred from the gas phase to the porous region through molecular diffusion (external mass transfer). In the porous region the species are then transported through the pores to the reaction sites by porous diffusion. The reactor could be operated either in the mass transfer limited region or in the kinetic limited region, depending on the reaction rate. In the case of high reaction rates, the rate at which the species react will be faster than the rate at which they are transported to the reaction site. In this case the reactions in the reactor are said to be limited by mass transfer. The reverse is true for low reaction rates (Hayes and Kolaczkowski, 1994; Tronconi and Forzatti, 1992). In determining the kinetics used in the reactor, mass transfer effects have to be considered since these determine how fast the reacting species are transported to the reaction sites. The rate of mass transfer in the reactor is thus determined via the dimensionless Sherwood number (Sh) given in Equation 2.33.

$$Sh = \frac{k_c d_h}{D_{AB}} \quad (2.33)$$

Where k_c is the mass transfer coefficient, D_{AB} is the diffusion coefficient and d_h is the hydraulic diameter. Sherwood numbers can be determined either experimentally or via simulations. When the steady state Sherwood number is determined experimentally this would require steady state conditions in the reactor and the value determined would therefore depend on the experimental conditions used. The Sherwood number can also be determined globally or locally. In determining a local Sherwood number experimentally, one would have to measure local mass concentrations in the reactor which is difficult to do due to the sizes of the monolith channels.

2.4.2 Determination of Sherwood number from simulations

Due to the level of difficulty and uncertainty that surround experimental determination of Sherwood number, simulations are used instead (Hayes and Kolaczkowski, 1994). Therefore, the steady state Sh number can be determined using a model where by the mass transfer coefficient is computed from the concentration gradient simulated by the model. With the concentration field of O_2 available from a model, Sherwood number can be calculated via D_{AB} and k_c . D_{AB} can be determined empirically via the Fuller equation for binary diffusion as given in Equation 2.34. This is an equation derived from the kinetic theory that gives the diffusion coefficient of a binary gas mixture.

$$D_{AB} = \frac{1.00 \times 10^{-8} T^{1.75} \left(\frac{1}{MW_A} + \frac{1}{MW_B} \right)^{1/2}}{p \left[(\sum \nu_A)^{1/3} + (\sum \nu_B)^{1/3} \right]^2} \quad (2.34)$$

Here AB is a binary gas mixture with solute A dissolved solvent B. Solvent B makes the bulk since A is assumed to be at infinite dilution. In Equation 2.34, ν_A and ν_B

represent empirical atomic diffusion volumes of A and B respectively, M_A and M_B represent their molecular weight, p gives the pressure while T gives the absolute temperature (Fuller et al., 1966).

In determining the mass transfer coefficient k_c , flux N can be determined from the concentration field simulated by the model via a shell balance made across the channel. Here the molar flow rate of the reacting species is computed at the inlet and outlet of the reactor in question and these are used to compute the flux N in mol/m^2s as given in Equation 2.35. Where $F_{A,in}$ and $F_{A,out}$ are molar flow rates of A at the inlet and outlet respectively and A_{shell} is the area of the cake layer.

$$N = \frac{F_{A,in} - F_{A,out}}{A_{shell}} \quad (2.35)$$

Thereafter, k_c is calculated in m/s via Equation 2.36

$$N = k_c(C_{b,A} - C_{s,A}) \quad (2.36)$$

Where C_b and C_s are the bulk concentration and average surface concentration of the reacting species A. These are also determined from the concentration field simulated by the model. Sherwood number is then determined via Equation 2.33 (Ekstrom, 2005).

3

Methods

In this section, the experimental set-up used in the study will be described, as well as the methods used to carry out various experiments. Furthermore, a general description of the obtained 2D CFD model will be given. Finally, the conditions and settings used in the preliminary simulations after Sarli and Benedetto (2015) as well as for the simulations matching the experiments of this thesis will be provided.

3.1 Experiments

An experiment set-up used for conducting both soot oxidation and flow experiments is developed. This also involves development of a pattern for thermocouple placement used in the set-up. Flow experiments are then conducted in order to characterize the reactor and finally soot oxidation experiments are conducted. The methods used in both the development of the experiment set-up and in the different experiment runs are described in detail below.

3.1.1 Reactor and other equipment

Soot oxidation in the reactor occurs in ceramic monolithic substrate samples that are made up of small parallel channels. The ceramic substrate samples used in the experiment are cut from a cordierite cylindrical wall flow monolith of 200 /12 cells per square inch. The channels of the substrates have 0.012 inch wall thickness and a repeating distance of 0.071 inch (Figure 3.1).

At the reactor inlet, the cut substrate samples are modified in order to prevent gas flow through the substrate channels in this region. This is achieved by blocking the channels using glue. At the reactor outlet no modification is done to the channels; they are left open to allow access for thermocouples. The ceramic substrate used in the experiment has the dimensions 153 mm x 12 mm x 6 mm and is contained in a 12 mm x 12 mm x 153 mm steel casing with 1mm wall thickness (Figure 3.2).

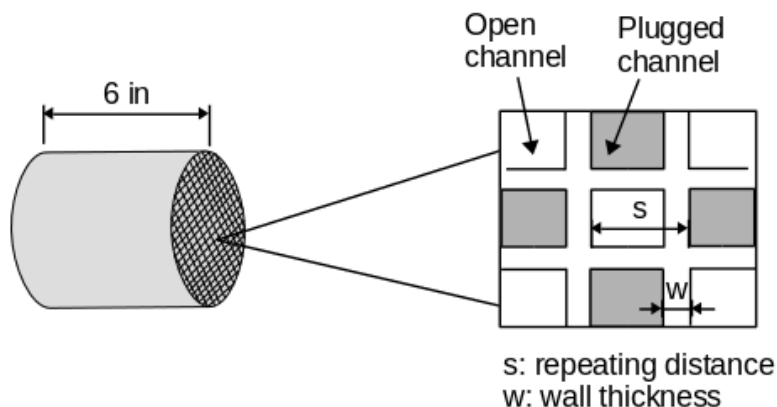


Figure 3.1: 200 /12 cpsi cordierite monolith and zoomed-in view of channels in the monolith.

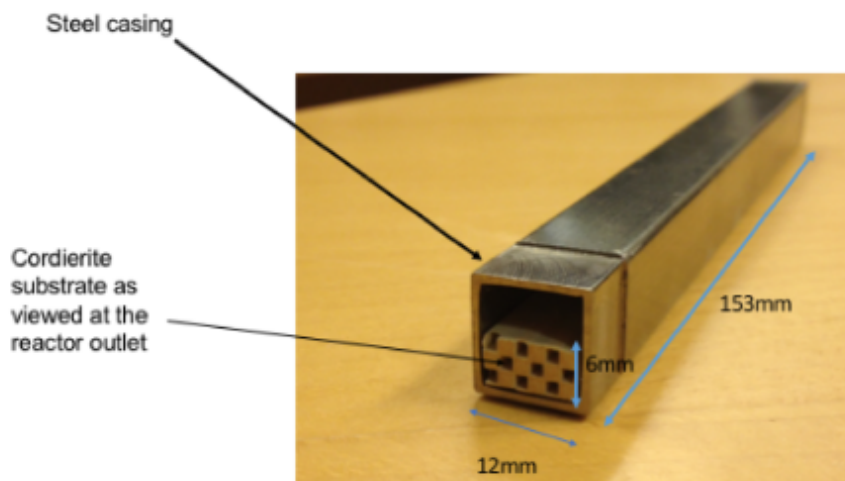


Figure 3.2: Reactor view from the outlet. The steel casing is 12 mm x 12 mm x 153 mm and the dimensions of the cut monolith substrate inside are 153 mm(= 6 in) x 12 mm x 6 mm.

Oven

A ceramic cylindrical hollow oven as shown in Figure 3.3 is used to heat up the reactor set-up. A heating coil in the wall of the oven heats up the oven to the desired temperature set on the oven temperature controller. Isothermal temperatures in the oven are thereafter achieved via the oven temperature controller. The oven temperature is measured by a thermocouple running along the inner wall of the oven, this predicted temperature signal is then sent to the temperature controller which then regulates the temperature of the oven to the desired value either by switching the heating coil on or off.

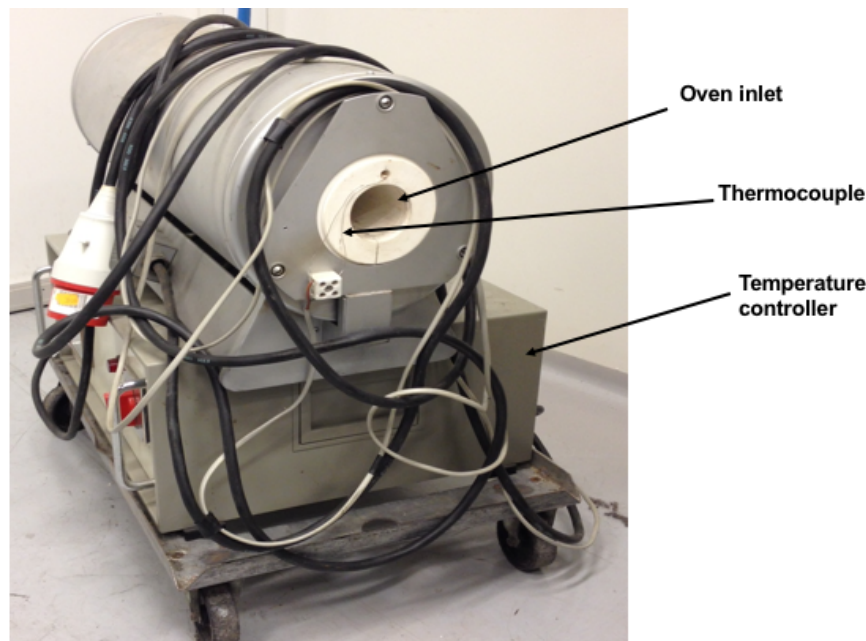


Figure 3.3: Front view of the oven

Thermocouples

In order to predict the temperature in the substrate and on the reactor surface 'type K' thermocouples are used. 0.5 mm probe diameter 'type k' thermocouples are used to measure the temperature in the substrate. On the other hand, 1mm probe diameter type K thermocouples are used to measure the temperature on the reactor surface and at the air inlet. The latter are used on the reactor surface in order to increase durability of the thermocouples since these have to be removed and re-attached for every experiment run. The thermocouples are calibrated as described in Appendix A. They are calibrated at both 0 °C and 100 °C reference temperature. Appendix A gives the temperature correction factors obtained from this calibration. It is assumed that the deviation from 100 °C is the same at the reactor temperature used later.

Other equipment

In order to measure and control the gas flow into the reactor set up, Bronkhorst High-Tech B.V.'s EL-FLOW type mass flow controllers of capacity 20 L_n/min and 2000 mL_n/min connected in series are used. Further information about the operating principle and properties can be found in Appendix A. A Horiba infrared gas analyzer is used to measure and quantify the amount of CO_2 and CO released at the reactor outlet. There is also an analyzer that detects nitrogen oxides (NO_x), whose pump is used to draw the gas sample for the Horiba analyzer. It is not used for analysis in this work, but it can be used in case of conducting soot oxidation via NO_x . Further information about properties and calibration of the Horiba analyzer is attached in Appendix A as well.

3.1.2 General Experiment set-up

In conducting either flow or soot oxidation experiments, a general experimental set-up is used. A detailed description can be found in Appendix B.1. The resulting set-up is shown in Figure 3.4, with the thermocouples placed as presented in Figures 3.5 and 3.6: A pair of thermocouples is placed both at the inlet and at the outlet. The thermocouples of each pair are placed at the same axial points, but different radial points in order to measure the radial temperature differences. Another thermocouple is placed in the middle of the substrate. In this way, axial temperature differences in the substrate are measured.

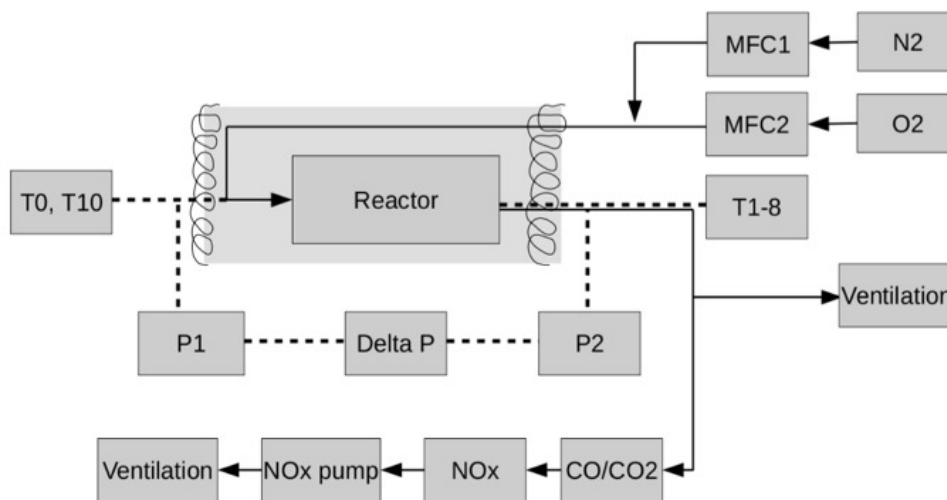


Figure 3.4: Flow diagram showing the insulated experimental set-up.

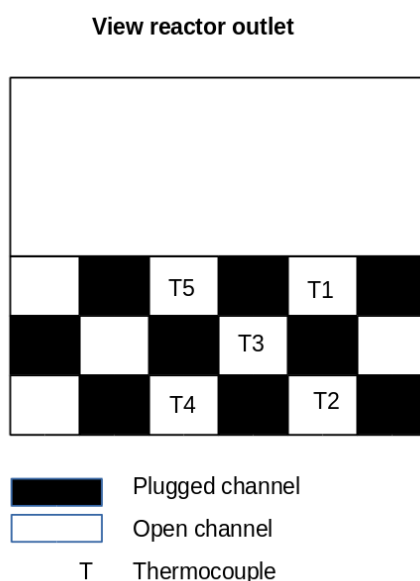


Figure 3.5: Thermocouple placement in the substrate outlet

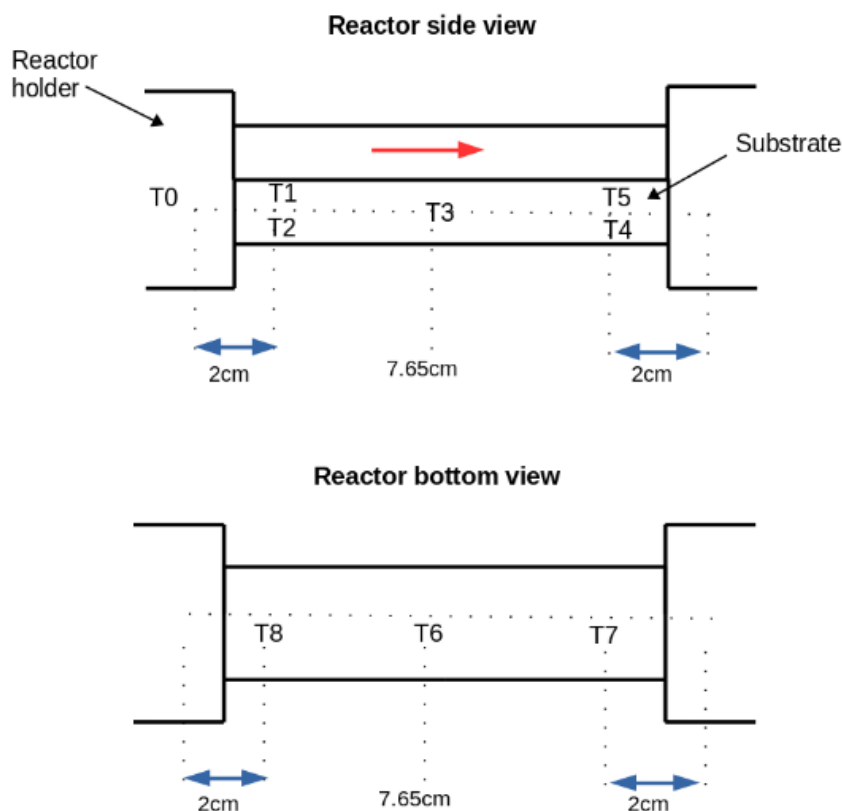


Figure 3.6: Thermocouple placement view from side and bottom of the reactor. The red arrow indicates the flow direction.

3.1.3 Leak proof test

To ensure that the set up is air tight, leak proof test is done on the different parts of the reactor set up. Leaks in the set up arise due to either poorly connected junctions or due to cracks and air bubbles in the ceramic glue applied on the reactor. To conduct leak proof test, the reactor set up part in question is connected to a pressurized synthetic air feed flowing in at $1 L_n/min$ and 1 bar pressure. All outlets from this the reactor set up are blocked and a gas leak detector spray is then used to locate possible leaks in the set up. Bubbles on the pipes connections or the glued part of the reactor indicate leaks.

3.1.4 Flow experiments

Flow experiments are carried out in order to characterize the reactor in terms of the temperature profile developed in the substrate and on the reactor walls. To achieve this, the reactor set-up is heated for some time until a steady temperature profile is achieved. In this type of experiment, no soot is loaded in the reactor, rather the reactor is heated up while air flows through it. To begin with, the reactor and experiment set-up are assembled as described in section 3.1.2. The reactor air inlet connected to the mass flow controllers is fed with $2000 mL_n/min$ (corresponding to a SV of 10893.2) pressurized air with the gas feed coming in at 4 bar. The

reactor is heated up in stages ranging between 600 and 800 °C to obtain a steady temperature. The temperature at different points in the substrate and on the reactor is measured by the attached thermocouples and logged in Lab-view. In addition, the pressure drop across the reactor is also logged in Lab-view as the reactor is heated up. Several flow experiments are carried out and the result of one of them is presented in Appendix C. Axial temperature differences are observed: the difference is roughly 10 °C between the measurements at inlet and outlet. The middle thermocouple measures temperatures very close to the inlet temperatures; However, in other flow experiment runs it has been in between the inlet and the outlet temperatures.

3.1.5 Soot oxidation experiments

Table 3.1: Experiment conditions used for different soot oxidation experiment runs conducted

Experiment condition	Soot oxidation Experiment 1	Soot oxidation experiment 2	Soot oxidation experiment 3
Mass of soot [mg]	70	32.6	73.9
Soot oxidation temperature [$^{\circ}C$]	650	650	650
Pressure [bar]	4	4	4
Gas mixture flow rate [L_n/min]	2	2	2
O ₂ [vol%]	15	2.5	15
N ₂ [vol%]	85	97.5	85
Synthetic air flow rate [L_n/min]	1.5	0.25	1.5
N ₂ flow rate [L_n/min]	500	1.75	500

Soot oxidation experiments are performed at two different conditions. Table 3.1 gives the experimental conditions used in different soot oxidation experiments conducted. In order to obtain a starting guess for extreme conditions that would provoke a thermal front, soot loading, oxygen concentration and temperature similar to those used by Chen et al. (2009) are used (Chen: 10 g/L soot loading, 15% O₂, 635 °C). Chen et al. (2009)’s study is used for starting guess due to the similarity of their study to this thesis i.e. they conduct experiments in a reactor that contains a section of a DPF substrate and apply soot on the top surface of the substrate as it is done in this thesis. However, a lower space velocity (based on the whole reactor volume and volumetric flow at room temperature) and wall-flow configuration is used in their experiments. The amount of soot used in the experiment runs similar to Chen et al. (2009) (soot oxidation experiment 1 and 3) is calculated as described in Appendix D.1. The composition of the flow rate of both synthetic air and N₂ required to make up the gas mixture used in the soot oxidation experiment is also calculated as described in Appendix E.1. In another experiment run the conditions are modified (experiment 2): the soot mass is half of experiment 1 and the oxygen concentration is a sixth of the concentration in experiment 1. This is done in order to investigate a lower border of conditions and it was planned to conduct more experiments in between however due to time restrictions this was not possible. For the sake of

reproducibility the experiment run similar to Chen et al. (2009) is conducted twice (soot oxidation experiments 1 and 3). In conducting soot oxidation experiments, soot is first applied on the surface of the reactor substrate as shown in the Figure 3.7.

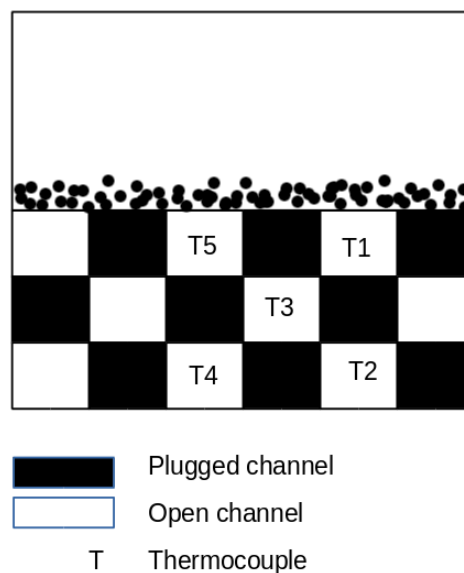
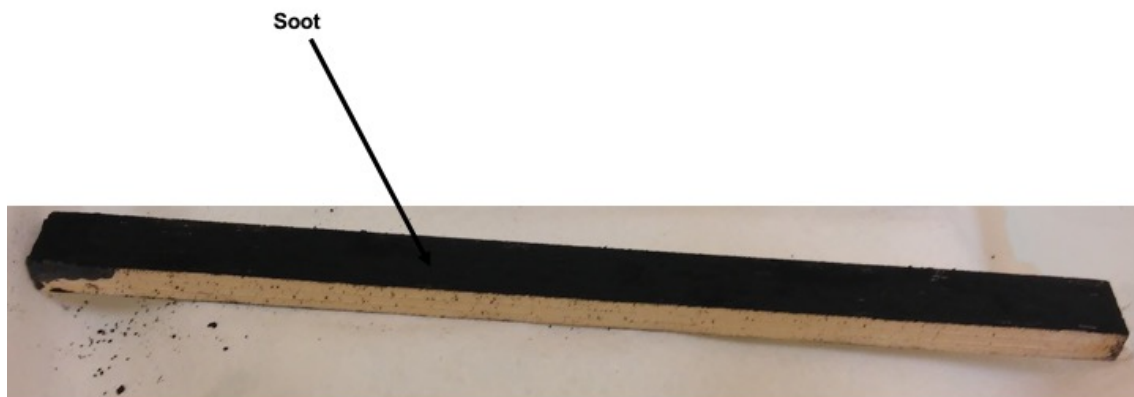


Figure 3.7: Soot applied on the top surface of the substrate. No soot is put into the channels.

The experiment is then set up as described in the Section 3.1.2. This is then followed by calibration of the gas analyzers as described in Appendix A. With all the connections made, the reactor is first heated up to the soot oxidation temperature.

This is achieved by heating up the reactor using 2 L_n/min N_2 with the synthetic air turned off. The reactor set up is heated up in stages as described in the section 3.1.4. When the reactor has been heated up to the desired soot oxidation temperature and a steady temperature profile in the substrate has been attained, synthetic air is then turned on and the flow rate of N_2 is adjusted accordingly. This sets off oxidation of soot in the reactor. The temperatures measured by the thermocouples, the pressure drop measured across the reactor as the oxidation commences and the amount of CO and CO_2 produced are logged in Lab-view.

3.1.6 DPF experiment

One trial is made using a DPF substrate made from SiC loaded with a real diesel engine; This is done in order to see if it is possible to conduct soot oxidation experiments in a DPF with the current experimental set-up. The thermocouples are put at the same axial positions as in the open substrate, but at different radial positions. The resulting graphs are shown in Appendix F. Due to time restrictions, there is no further analysis made in this thesis.

3.2 Simulation

A CFD model is built that can simulate the temperature development during regeneration of a DPF. The set-up is made in analogy with a model presented by Sarli and Benedetto (2015) and first simulations are done using the conditions of Sarli and Benedetto (2015) in order to verify the implementation of the model. Afterwards, the model is used on the open-flow geometry and conditions of the experiments described in this thesis. In the following, the general set-up is described, followed by two separate sub-sections containing the simulation conditions for both the preliminary simulations and the simulations matching the experiments in this thesis.

3.2.1 Modelling of the gas mixture

The inlet gas mixture is assumed to contain only nitrogen (N_2) and oxygen (O_2). It is also assumed that the soot oxidation reaction produces only carbon dioxide (CO_2). The density of the gas mixture is calculated according to the ideal gas law and its specific heat capacity is calculated as the mass-fraction average of the component's heat capacities (mixing-law). The specific heat capacities for the individual gas components are specified as temperature-dependent, using a piecewise-polynomial approach. The viscosity of the gas mixture as well as its thermal conductivity are calculated by assuming a temperature dependency given by correlations for N_2 reported in Canu (2001). The thermal conductivity is implemented as piecewise-polynomial whereas viscosity is implemented as a function of temperature. The expressions can be found in Appendix G. The mass diffusivity is determined assuming unity Lewis number as described in the theory Section 2.2.1.

3.2.2 Modelling of the influence of soot consumption on porosity and viscous resistance

In reality, soot is present in the filter as well as as the soot cake layer on top of the filter. When modelling of the experiments of this thesis only the soot in the cake layer is considered. This is assumed since in the experiments soot is applied manually as opposed to being deposited on the substrate using a real engine exhaust gas. Furthermore, a non-catalyzed substrate is used. Sarli and Benedetto (2015) on the other hand use a catalyzed filter and they assume a certain concentration of soot in the filter. Hence, expressions for porosity and viscous resistance for the filter are needed in addition to the expressions for the soot cake in order to reproduce their results. Since this method is first written in a general manner, the expressions for soot consumption in both filter and soot cake will be described.

Both the soot cake and the filter are defined as porous zones and the pressure drop across them is calculated via the porous media model. The soot layer is modelled as a layer of a certain thickness and porosity and it is initialized with a certain soot mass concentration before simulation. The consumption of soot over time is represented in the model by decreasing the porosity of the layer. (Sarli and Benedetto, 2015)

The porosity of the soot layer is considered to be linearly dependent on the local soot mass concentration, as shown in Equation 3.1.

$$\epsilon_{cake} = 1 - \frac{Z}{\rho_{soot}} \quad (3.1)$$

Here, ϵ_{cake} represents cake porosity, Z is the mass concentration of soot while ρ_{soot} is the density of the soot. $\epsilon_{cake} = 1$ corresponds to the state where all soot has been oxidized. The model does not describe the behaviour of single soot particles and the breakdown of the soot layer as the soot is oxidized is not accounted for.

The porosity of the filter is also assumed to vary in a linear manner depended on the local mass concentration of soot. A porosity of 0.5 is assumed for the clean filter, which is a common porosity for DPF filters (Konstandopoulos and Johnson, 1989). A value for the loaded filter is found by calculating the volume of soot in a computational cell ($V_{soot,cell}$) via dividing the initial mass concentration by the density of soot.

$$V_{soot,cell} = \frac{Z_0}{\rho_{soot}} \quad (3.2)$$

Then the combined volume fraction (VF) of soot and filter material in one computational cell is calculated. Where, V_{filter} and V_{cell} represents volume of the filter and volume of the cell respectively.

$$VF = \frac{(V_{soot,cell} + V_{filter})}{V_{cell}} \quad (3.3)$$

The resulting porosity of the filter (ϵ_{wall}) is calculated via Equation 3.4.

$$\epsilon_{wall} = 1 - VF \quad (3.4)$$

The resulting porosity for both soot cake and filter before and after soot oxidation is given in Table 3.2. Their calculation for each iteration is dynamically updated using additional in-house functions hooked to the main CFD solver. The obtained initial porosity for the soot cake layer agrees with reported values in literature, although the reported range varies a lot ((Swanson et al., 2013; Kim et al., 2009; Konstandopoulos et al., 2002)).

The viscous resistance of both soot cake and filter is assumed to be dependent on their respective porosity and is calculated using Equation 2.17 and the Kuwabara function (Equation 2.21) that have been introduced in Section 2.2.3. For simplification, the SCF factor is assumed to be 1 and the grain size/pore diameter of the soot particles/filter unit collectors is kept constant. It has to be kept in mind that this is a very simplified model for the soot cake and is not representing reality for the soot cake particles, since they shrink over time and vanish once the soot has been oxidized. In order to estimate the grain size of the soot cake, the value for initial viscous resistance used by Sarli and Benedetto (2015) is taken and it is calculated backwards to the grain size using Equation 2.17. The same is done for the filter, but in this case the value for viscous resistance provided by Sarli and Benedetto (2015) is based on the clean filter (Sarli and Benedetto, 2015). The obtained grain size/pore size can be found in Table 3.2. The viscous resistance used for the filter

is in agreement with data reported by Konstandopoulos and Johnson (1989) for a 200 cpsi cordierite monolith and the obtained pore size of $24.4 \mu\text{m}$ for the filter is in agreement with typical cordierite monolith pore sizes (Gulati, 1986). The obtained values will be used to reproduce the results of Sarli and Benedetto (2015) as well as for the simulation of the experiments in this thesis.

The viscous resistances are finally calculated for each iteration via additional in-house functions hooked to the viscous resistance section for the first direction in the porous zone. The first direction is specified in -y direction. In the second direction, which is the x-direction in 2D, the viscous resistance is specified 3 orders of magnitude larger than in direction 1. This is done to simulate that the main flow direction is downwards through the porous zones. Figure 3.8 and 3.9 show viscous resistance plotted versus porosity for the soot cake (top) and for the filter (bottom).

Table 3.2: Values for viscous resistance, permeability, initial porosity, porosity after oxidation and grain size/pore size for soot cake and filter

Domain	Viscous resistance [m^{-2}]	Permeability [m^2]	Initial porosity	Porosity after oxidation	Grain size [μm]
Soot cake	4×10^{13}	2.5×10^{-14}	0.92	1	0.574
Filter	2×10^{12}	5×10^{-13}	0.494	0.5	24.2

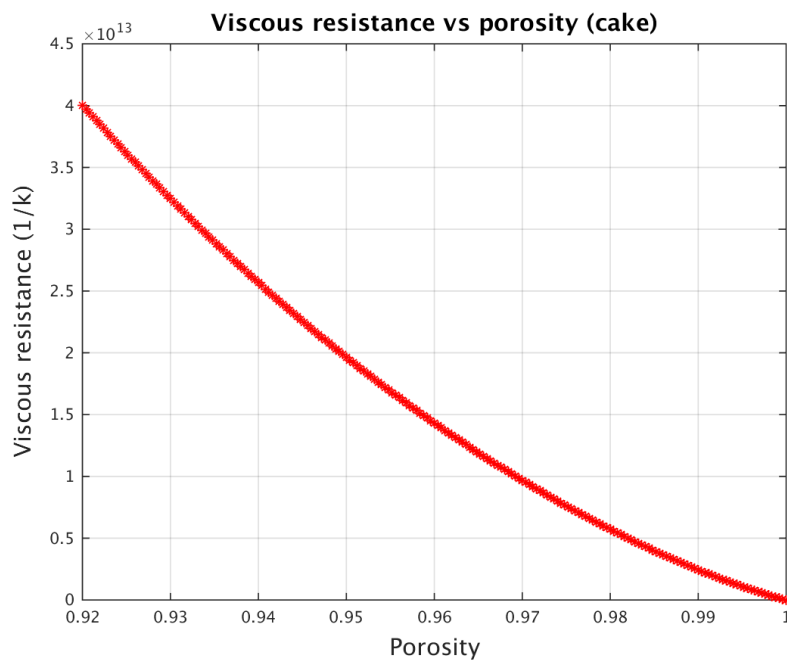


Figure 3.8: Viscous resistance against porosity for the cake

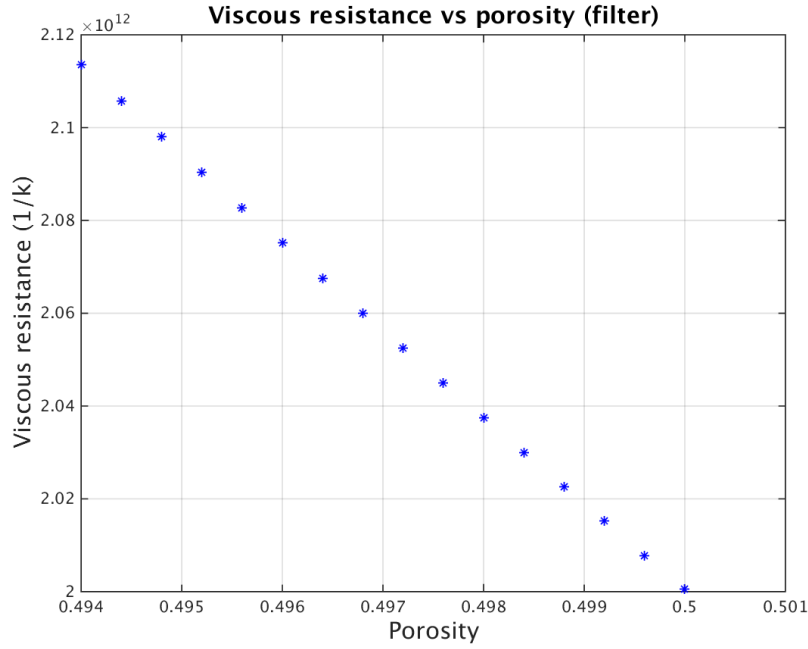
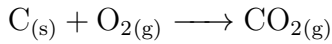


Figure 3.9: Viscous resistance against porosity for the filter

3.2.3 Modelling of the soot oxidation reaction

In accordance with Sarli and Benedetto (2015), full selectivity for CO_2 is assumed for simplification and the reaction equation is shown below.



The reaction rates are implemented as source terms for the species conservation equations. They are calculated via additional in-house functions. The reaction rate for soot in $\frac{\text{mol}}{\text{m}^3\text{s}}$ is determined by calculating the reaction rate for soot consumption according to the kinetic model by Darcy et al. (2007) (see 2.3.1). Since 1 mol soot is assumed to react with 1 mol O_2 to 1 mol CO_2 , the reaction rates for O_2 and CO_2 are then the same as the one calculated for soot, with a positive sign for the product CO_2 and a negative sign for the reactants.

As mentioned above, the soot is represented as a layer in the geometry and it is therefore not present as a species in the model, rather as the solid material that makes up the porous zone of the soot cake. There are different versions of the in-house code for the soot cake and the filter, since the preliminary simulation considers catalyst in the filter whereas a non-catalyzed substrate is used in the experiments in this thesis. The reaction in the soot cake is assumed to follow the slow catalyzed kinetics presented in Section 2.3.3, since only a small fraction of the soot is in contact with the filter surface. The small fraction will be neglected. On the contrary, all the soot that is in the filter is assumed to be in contact with the catalyst and therefore both slow and fast kinetics are applied on all soot present in the filter (see Section 2.3.3) (Sarli and Benedetto, 2015). To ensure mass conservation, a source term is also written for the continuity equation: It is calculated by subtracting the reaction rate for O_2 from the reaction rate for CO_2 .

3.2.4 Treatment of the heat release from the reaction

The heat produced by the exothermic soot reaction is accounted for as source term in the energy equation presented in Section 2.2.1. The heat of reaction (H_R^0) is calculated by subtracting the heat of formation of the product CO₂ ($H_{products}^0$) from the sum of the heat of formation for the two reactants ($H_{Reactants}^0$) (McQuarrie, 2011), as shown in Equation 3.5.

$$\Delta_f H_R^0 = \sum \Delta_f H_{Reactants}^0 - \sum \Delta_f H_{Products}^0 \quad (3.5)$$

The standard heat of formation for soot is assumed to be similar to that of graphite, which is zero. The heat of formation for O₂ is zero as well, whereas it is -393.5 *kJ/mol* for CO₂ (NIST, 2016). To obtain the source term for each iteration, the heat of reaction is multiplied with the molar reaction rate of soot. Using this way of calculating the heat of reaction assumes that the heat of formation is not dependent on temperature. To investigate this matter, a comparison with an reaction enthalpy dependent on temperature will be done, using the temperature dependent heat capacities of the participating species.

3.2.5 Preliminary simulation of Sarli and Benedetto (2015) for verification of the model

A 2D geometry is made, using the dimensions given by Sarli and Benedetto (2015). It represents a section of a DPF, consisting of one inlet channel as well as an outlet channel and separate zones for the soot cake and the filter wall. A schematic view of the geometry is shown in Figure 3.10.

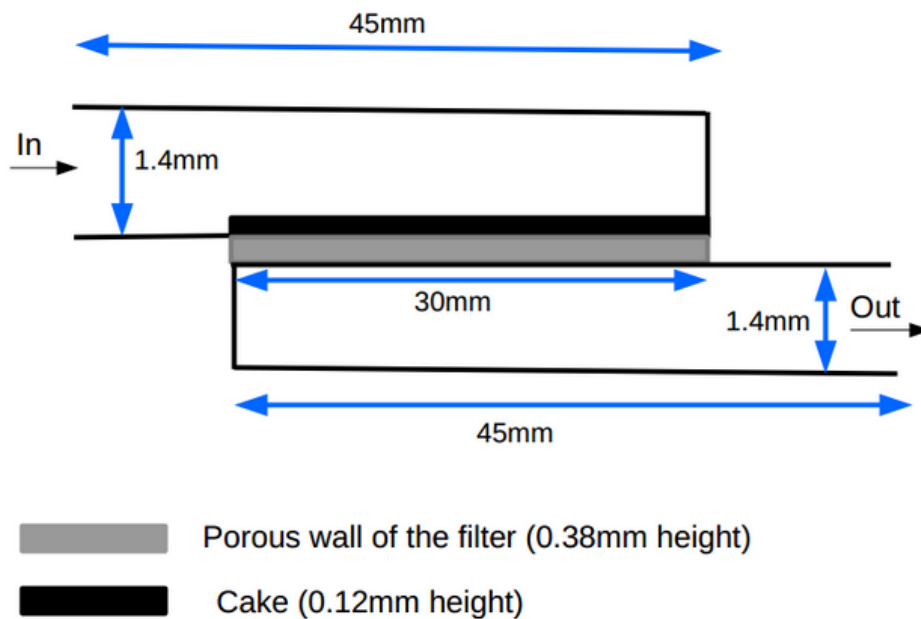


Figure 3.10: Schematic drawing of the geometry for the preliminary simulation after Sarli and Benedetto (2015)

Then a mesh is generated on this geometry with the cell size reported by Sarli and Benedetto (2015). Information about the mesh is provided in Table 3.3.

Table 3.3: Mesh parameters and mesh quality aspects for the preliminary simulation.

Max. cell size	No. of Elements	Orthogonal quality	Maximum Aspect ratio	Maximum orthogonal skewness
0.025 mm	219629	0.8397	2.5284	0.16024

Energy equation and species equation are solved, as well as the equations for the fluid flow. Material properties for the mixture are set as presented in Section 3.2.1 and the material properties for soot and for the filter material silicon carbide (SiC) are set according to Table 3.4 (Sarli and Benedetto, 2015).

Table 3.4: *Solid material properties for the preliminary simulation (Sarli and Benedetto (2015))*

Material	Intrinsic density [kg/m^3]	Specific heat capacity [$J/(kgK)$]	Thermal conductivity [$W/(mK)$]
Soot	2500	900	10
SiC	3240	1120	18

The soot cake and the filter are defined as porous zones and the in-house code for the viscous resistances and porosities is hooked (see Section 3.2.2). The superficial velocity formulation is chosen. Soot is chosen as the solid material for the soot cake and SiC is chosen as filter material. Thermal equilibrium between the porous medium and the fluid flowing through it is furthermore assumed. Source terms are activated for these porous zones and the in-house code for the source terms for reaction rate, heat production by reaction as well as mass conservation is included. The inlet conditions are set as shown in Table 3.5. Adiabatic wall conditions are applied. No species transport is allowed through the outside walls of the channels (Sarli and Benedetto, 2015).

Table 3.5: *Inlet boundary conditions and initial conditions from Sarli and Benedetto (2015). Velocity is given at inlet temperature 813 K while SV is given at standard conditions*

Velocity at inlet conditions [$\frac{m}{s}$]	3 (SV= 132022.1)
O_2 mol fraction [$\frac{mol}{mol}$]	0.15
Temperature [K]	813
Initial soot concentration [$\frac{kg}{m^3}$]	200 (cake), 15 (filter)
Initial velocity [$\frac{m}{s}$]	0
Initial temperature [K]	523

The problem is solved transiently, using a pressure-based segregated solver. The pressure-velocity coupling scheme used is SIMPLE. The convective terms are discretized using a second-order upwind scheme and the diffusive terms are discretized using a second-order bounded central differencing scheme. The second order accurate implicit scheme is chosen for discretization of the transient terms. A time-step of 0.1s is used, which is large, but according to Sarli and Benedetto (2015) this is appropriate since the time-scale of the reaction is much larger than the time needed for the flow to pass the domain. They base this assumption on a claim made by Konstandopoulos et al. (2000) that a quasi-steady approximation can be used for the gas flow because the transient behaviour of the filter is slow compared to the residence time of the gas in the filter. In order to monitor the solution and to be able to compare to the results of Sarli and Benedetto (2015), monitor points are made along the axial length of the filter and the soot cake layer (Figure 3.11). The monitor points are named according to their distance from the inlet and if they are in the soot cake (c) or in the filter (f). Temperature as well as soot mass concentration will be recorded over time.

3. Methods

Several cases reported by Sarli and Benedetto (2015) are reproduced in this work. The cases differ in their values for the pre-exponential factor for the fast catalyzed oxidation kinetics: the pre-exponential factor obtained from the study of Darcy et al. (2007) is multiplied with a factor k_s that ranges from 0 to 10. Only the cases 0, 1 and 5 will be reproduced and reported in this thesis report.

c1	c2	c3	c4	c5	c6	c7
						
f1	f2	f3	f4	f5	f6	f7

Figure 3.11: Monitor points for recording the temperature in the cake and in the filter made in accordance with Sarli and Benedetto (2015). The points are where the crosses are, where f stands for filter and c stands for soot cake.

3.2.6 Development of a 2D open flow model

In the experiments, an open flow reactor is used, as described in Section 3.1.1. It is chosen to use a 2D simulation and to represent the channels as open, as it is assumed that the temperature variation across the depth of the substrate is negligible. In reality, there are thermocouples inserted in the channels as described in the experimental method. An artificial wall on the left end of the substrate is introduced to represent that this side is closed with ceramic glue. A schematic view of the geometry used for the simulation is shown in Figure 3.12. Information about the mesh used can be found in Table 3.6.

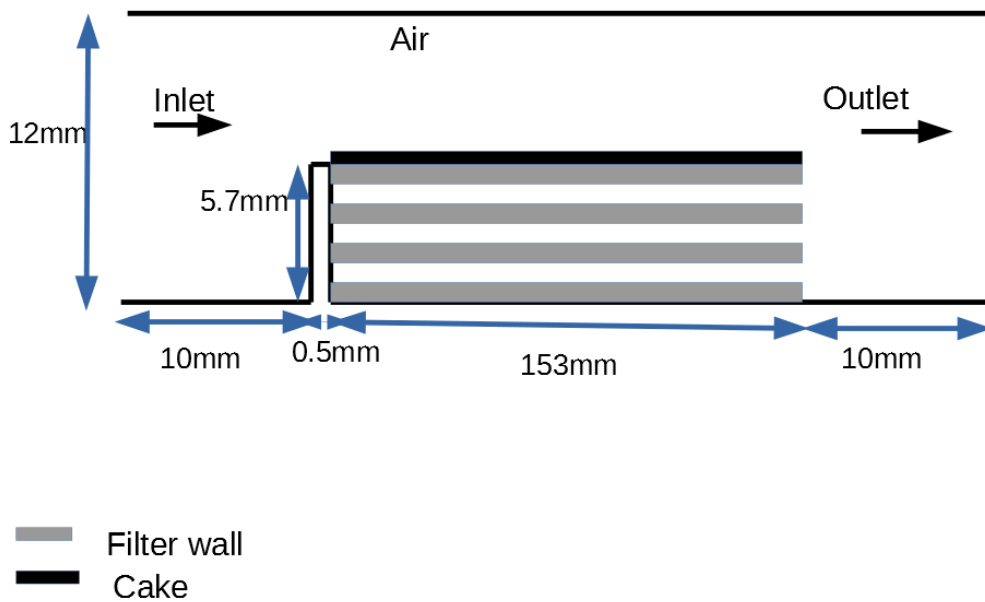


Figure 3.12: Scheme of the model geometry for the experiments

Table 3.6: Mesh parameters and mesh quality aspects for the simulations of the experiment

Max. cell size	No. of Elements	Orthogonal quality	Maximum Aspect ratio	Maximum orthogonal skewness
0.1 mm	240825	0.7079	3.775	0.292

Most of the simulation set-up is the same as described in the previous section about the preliminary simulations. Therefore, only the differences will be pointed out. The solid material of the filter walls is chosen to be cordierite instead of SiC, because the substrate in the experiment is made from cordierite. The material properties can be found in Table 3.7 and are an average of values found in different sources. The wall material is set as steel for the outside walls and as cordierite for the artificial wall.

A temperature profile is applied to the reactor wall since it is observed from the flow experiments that there is an axial temperature variation across the length of

the reactor: The temperature is highest at the outside wall at the reactor inlet and it decreases towards the outlet. Also, the oven can not be controlled other than with an analogous scrolling wheel and it is observed in the flow experiments that not the same temperature is reached every time with the same settings. Therefore, for each experiment simulation a wall temperature profile is developed that fits the experiment in question and the inlet temperature is adjusted as well. The temperature profile is obtained from the thermocouples attached at the bottom of the reactor and it is applied to both the top and bottom outside walls in the model. The profile is approximated as linear and extrapolated over the whole length of the model. This is done since only the soot oxidation part of the experiments and not the heating up phase will be simulated: in the soot oxidation phase the temperatures increase very slowly compared to the speed of the reaction and therefore the profile is regarded as constant over time.

The porosity and viscous resistance of the filter substrate are set as constant values of 0.5 and $2e-12$ for this case, since the soot was applied manually it is assumed that the amount of soot in the substrate is negligible. For the same reason, only the slow kinetics will be applied (see Section 2.3.3).

Monitor points are defined at the same axial and radial positions as the thermocouples in the substrate in the experiment. The height of the cake layer is calculated to be 0.2 mm for a soot loading of 200 kg/m^3 . The initial mass concentration of soot actually used is then adjusted according to the exact amount of soot applied in the corresponding experiment. The inlet species concentrations are set according to the corresponding experiment as well. Monitor points are set that correspond to the positions of the thermocouples in the reactor substrate; They are shown in Figure 3.13.

Table 3.7: *Solid properties cordierite*

Density [kg/m^3]	Specific heat capacity [$\text{J}/(\text{kgK})$]	Thermal conductivity [$\text{W}/(\text{mK})$]
2100	750	1

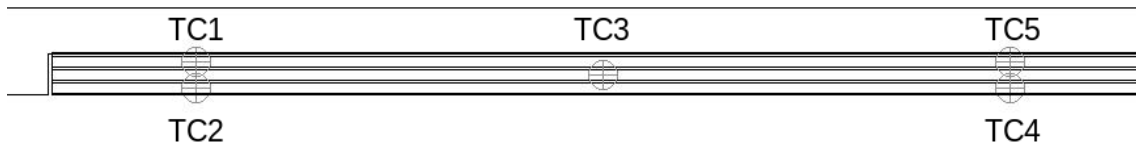


Figure 3.13: *Monitor points for recording the temperature in the substrate. The points are in the middle of the crosses and they correspond to the thermocouple placement in the experiments.*

Simulations are then run for the three experimental runs presented in Table 3.1. To begin with, kinetics for diesel soot oxidation reported by Darcy et al. (2007) are used. Furthermore, simulations are run using kinetics for Printex-U oxidation reported by Neeft et al. (1997) (see Table 2.1 for a summary for the non-catalytic soot oxidation parameters).

3.2.7 Mass transfer effects in the reactor

In order to assess the mass transfer effects in the reactor, a 2D model developed in Section 3.2.6 is used to both assess the possibility of having oxygen depletion in the reactor and to calculate the Sherwood number. A steady state Sherwood number is calculated from a steady state flow field simulated by the 2D model. To begin with, a converged flow and energy steady state solution is simulated. Thereafter the concentration field of O_2 in the model is attained by solving only the O_2 equation. Here a zero concentration of O_2 is imposed in the cake porous region; this is with the assumption that the reaction rate is infinitely high so that all the O_2 in the cake (reaction surface) is instantly consumed. Hence, the reactor is assumed to be operating in a mass transfer regime. Three different velocities are investigated as shown in Table 3.8. The first velocity (0.7408 m s^{-1}) corresponds to the velocity used in the soot oxidation experiment 1, the second velocity (15.3 m s^{-1}) corresponds to residence time corresponding to Sarli and Benedetto (2015) inlet conditions while the third velocity (0.224 m s^{-1}) is chosen in order to invoke oxygen depletion by using a velocity that is much lower than the velocity used in the experiment. The inlet conditions used are summarized in Table 3.8.

Table 3.8: *Inlet and initial conditions used in the steady state simulation*

Velocity [$\frac{m}{s}$]	0.7408	15.3	0.224
O_2 mol fraction [$\frac{mol}{mol}$]	0.15	0.15	0.15
Temperature [K]	936.77	936.77	936.77
Initial velocity [$\frac{m}{s}$]	0.7408	15.3	0.224
Initial temperature [K]	936.77	936.77	936.77

The corresponding Sherwood number for each case is then determined from the simulation result according to the theory given in Section 2.4.2.

4

Results and Discussion

In accordance with the aim of the thesis, the soot oxidation experiments and simulations are designed to provoke a thermal front. In the following, the results of both experiments and simulations are presented and comparisons between the experimental result and the predictions made by the simulations are reported.

4.1 Experimental results

Several observations about the behaviour of the experimental set-up are obtained from the conducted flow experiments.

Firstly, the pressure drop over the reactor generally increases with temperature (see Figure C.1 Appendix C), which is due to increased gas velocity at higher temperatures. It is also dependent on how tight the connections are. Part of the pressure drop behaviour at high temperature can also be attributed to the cracking of the ceramic glue at high temperature, which reduces the pressure drop. Secondly, there is an axial temperature variation over the reactor, which is dependent on the temperature given by the control unit of the oven but also on the position of the reactor in the oven. The temperature at the inlet is highest and the temperature at the outlet is lowest (see Figure C.2 and C.3 in Appendix C). From Figure C.3 it can also be observed that the radial differences in the substrate are small: The differences in temperature measured by the thermocouples on the same axial position is only a few degrees (1-4 °C). This is important in order to be able to observe an increase in temperature during the following soot experiments and also to be able to observe heat transfer from the surface through the substrate. Thirdly, a slight increase in temperature over time is observed, which decreases in magnitude the longer the oven is heated. This is caused by the control sequence of the oven control unit.

4.1.1 Soot experiment 1

The experimental result of soot experiment 1 are evaluated first, representing experiment 1 and 3. Experiment 3 is a reproduction of experiment 1 and exhibits and thus exhibits the same temperature pattern as experiment 1. Experiment 1 will be discussed here and the plots for experiment 3 can be found in Appendix I.

The recorded temperatures in Figure 4.1 show peaks for the thermocouples in the substrate and on the reactor outside once the oxygen is introduced. It is observed that the oxidation lasts for approximately 6 minutes (360 s) under the current conditions. The peaks are highest for the temperatures measured by the thermocouples

closest to the surface of the substrate and lowest for the thermocouples on the reactor outside. This shows that the additional heat is produced by the oxidation reaction in the reactor on the surface of the substrate. The heat is transferred via conduction from the surface of the substrate to the reactor bottom. The temperature increase is highest at the reactor outlet (TC5), with an exotherm of approximately 72 °C. Second highest is the increase in the middle of the reactor (TC3) and lowest at the inlet (TC1). It has to be noted that the starting temperature for the soot oxidation is not the same due to the axial temperature gradient in the reactor. The relative increase is calculated by subtracting the temperature at the start temperature for each temperature measurement from its further values in order to set all temperatures to 0 at the start of the soot oxidation. The resulting plot is shown in Figure 4.2. To investigate when the soot ignites at which axial position and to see how the axial profile develops, the relative increase is plotted over the length of the reactor over time. Some stages are displayed in the Appendix H in Figure H.1. It is found that the temperature increase starts at the same time (0.27 s) at the inlet and outlet and then in the middle. The peak at the outlet is highest, presumably because a large part of the heat produced upstream is transported along the reactor and there is also heat conduction in the substrate. This causes the reaction to speed up downstream. In accordance with this, the peak in the middle is second highest. However, the middle thermocouple reaches a higher temperature than the thermocouple in the inlet after a while. The thermocouple in the middle of the substrate is placed in a lower channel compared to the inlet and outlet thermocouples at the surface. This affects the temperature increase, as the heat must be conducted first to reach the thermocouple and some is also transferred in other directions than downwards. Due to this, it is unknown how high the temperature at the surface is in the middle at the same position as the other two thermocouples closer to the surface. In the simulation result presented later it is observed that the temperature of the soot layer in the middle of the substrate surface is actually higher than that in the outlet and the inlet. A thermal front that moves from the back of the reactor channel to the front and then backwards again, as it was observed by Chen et al. (2009), is not obtained in the soot experiments 1 and 3. Only a single peak of high temperature is observed at the inlet, in the case of occurrence of a moving thermal front a second peak of high temperature would have been measured at inlet temperature thermocouple.

The pressure drop is around 615 Pa before oxygen is added and increases by roughly 25 Pa when the soot oxidation reaction starts. The increase is difficult to be seen in Figure H.3 (Appendix H) because the signal is very noisy and the values read from it are therefore not accurate. It is however visible upon comparison with the data recorded before oxygen is added to the system. The increase is probably due to the temperature increase from the reaction, as it is observed in the flow experiments mentioned earlier that the pressure drop increases with temperature. Afterwards, the pressure drop slightly decreases over time, as can be seen Figure H.3. The decrease can be explained by possible cracking of the ceramic glue due to the temperature increase as well as decreasing temperatures as the soot oxidation reaction slows down. However, the pressure drop does not decrease to the original value before soot oxidation but stays at 630 Pa. This can be explained by the temperatures not being totally constant but slightly increasing in time.

The recorded signals for CO and CO₂ are integrated in order to compare the amount of CO and CO₂ produced with the amount of soot put into the reactor. A molar flow of 0.00136 mol/s (calculated from 2 L/min at 298K, 1 atm) is used. It is expected to achieve almost 100% conversion of soot to gaseous products, since the substrate is clean after the soot oxidation. However, the conversion is calculated to be 72%. This is assumed to be mainly due to the fact that the peak for CO has to be reconstructed from the ratio of CO/(CO+CO₂), since no appropriate gas for the calibration range needed for the instrument was available. Figure 4.3 shows the plot for ppm of CO and CO₂ produced, including the reconstructed peak. However, the ratio of CO₂ to CO produced is reported in literature to depend significantly on the temperature used. Neef et al. (1997) reports ratio of CO₂ to CO of 1 at 780 K, the ratio is then reported to decrease at oxidation temperature greater than 780 K. However the ratio changes during the temperature peak in the soot oxidation experiment can not be accounted for in the results due to lack of data. Furthermore, taking the molar flow rate at room temperature could affect the accuracy.

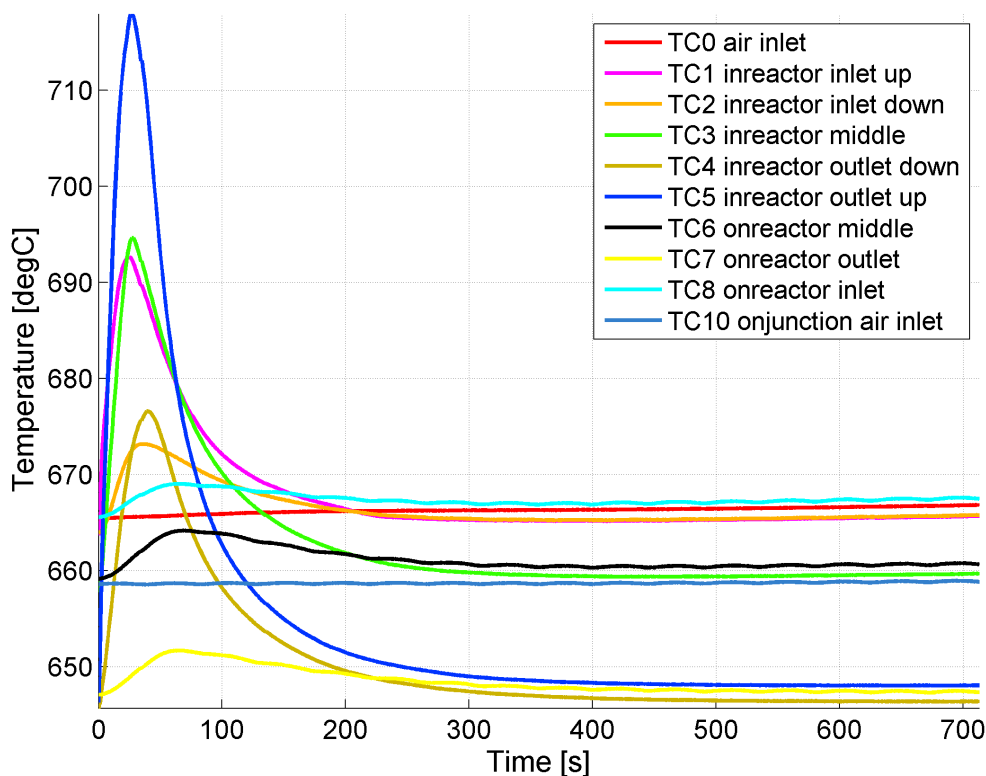


Figure 4.1: Temperature measured during soot oxidation in experiment 1. Note that there are axial differences in temperature also at the start of the soot oxidation. They show the same pattern and are about the same magnitude as after the soot oxidation (around 600 s).

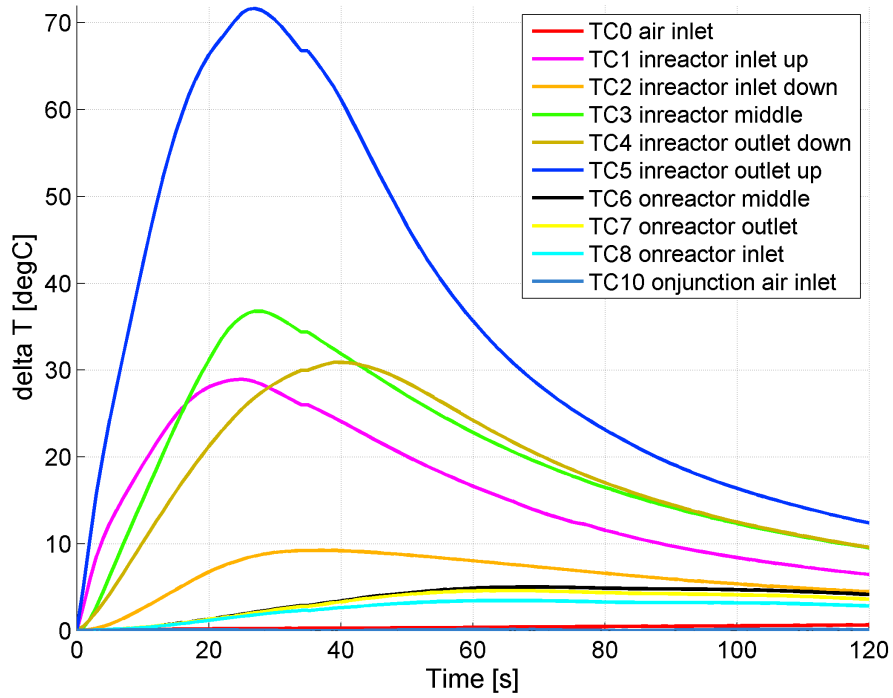


Figure 4.2: Relative temperature increase during soot oxidation in experiment 1

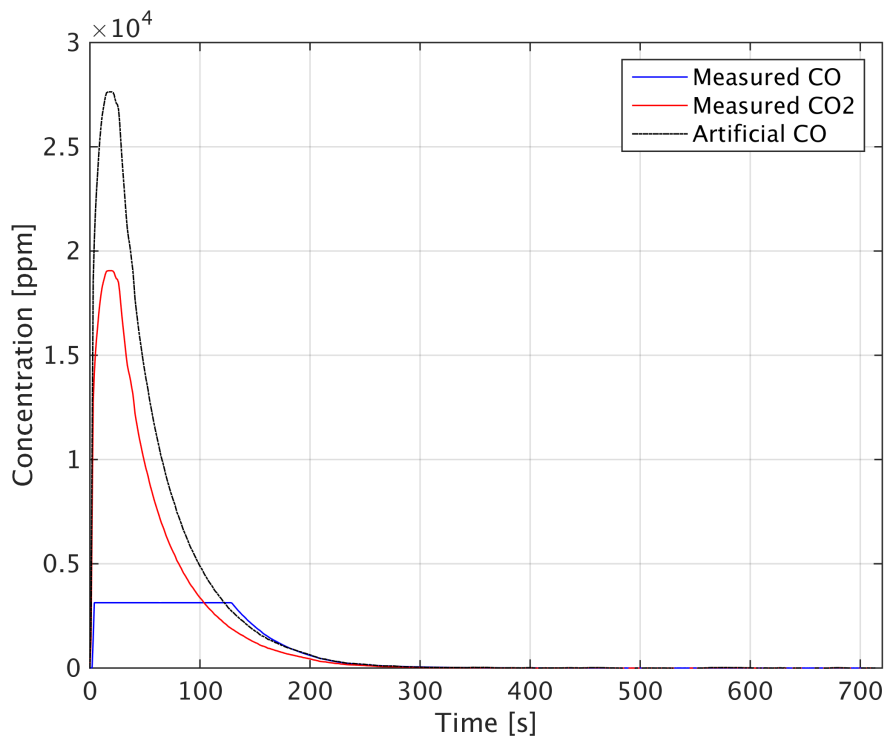


Figure 4.3: Production of CO and CO2 during soot oxidation in experiment 1 (Peak for CO reconstructed)

4.1.2 Soot experiment 2

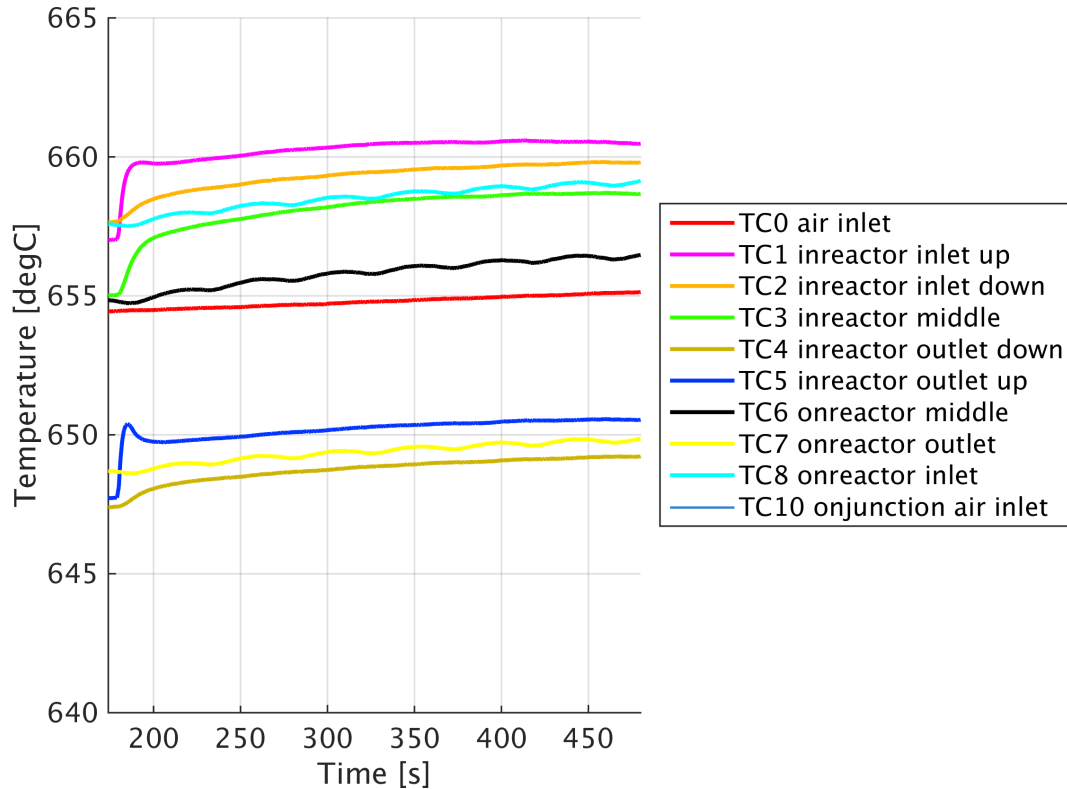


Figure 4.4: Temperature measured during soot oxidation in experiment 2. Only a part of the data is shown to highlight the peaks at the start of the soot oxidation when oxygen is turned on (at approx. 180 s).

The obtained temperature plot is shown in Figure 4.4. Only part of the data is shown to highlight the peaks at the start of the soot oxidation. Only a very small exotherm of 4 °C is observed as can be seen in Figure 4.4. Only a part of the data is shown to highlight the peaks at the start of the soot oxidation when oxygen is turned on (at approx. 180 s). It is concluded that this combination of inlet temperature, oxygen concentration, soot mass and inlet velocity is not favorable to provoke a peak of high temperature. Furthermore it is seen that increasing the flow rate decreases temperature and increasing the oxygen concentration gives a slight increase in temperature as well. The soot is completely burned after the experiment (oxidation time approximately 2400 s); hence, the initial soot loading could be too small to provoke a steep increase with a high exotherm or the oxygen concentration could be too low. Limitation by oxygen availability is thought to be likely since a peak in the temperature at TC5 (outlet) is observed, which then decreases and settles on a constant reaction rate. The peak is assumed to occur due to heat from the reactions occurring upstream and judging from the trend observed in experiment 2 this should lead to the highest peak always being at the outlet. But the highest magnitude is observed at the inlet, so a decrease in oxygen availability towards

the outlet could explain this difference. It can be concluded that the oxidation occurs, but reaction rates are low and it takes a long time to burn all the soot under these conditions. Unfortunately, the recording of CO and CO₂ concentrations is not available, but during the experiment the readings for CO and CO₂ have been observed to determine if the soot has been fully oxidized, indicated by zero ppm.

4.2 Reproduction of the 2D model of Sarli and Benedetto (2015)

First, the flow field will be described and analyzed; it represents the flow field in a DPF. Then the results of the cases $k_s=1$ and $k_s=0$ will be presented (see Section 3.2.5 for explanation of k). $k_s=1$ corresponds to the original kinetics taken from Darcy et al. (2007). Finally, $k_s = 5$ will be reported.

4.2.1 Analysis of the flow field

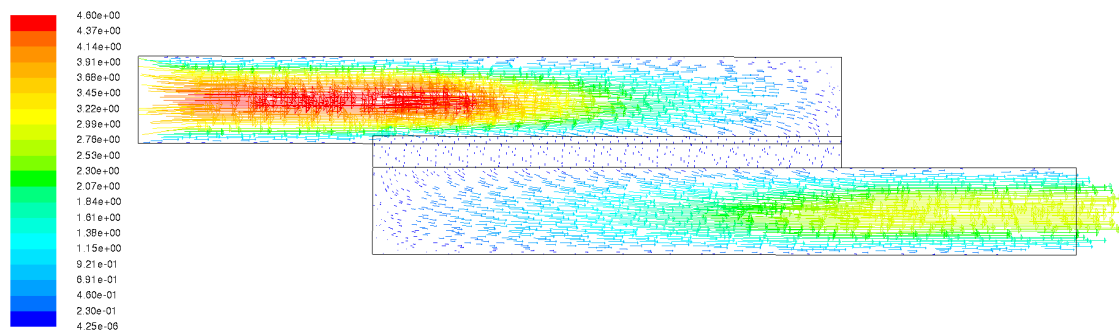


Figure 4.5: *Vectors of velocity coloured by velocity magnitude in m/s for the preliminary simulation (scaled in y direction). Red is high velocity, blue is low velocity.*

Figure 4.5 shows the velocity vectors coloured by velocity magnitude for the first second of simulation where the reaction rates are still very low and no soot has been consumed yet. The velocity is highest in the inlet channel (top left) and then reduces towards the end of the channel since this is blocked at the end. The velocity is lower towards the channel walls because a no-slip condition is applied. Since the soot cake and the filter wall are porous, the flow is then forced downwards through these zones and proceeds towards the outlet. Its velocity increases again towards the outlet (bottom right), but the overall velocity magnitude is lower than that in the inlet. The reason for this is assumed to be reduction of the inlet channel height due to the soot cake layer. Losses due to friction in the channels and the porous wall can also be an explanation. The pressure drop observed is about 14751 Pa, which is in the range for pressure drop of typical DPFs reported by Konstandopoulos and Papaioannou (2008).

4.2.2 $k_s = 1$ and $k_s = 0$

The resulting temperatures over time for case $k_s = 1$ are plotted for the monitor points made along the axial length of the filter (see Figure 3.11) and the plot is shown in Figure 4.6. The simulations are aborted after a while because the simulation time is long and the achieved result is satisfying for testing of the CFD model. It can be seen that the obtained pattern of temperature is in very good agreement with the result reported by Sarli and Benedetto (2015), although the maximum temperature that is reached is approximately 4 K higher in Di Sarli's plot. The monitor plots for mass concentration for the soot cake and the filter are also in excellent agreement with the ones reported by Sarli for $k_s=1$. The reproduced plot for conversion of the mass concentration of soot in comparison with the original is shown in Figure 4.7. It is investigated if the lower temperature observed could be explained by the assumption made that the reaction enthalpy is constant value that is multiplied with the reaction rate. This is done assuming a temperature dependent reaction enthalpy based on temperature dependent heat capacities of the reaction components; however, this does not change the obtained result.

The case $k_s=0$ is investigated because no catalyst is used in the filter in the experiments of this work. The conversion plot is shown in Figure 4.7. Sarli and Benedetto (2015) reports that the conversion of soot is the same for the filter and the soot cake. However, the reproduced result shows that the conversion in the filter is higher than that of the soot in the soot cake. This is regarded to be closer to reality, since the soot cake is very porous and hence consists mostly of air. It is expected that the produced heat is stored longer in the filter, and since the reaction rate is dependent on temperature this will speed up the conversion in the filter.

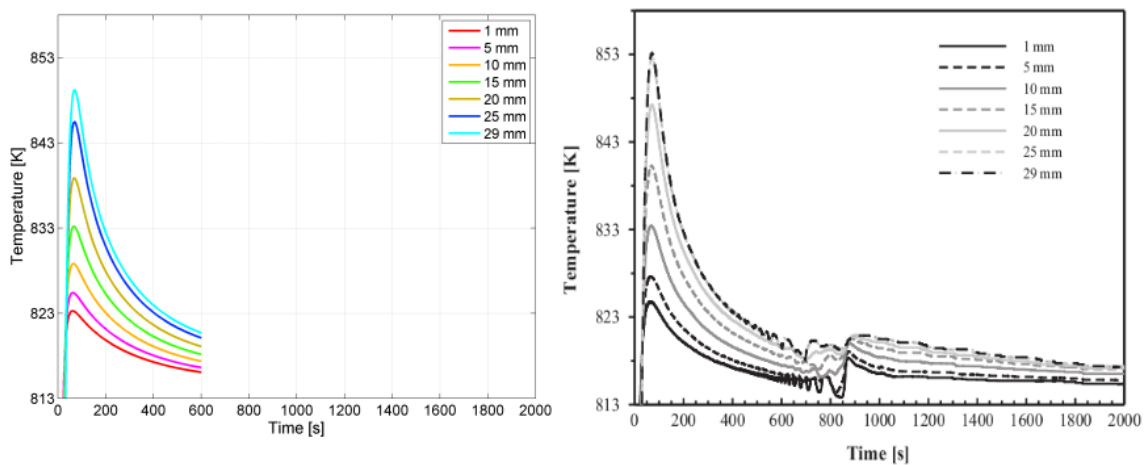


Figure 4.6: Plot of temperature predicted in the wall of the filter vs time for case $k_s = 1$. Reproduced temperature plot (left) and temperature plot reported by Sarli and Benedetto (2015) (right)

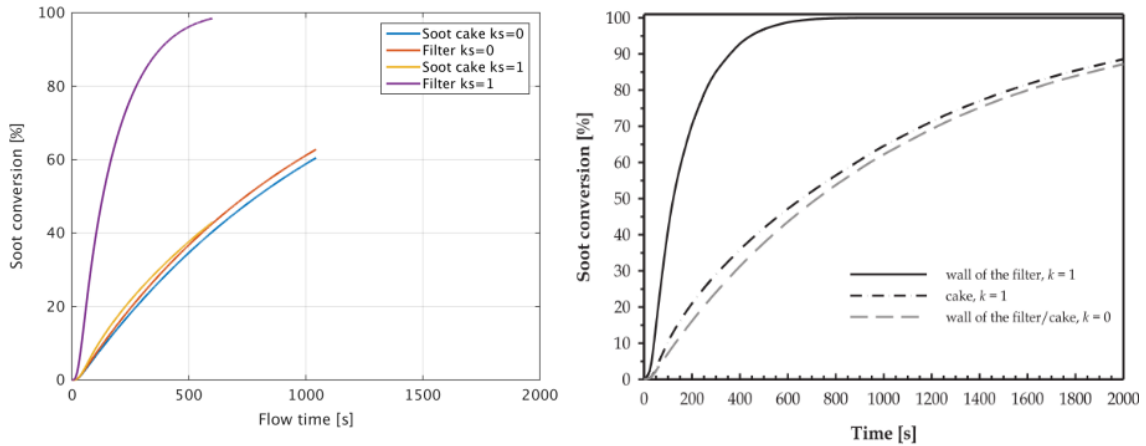


Figure 4.7: Soot conversion vs flow time for $k_s=1$ and $k_s=0$ case. Reproduced soot conversion plots (left) and and soot conversion plots reported by Sarli and Benedetto (2015) (right)

4.2.3 $k_s = 5$

At high values of k_s it is observed in the simulations in this thesis that the temperature increases rapidly after the heat-up phase; at this point the simulation crashes due to divergence. A possible reason for this is identified as negative oxygen concentration or negative soot mass concentrations at high soot consumption rates. In order to avoid this problem, the soot mass concentration is limited to be minimum 0 and a limiter on the reaction rate is set for the case of negative oxygen/negative soot concentration. Since this is not improving stability, it is concluded that the time step used may be too large to resolve the steep temperature increase; When thermal runaway occurs, the reaction rates increase drastically and cause large gradients in the domain and the fluid properties change drastically. It is no longer possible to resolve the transport of reactants into and out of the cell and eventually the flow field diverges. Hence the time step chosen must provide a good balance between transport and reaction rates to avoid too large gradients. However, the simulation time increases significantly when a very small time step is used and to be able to observe a thermal front a certain amount of flow time is needed. To circumvent this problem, the temperature is limited to 1300 K and explicit formulation is used in the calculations of the source terms. The explicit formulation is a more conservative approach for the case of a thermal runaway. Furthermore, the flow field is converged first and then updated every 10 time steps, since the flow is only resolved at a large time-scale due to the long time step; therefore it is assumed that the flow field changes slowly with respect to the temperature and concentration fields and updating the flow less often could enhance convergence. The resulting plot for temperature registered at the monitor points in the filter is shown in Figure 4.8. Upon comparison with plots for $k_s = 2.3$ and $k_s = 10$ reported by Sarli and Benedetto (2015) it can be concluded that the achieved temperature pattern in Figure 4.8 is in between those two extreme cases. The front of high temperature starts at f7, which is towards the outlet of the reactor, and then moves towards the inlet. This is also shown in the contour plots in Figure 4.9.

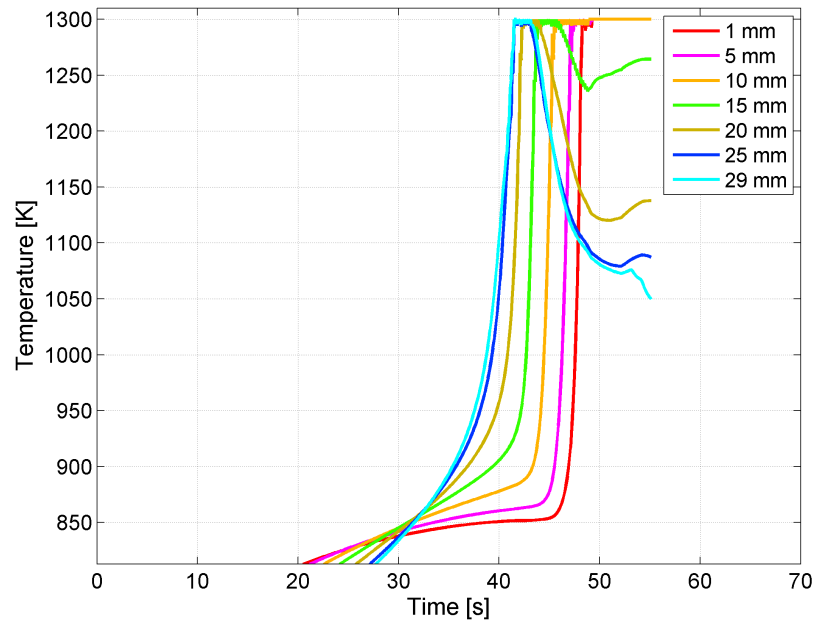


Figure 4.8: Temperature registered at the monitor points in the filter for $k_s = 5$ case, using an explicit formulation of the source term, with temperature limited to 1300 K and updating the flow field every ten time steps.

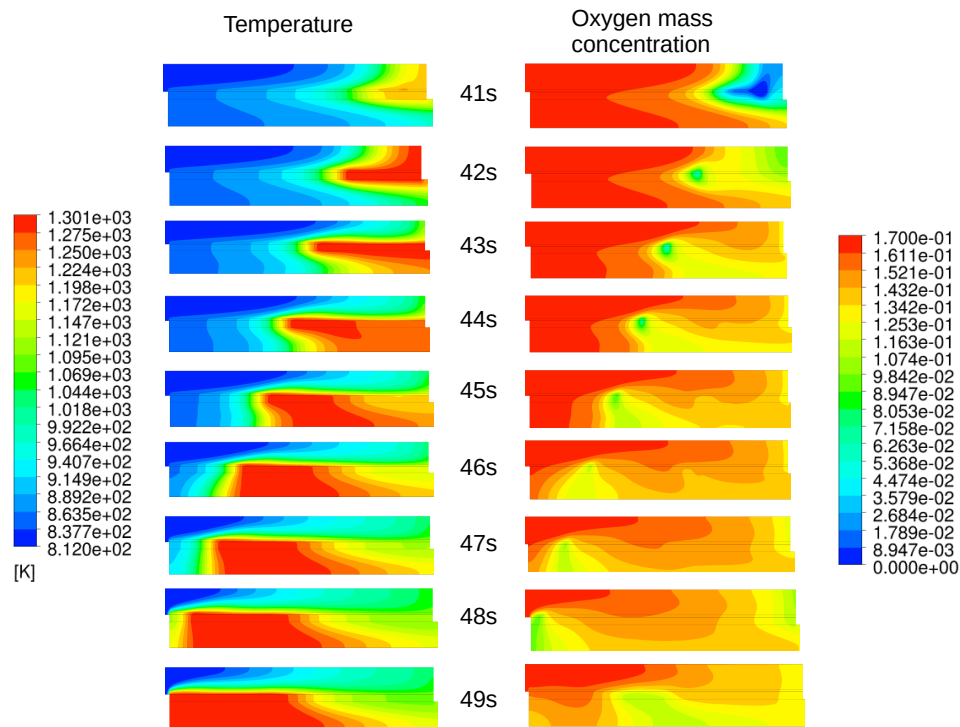


Figure 4.9: Contour plots for temperature and oxygen mass fraction for $k_s = 5$ case.

The movement of the high temperature front opposite to the flow direction can be caused by either depletion of oxygen or depletion of soot. Sarli and Benedetto (2015) report that the front they observe moves upstream towards lower temperature and higher oxygen concentrations and from their plots it can be observed that oxygen is depleted where the front is. They also observe a front moving downstream afterwards; they conclude that the downstream front moves backwards due to the lack of oxygen needed for the combustion and also because the soot concentration becomes very low where the front is situated and where much soot is burned. In the result presented in Figure 4.8 however, only a front moving upstream is observed. The simulation crashes after 55 s, but the soot in the domain is almost depleted at this point so that a front moving backwards would not occur even if the simulation would proceed. In this case, the moving of the front is found to be caused by lack of soot and not by lack of oxygen; This can be observed from the contour plots of temperature and oxygen mass fraction in Figure 4.9.

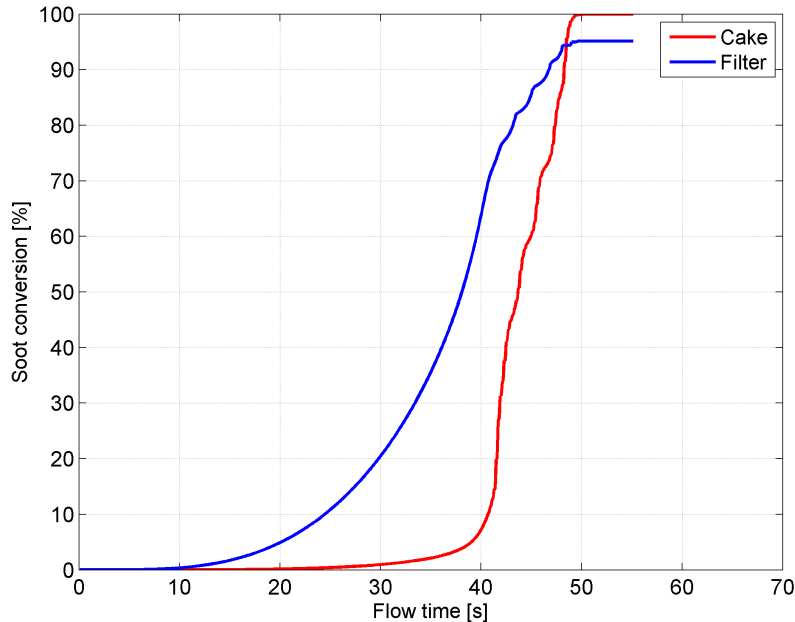


Figure 4.10: Soot conversion calculated from soot mass concentration registered at the monitor points in the filter and cake for $k_s = 5$ case, using an explicit formulation of the source term, with temperature limited to 1300 K and updating the flow field every 10 time steps.

Sarli and Benedetto (2015) also conclude from their result that catalyzed soot oxidation in the filter acts as a pilot to ignite the soot in the cake. This can also be seen from comparison of the results for soot conversion for $k_s = 5$ (Figure 4.10) with the soot conversion in the cases $k_s=0$ and $k_s=1$: at the present temperature of 813 K and low catalytic activity, soot oxidation in the cake is occurring only at very low rates. Under high catalytic activity the soot cake is consumed at high rates though, even though there is much less soot in the filter compared to the soot cake. Hence, the model from this thesis shows this effect of the filter as well. However, it has to

be noted that the soot in the filter should be fully consumed earlier than the soot in the cake, but the soot conversion plot shows the opposite; hence the reliability of the result for the last time steps is questionable.

4.3 The 2D open flow model

In order to develop the open flow model, simulations are coupled with experiments. The previously reported experimental results provide both initial conditions and boundary conditions for the simulations. The kinetics used in the 2D model are then tuned so as to achieve the temperature profile predicted by the experiments. The input data for soot oxidation experiments can be found in Section 3.1.5 and kinetics reported by both Darcy et al. (2007) and Neeft et al. (1997) can be found in Section 2.3.2 in Table 2.1. Results from the simulations made as well as comparisons between experimental and computational runs made are presented below.

4.3.1 Simulation of soot oxidation experiment 1

General flow field

The flow field from a flow and energy simulation using conditions corresponding to experiment 1 is used here to assess the flow field developed in the open flow domain. Figure 4.11 gives the velocity flow field. Here the velocity is highest in the open flow channel as indicated by the red colour in the domain while a much lower velocity is predicted at the inlet of the domain. The velocity increase is due to the change in cross-sectional area upstream. In addition, an increase in velocity is observed in the open flow channel when soot oxidation occurs, this increase in velocity is probably due to the exothermic soot oxidation reaction. The lowest velocity is predicted in the regions closest to the outer wall of the open flow model, this is due to the non-slip boundary condition implemented on the outer walls of the model. Furthermore a swirl is predicted at the outlet as shown 4.11; the swirl in this case probably arises as a result of flow separation at the outlet occurring due to the abrupt change in cross-sectional area at the end of the substrate. A small amount of flow passes downwards through the soot cake and the porous wall of the filter. There is only very little flow in the lower channels. It is observed that the magnitude of flow velocity increases as the reactions occur; as a result, it can happen that the swirl recirculates a part of the flow back into the lower channels of the substrate. This influences the velocity field and the observed temperatures.

Simulation of soot oxidation experiment 1 using Diesel soot oxidation kinetics

Here, kinetics reported by Darcy et al. (2007) for Diesel soot oxidation are used in the reproduction of the thermal front observed in soot oxidation experiment and the results from this simulation are presented here. A high exotherm of 50 °C upstream and an exotherm of 28 °C downstream at 0.9 s of soot oxidation is obtained; this steep increase also leads to instabilities in the model and eventually to a crash. The kinetic parameters are then modified by tuning the pre-exponential factor. A pre-exponential factor of $3 \times 10^6 \text{ s}^{-1}$ is used and the temperature profile registered by the monitor points in the substrate from this simulation is given by Figure 4.12.

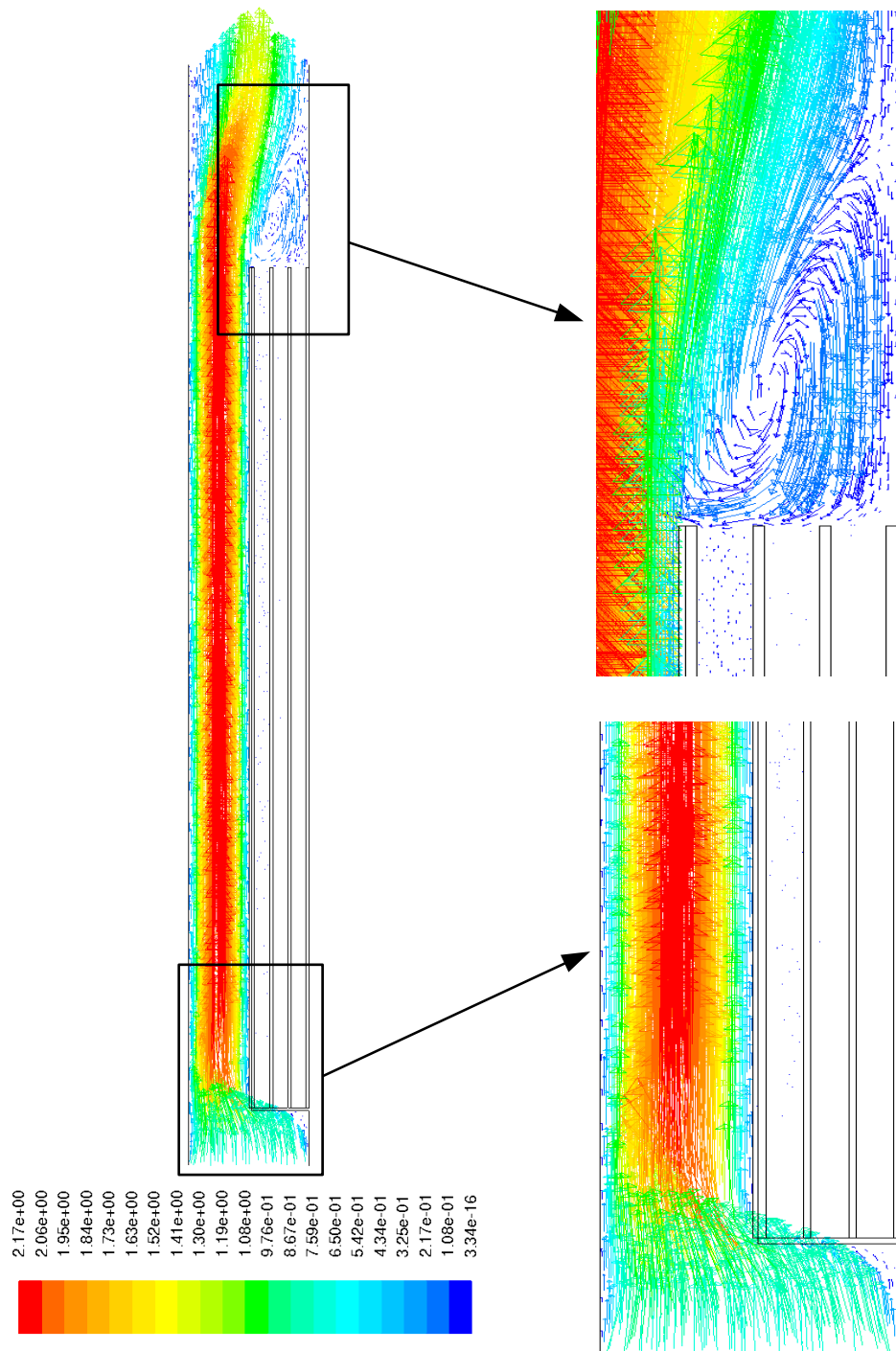


Figure 4.11: Vectors of velocity coloured by velocity magnitude in m/s for the simulation of the soot oxidation experiment 1 (domain scaled in y direction). A zoomed in version of the inlet (left) and outlet (right) is also given. Red indicates highest velocity and dark blue is lowest.

The temperature profile obtained for Darcy kinetics with a pre-exponential factor of $3 \times 10^6 \text{ s}^{-1}$ is still significantly different from the one obtained in the experiment run. Temperatures lower than those observed during the experiment are registered upstream (TC1). This could be due to low reaction rates upstream as a result of the low temperature of the gas mixture at the inlet. An exotherm of $187 \text{ }^\circ\text{C}$ is obtained downstream (TC5); this is still quite high as compared to the $70 \text{ }^\circ\text{C}$ exotherm observed in the experiment. Furthermore, the exotherm is obtained much later than in the experiment run. However, the temperature predicted by the model is highest at the outlet, consistent with the experimental run. However, overall too high temperature peaks are registered in the middle (TC3) and downstream compared to those measured in the experiments. Also, the temperatures should have reached their maximum values by 27 s, but the trend in the simulation is still towards higher temperatures. Due to these inconsistencies, it is concluded that the Diesel soot oxidation kinetics used in the model cannot accurately describe the kinetics used in the experiment. Hence, another set of kinetics is used and the obtained result will be described in detail in the following section.

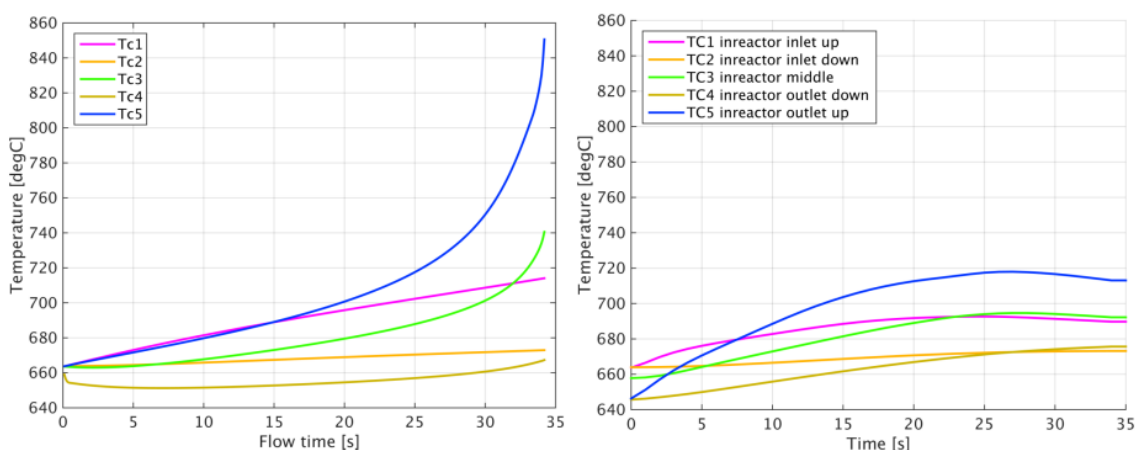


Figure 4.12: Temperature (in $^\circ\text{C}$) predicted at the monitor points in the substrate (Tc) during soot oxidation simulation using Diesel soot kinetics

Simulation of soot oxidation experiment 1 using Printex-U oxidation kinetics

Here, kinetics reported by Neeft et al. (1997) for Printex-U oxidation are used in the reproduction of soot oxidation experiment 1. This is done since Printex-U was used in the experiments. The temperature profile developed in the substrate as registered by monitor points in the substrate during soot oxidation simulations with Printex-U kinetics is given in Figure 4.13. Here, generally a step increase in temperature is observed for monitor points TC1 and TC5 corresponding to inlet and outlet positions in the reactor respectively. At low temperatures in the reactor i.e. in the first 10 s of oxidation, axial gradients between these two monitor points are very small and thus a similar rate of increase in temperature is registered upstream and downstream; this is inconsistent with the big axial gradients measured by the

experiment at this flow time. The small axial gradients predicted by the model could be both due to the very porous cake layer and 'open flow effects' in the domain: here the gas mixture is not blocked but rather flows axially along the domain and in so doing, convects heat through the very porous cake layer. As a result heat is equally distributed in the cake layer thus setting off soot oxidation at the same rate along the cake. Consistent with the experiment run, lower temperatures are registered in the middle (TC3) as compared to the upstream (TC1) and downstream (TC5) regions. This could probably be due to the middle monitor point being on a lower radial level as compared to the upstream and downstream points i.e. TC1 and TC5 are closer to the surface of the substrate as compared to TC3. Therefore, the temperature registered in the middle monitor point is much lower than the temperature that would be measured closer to the surface where the reaction takes place.

After 13 s flow time, axial temperature gradients between monitor points TC1 (upstream) and TC5 (downstream) become bigger and thus lower temperatures are registered upstream as compared to downstream. This trend is in agreement with the experiment run, although the change occurs already at 8 s in the experiments. The fact that temperatures downstream become higher could be a result of two different effects: cooling effect of the gas mixture at the inlet that comes in at 659 °C, which is lower than the approximately 690 °C acquired after soot oxidation at 15 s. Furthermore, the temperatures downstream benefit from the heat released by the reactions occurring in the middle and upstream of the reactor. These two effects therefore introduce an axial temperature gradient between upstream and downstream regions resulting into varying reaction rates in these regions. Axial gradients that are bigger as compared to those measured by the experiment are predicted by the model between monitor points TC2 (furthest down in the substrate upstream) and TC4 (furthest down in the substrate downstream). These two points also register very low temperatures. This could be due to the less porous filter wall. Here minimal flow of the gas mixture through the porous wall is observed and therefore the amount of heat convected by the gas mixture to these regions is minimal. Furthermore, the temperature at TC4 could be influenced by cool air that is sucked into the lower outlet channels due to the swirl at the end of the substrate. The radial gradient pattern between TC1 and TC2 and between TC5 and TC4 is in accordance with the experiment run 1 but of different magnitudes; Especially the radial difference between TC1 and TC2 is much less compared to that measured in the experiment.

At 21 s (indicated by the black line in the plot), the predicted order of measured temperature magnitudes (pattern) is still in agreement with the experimental result. However, steeper temperature increases are predicted by the model as compared to the more gradual temperature increase measured by the experiment at this time.

A high temperature of 807 °C is later attained at 25 s which in turn causes instabilities in the model and thus a crash. However, this temperature run-away is not observed in the experimental run conducted; the maximum temperature is reached at roughly 27 s in the experiments and afterwards temperatures decrease again. In addition, the steep rise in temperature registered by both upstream and downstream monitor points starts much later than the measurement in the experiment. In the latter the steep increase in temperature starts at soon as the oxidation begins as opposed to the 13 s start for the simulation run. A possible explanation to this would

be that either the kinetics used do not fit the soot oxidation experiment or that the model used does not accurately describe the reactor. However, the model predicts the same pattern like the one measured by the experiment even if the temperature profiles registered by both model and experiment are different.

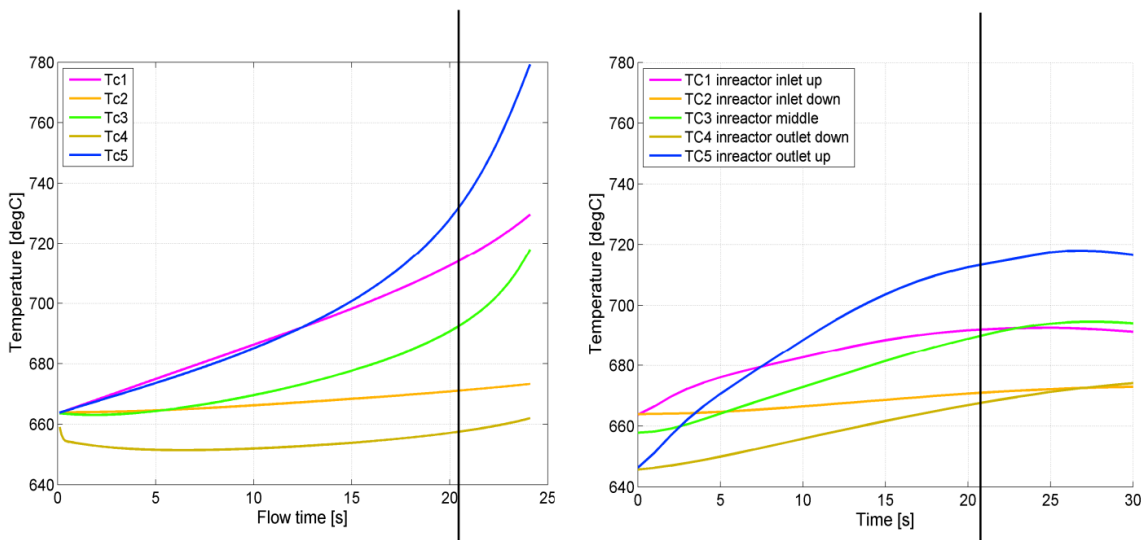


Figure 4.13: Temperature (in °C) predicted at the monitor points in the substrate (Tc) during soot oxidation simulation using *Printex-U* kinetics (left) and temperature measured during the experiments (right).

In order to monitor the consumption of soot during soot oxidation, monitor points are placed in the cake layer at the upstream (C1), middle (C3) and downstream (C5). Their axial positions correspond to those of the temperature monitors TC1, TC3 and TC5. Figure 4.14 gives the consumption of soot in the cake with time registered in the aforementioned monitor points. The trend predicted here shows that the axial variations in the temperatures predicted at the inlet and outlet do arise due to reaction that leads to consumption of soot; i.e soot is consumed at different rates in all the cake domain. However, it is not possible in this work to verify this trend since local soot concentration in the reactor during soot oxidation experiments was not measured. It is observed from the soot concentration plot that more soot is consumed in the middle (TC3) as compared to the downstream region (TC5). From this trend therefore, since more soot is consumed in the middle, a higher reaction rate and thus higher temperatures are expected in the middle as compared to the outlet. This was however not observed from the temperatures measured in both the simulation and experiment runs. In order to investigate this occurrence further, the soot reaction rate along the axial length of the cake layer is plotted for different soot oxidation times (Figure 4.15).

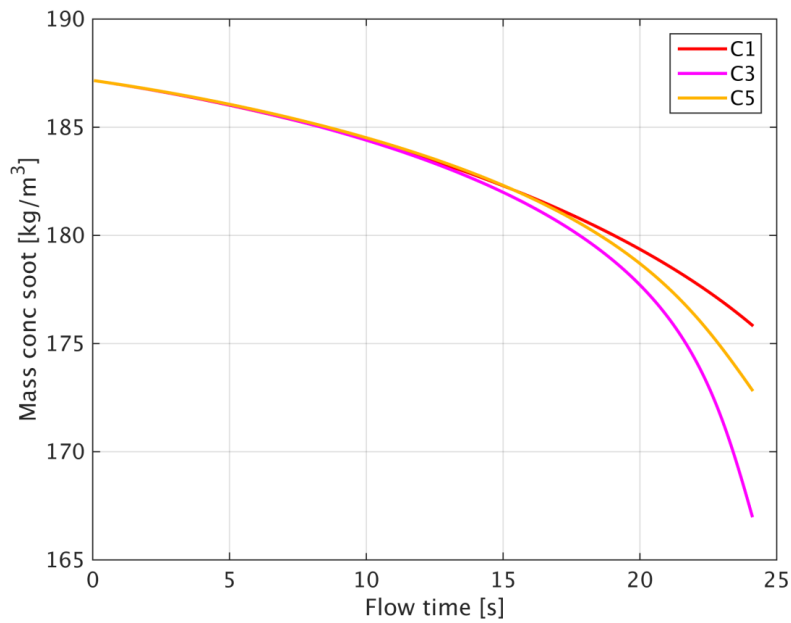


Figure 4.14: Mass concentration of soot as registered in monitor points in the soot cake (C) during soot oxidation simulation using Printer-U kinetics

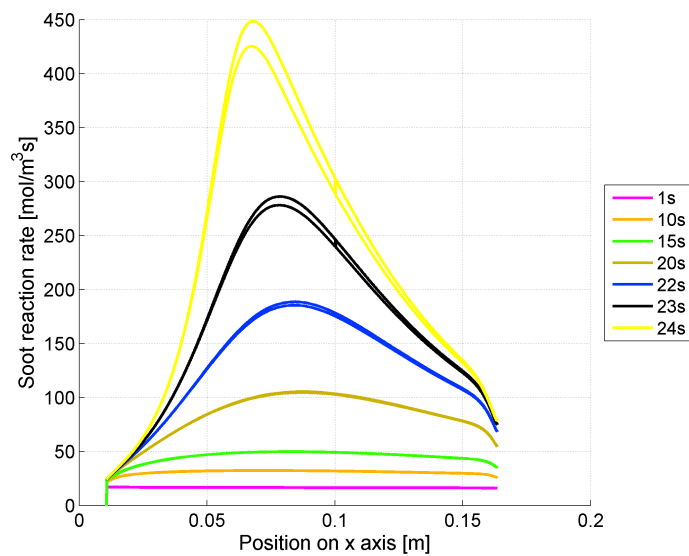


Figure 4.15: Reaction rate in the cake along the substrate length plotted for different points in time.

From Figure 4.15, the reaction rate along the cake layer is shown to increase as the soot oxidation progresses in time. The increase in reaction rate is more inclined towards the middle of the cake layer to the extent that at 24 s, the highest reaction rate is registered in the middle of the cake layer. Thus its expected that the highest temperature is registered in the middle and not at the outlet as indicated by both the experiment and simulation. It is concluded that the lower temperature measured

in the middle as compared to the outlet in both experiment and simulation is due to the thermocouple placement. Here, since the middle thermocouple is further away from the surface of the cake layer, the exact increase in temperature of the cake layer in the middle due to the soot oxidation experiment is not measured. Furthermore, radial temperature differences have been observed to increase as the temperature increases; these also affect the accuracy of the thermal front temperature measurement. Therefore in order to correctly measure the temperature profile developed during soot oxidation, thermocouples should be placed as close to the surface of the soot cake layer as possible in order to minimize the large radial gradients that arise at high temperatures.

The evolution of the thermal front and the respective flow field for oxygen developed during soot oxidation using Printex-U kinetics is given in Figures 4.16 and 4.17. The first second of the soot oxidation shows an exotherm that burns uniformly in the cake layer at a temperature of 941 K. This low temperature results into low reaction rates in the entire cake layer and thus minimal consumption of oxygen as shown in the 1s contour plot for oxygen mass fraction (Figure 4.16). A gradient in the oxygen mass fraction develops at 2 s downstream. This is an indication of higher reaction rates and thus higher temperature downstream as compared to the rest of the cake layer. At 10 s (Figure 4.17), the gradients in oxygen mass fraction increase and extend as far as 30% of the cake layer (orange section). To this end, an oxygen mass fraction of 0.158 is registered. This therefore indicates a low consumption of oxygen by the reaction and thus a low temperature exotherm of 973 K in the middle and downstream regions of the cake layer. From 10 s to 24 s, the exotherm increases as more oxygen is consumed by the reaction. At 25 s the consumption is so high that a depletion of oxygen in the downstream and middle region of the domain occurs. The depletion of oxygen at 25s is probably due to high reaction rates in the middle of the cake layer and thus high consumption of oxygen. These big gradients cause the model to crash after 25 s.

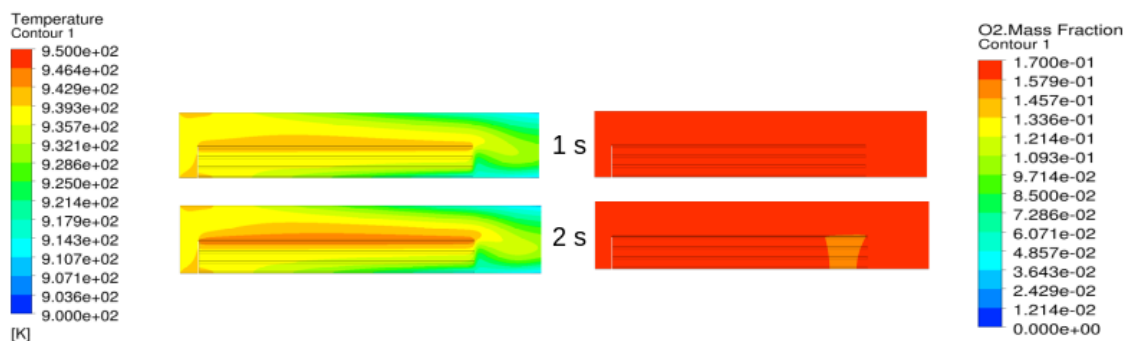


Figure 4.16: Contour plots for temperature (in K) and O_2 concentration in the first two seconds of flow. It can be seen that at 1 s the soot is already reacting homogeneously along the substrate length.

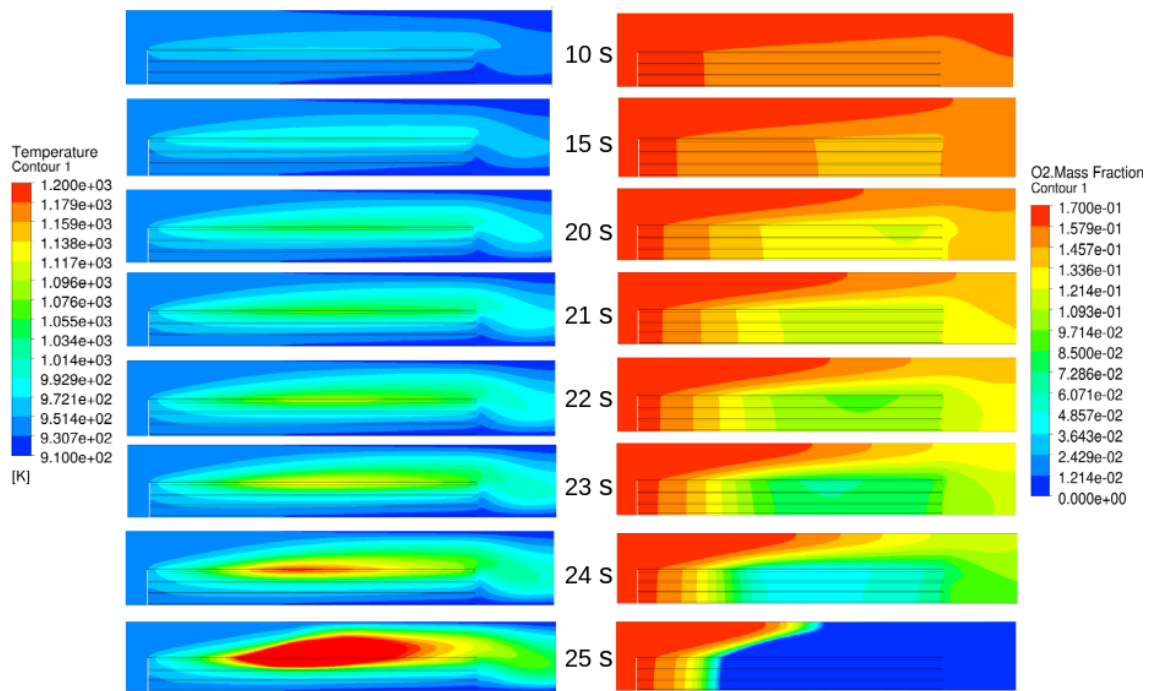


Figure 4.17: Contour plots for temperature (in K) and O_2 concentration for different points in time. Note the different scale in comparison to the previous picture. The red zone in the temperature plot for 25 s represents all temperature above 1200 K; the highest obtained temperature is 1673 K and is situated in the middle of the substrate.

4.3.2 Mass transfer effects

One of the objectives of this study was to investigate the occurrence of a moving thermal front in the open flow reactor since the occurrence of moving thermal fronts is most likely to occur when an engine that was initially operated at high load drops into idle mode. This results into a low gas flow rate and hence low cooling effects. The soot will react when the conditions are beneficial and consume the available oxygen at rates that might exceed the available oxygen. Hence, oxygen depletion occurs and according to Sarli and Benedetto (2015) this will result into a movement of the thermal fronts. Moving thermal fronts can also occur due to soot depletion as has been concluded earlier from the DPF study. This has however not been observed in both the simulation and experiment run. Hence, it is assumed that neither of these prerequisites has been met in the open flow reactor experiments. The possibility of having oxygen depletion in the open flow reactor is investigated here through studying the mass transfer effects in the reactor using the CFD model for the open flow reactor. Steady state simulations are conducted as described in Section 3.2.7 and the solution from the steady state simulations are used here to assess the mass transfer effects in the reactor. Three different velocities are investigated.

0.7408 m/s steady state simulation

0.7408 ms^{-1} velocity that was used in the soot oxidation experiment 1 is used here. From Figure 4.18 the velocity profile at the entrance to the porous part of the reactor is in the developing region; however at 5% length of the cake layer, a fully developed velocity profile is attained. Figure 4.19 shows the development of a boundary layer of O_2 along the axial length of the cake. The boundary layer is thin at the inlet and becomes wider along the axial length of the cake layer length. Initially, the thin boundary layer at the inlet of the reactor given in Figure 4.20 is due to the fact that the profiles in this region are still developing. In addition, low temperatures at the inlet result into kinetic limitations in accordance with Hayes and Kolaczkowski (1999) who reports that the operation at the reactor inlet is most usually kinetically controlled due to the low temperatures at the inlet. From 30% of the cake layer length, the boundary layer gets wider and spreads over the whole channel height. A view of the outlet is given in Figure 4.21.

Furthermore, more oxygen is consumed in the middle, resulting into less oxygen reaching the downstream region. Here, 80% of the oxygen coming in at the inlet reaches the middle of the reactor while only 45% of the oxygen coming in at the inlet reaches the outlet. However even if low oxygen concentrations are delivered to the outlet, a depletion of oxygen is not obtained at the conditions investigated. Therefore, with the assumption of instantaneous reactions occurring in the cake layer, no oxygen depletion is observed in the reactor set up at the conditions investigated i.e. at high residence time with velocity of 0.7408 ms^{-1} for the gas mixture.

From the concentration field simulated by the model, a global steady state Sherwood (Sh) number is calculated as described in Appendix J (Section J.1.1). A steady state global Sh number of 2 that is independent of mesh refinement is obtained for the reactor at the conditions investigated. The Sh number obtained here is in agreement with the Sh number reported by Wang-Hansen et al. (2011) for theoretical minimum Sherwood number for flow in a monolithic square channel. Wang-Hansen et al. (2011) reports the theoretical Sh_{min} as given by hydraulic diameter divided by the maximum film thickness. Sh_{min} of 2 is reported by them for flow in a monolithic square channel with mass transfer occurring to all bounding surfaces. However, in the case of this work mass transfer occurs only to the soot cake on the filter surface as soot is applied only to the surface of the substrate. Hence, the maximum film thickness is equal to the hydraulic diameter of the channel, resulting in a theoretical Sh_{min} of 1. Sh number also depends on flow, reaction rate and channel geometry according to Ekstrom (2005); hence, the Sh number is expected to change as these factors change. To this, Hayes and Kolaczkowski (1994) reports a value of Sh number ranging from 3.8 to 4.4 for a fully developed flow in a single monolith square channel which depends on the reaction conditions. Tronconi and Forzatti (1992) roughly agrees with this range.



Figure 4.18: Contour plot showing the fully developed velocity profile in the 0.7408 ms^{-1} steady state simulation case. The red zone in the contour plot represents the highest velocity (2.17 ms^{-1}) while the dark blue zone represents zero velocity.

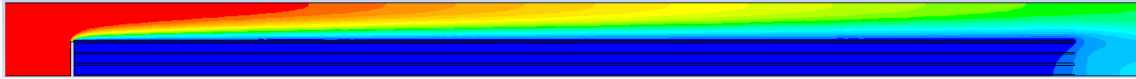


Figure 4.19: Contour plot showing flow field of O_2 in the 0.7408 ms^{-1} steady state simulation case. The red zone in the contour plot represents maximum mass fraction of oxygen (0.168) while the dark blue zone represents the lowest oxygen mass fraction (0.0)

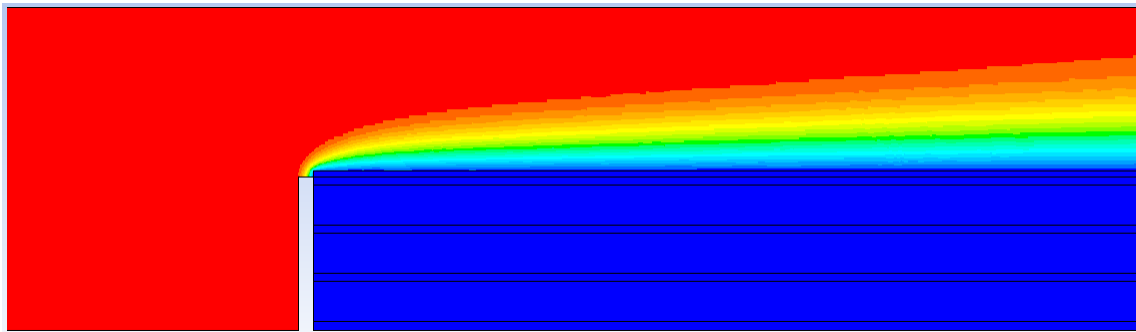


Figure 4.20: Contour plot showing flow field of O_2 at the inlet during the 0.7408 ms^{-1} steady state simulation case. The red zone in the contour plot represents maximum mass fraction of oxygen (0.168) while the dark blue zone represents the lowest oxygen mass fraction (0.0)

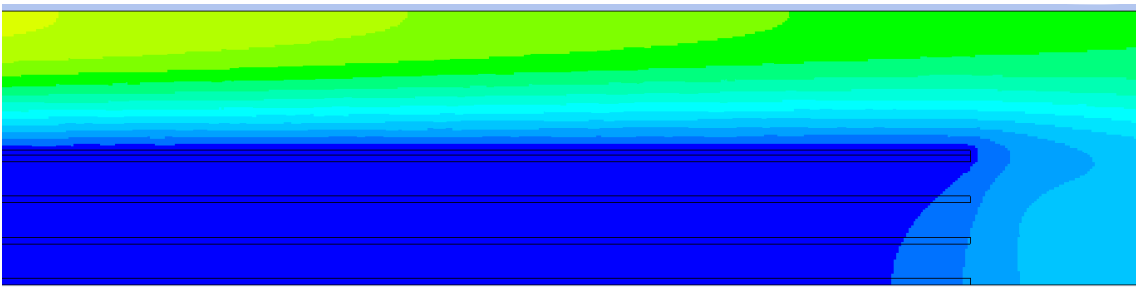


Figure 4.21: Contour plot showing flow field of O_2 at the outlet during the 0.7408 ms^{-1} steady state simulation case. The red zone in the contour plot represents maximum mass fraction of oxygen (0.168) while the dark blue zone represents the lowest oxygen mass fraction (0.0)

15.3 m/s steady state simulation

The mass transfer effects in the reactor are also assessed as a function of residence time corresponding to Sarli and Benedetto (2015) inlet condition; the open flow geometry is used. Here a velocity of 15.3 m s^{-1} is used that corresponds to a residence time of 0.01 s that was used by Sarli and Benedetto (2015). Results from this simulation are presented here. Figure 4.22 shows the developing velocity profile predicted by the model in the 15.3 m s^{-1} case. Here the entire axial length of the domain is in the developing region in contrast to the 0.7408 m s^{-1} case (Figure 4.18). The boundary layer developed in the 15.3 m s^{-1} case is given by Figure 4.23. Here, a boundary layer is formed at the inlet and generally increases along the axial length of the cake layer. However the boundary layer predicted in Figure 4.23 is much thinner in comparison to that predicted the 0.7408 m s^{-1} steady state simulation and does not cover the height of the channel at any point (Figure 4.19). Furthermore, the boundary layer at the inlet (Figure 4.24) in the 15.3 m s^{-1} case is much more thin as compared to the one observed in the 0.7408 m s^{-1} case (Figure 4.20). In the former, the thin boundary layer is a result of the developing velocity profile that stretches along the entire axial domain (Figure 4.22). Due to the thin boundary layer, oxygen is effectively transported towards the cake layer. In contrast to the 0.7408 m s^{-1} case, oxygen is uniformly consumed in the domain resulting in equal amounts of oxygen reaching both the middle and the downstream region. Furthermore, the boundary layer at the outlet as shown in Figure 4.25 is much thinner as compared to that predicted by the 0.7408 m s^{-1} case (Figure 4.21) which results into more oxygen being transferred towards the cake layer at the outlet in the 15.3 m s^{-1} as compared to the 0.7408 m s^{-1} case. As was predicted in the 0.7408 m s^{-1} case, the model also predicts no oxygen depletion in the 15.3 m s^{-1} case at the conditions investigated. Therefore from this assessment, with the assumption of instantaneous reactions in the cake layer, it can be concluded that decreasing the residence time that the gas mixture takes in the open flow reactor would positively impact the transport of oxygen in the reactor, but no oxygen depletion would be observed in the reactor set-up at these conditions.

The concentration field simulated by the model in the 15.3 m s^{-1} case is used to calculate a global steady state Sherwood (Sh) number as described in Appendix J (Section J.1.2). Due to the very high velocity used, an unsteady solution is generated that gives a Sh number that is dependent on the mesh. Therefore, the grid is refined with respect to the gradient of oxygen mass fraction so as to be able to resolve the boundary layer and also so as to obtain a Sh number that is independent of the mesh. To this end, a global Sh of 8 that is independent of mesh refinement is obtained. The Sherwood number would have been expected to be in the range reported by Hayes and Kolaczowski (1994) and Tronconi and Forzatti (1992) for laminar flow in monolithic channels (e.g. between 3 and 4.4) However, the reported ranges are valid for fully developed flow, and in the present case entrance effects are present that stretch over the entire axial length of the domain and result into a developing velocity profile along the axial length of the domain. This unsteady behaviour could be the reason for the higher Sherwood number, as well as differences between the present geometry and a typical monolith channel (e.g. height). This statement is

supported by the fact that the local Sherwood numbers reported by Tronconi and Forzatti (1992) are higher in the inlet region than further in the reactor, which is due to that the flow is still developing. Furthermore, a high Reynolds number of 1010 that arises as a result of thermally induced instabilities in the domain is obtained.

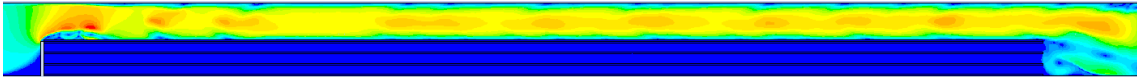


Figure 4.22: Contour plot showing the developing velocity profile in the 15.3 ms^{-1} steady state simulation case. The red zone in the contour plot represents the highest velocity (52.98 ms^{-1}) while the dark blue zone represents zero velocity.



Figure 4.23: Contour plot showing the flow field of O_2 developed in the 15.3 ms^{-1} steady state simulation case. The red zone in the contour plot represents maximum mass fraction of oxygen (0.168) while the dark blue zone represents the lowest oxygen mass fraction (0.0).

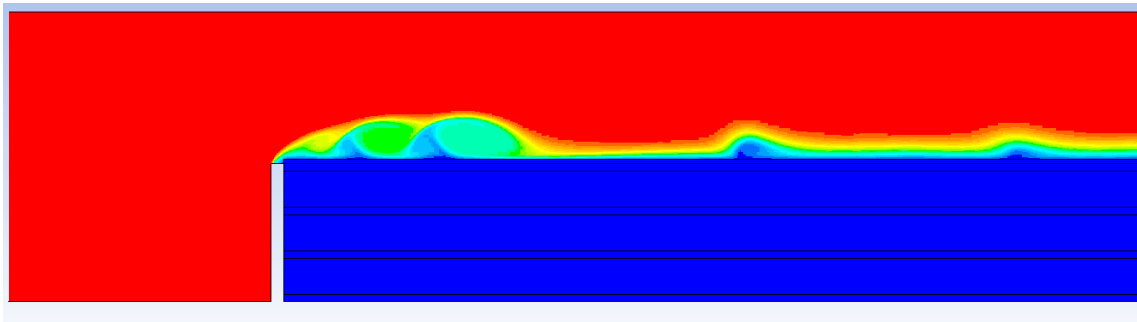


Figure 4.24: Contour plot showing flow field of O_2 at the inlet in the 0.7408 ms^{-1} steady state simulation case. The red zone in the contour plot represents maximum mass fraction of oxygen (0.168) while the dark blue zone represents the lowest oxygen mass fraction (0.0).

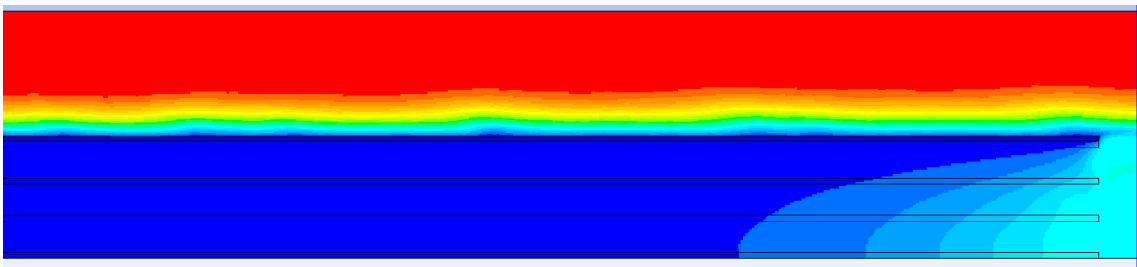


Figure 4.25: Contour plot showing mass fraction of O_2 at the outlet during the 15.3 ms^{-1} steady state simulation case. The red zone in the contour plot represents maximum mass fraction of oxygen (0.168) while the dark blue zone represents the lowest oxygen mass fraction (0.0).

0.224 m/s steady state simulation

The velocity of the gas mixture is decreased further to assess the possibility of oxygen depletion in the reactor. A velocity of 0.224 m s^{-1} is used in the steady state simulation and results from the simulation are presented here. From Figure 4.26 the velocity profile at the entrance to the porous part of the reactor is in the developing region, which is in agreement with the velocity profile predicted in the 0.7408 m s^{-1} case. However, in the 0.224 m s^{-1} case the fully developed velocity profile is obtained much earlier; at approximately 1% length of the cake layer. This is probably due to the lower velocity in the latter. The boundary layer developed in the 0.224 m s^{-1} case is given in Figure 4.27. Here, the boundary layer is thin at the inlet (see Figure 4.28) and becomes wider along the cake layer length until it covers the whole open channel in agreement with the 0.7408 m s^{-1} case. In the 0.224 m s^{-1} case however, the boundary layer gets wider and covers the whole channel from approximately 20% of the cake layer length; this is observed earlier in the 0.224 m s^{-1} case than in the 0.7408 m s^{-1} case. Furthermore, in contrast to the 0.7408 m s^{-1} case, only 30% of the oxygen coming in at the inlet reaches the middle of the reactor and only 5% of the oxygen coming in at the inlet reaches the outlet. This suggests more effective oxygen transfer to the surface upstream. This effective transport of oxygen occurs much earlier than in the 0.7408 m s^{-1} case thus resulting into lower oxygen concentrations reaching both the middle and downstream regions. Furthermore, oxygen depletion is predicted by the model at the outlet in the 0.224 m s^{-1} case as shown by Figure 4.29. The oxygen depletion is due to that oxygen has been consumed by reaction upstream. Therefore from this assessment, with the assumption of instantaneous reactions in the cake layer, it can be concluded that at very low gas flow rates would negatively impact the oxygen transport in the open flow reactor, but oxygen depletion could be achieved at these conditions.

From the concentration field simulated by the model in the 0.224 m s^{-1} case, a global steady state Sherwood (Sh) number is calculated as described in Appendix J (Section J.1.3). A steady state global Sh number of 0.91 that is independent of mesh refinement is obtained for the reactor at the conditions investigated. This is close to the theoretical minimum Sherwood number of 1.



Figure 4.26: Contour plot showing the fully developed velocity profile in the 0.224 m s^{-1} steady state simulation case. The red zone in the contour plot represents the highest velocity (0.665 m s^{-1}) while the dark blue zone represents zero velocity.



Figure 4.27: Contour plot showing the flow field of O_2 developed during the 0.224 m s^{-1} steady state simulation case. The red zone in the contour plot represents maximum mass fraction of oxygen (0.168) while the dark blue zone represents the lowest oxygen mass fraction (0.0).

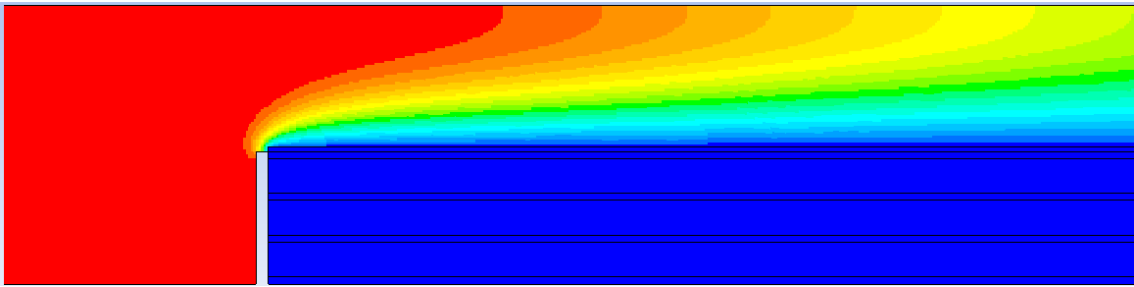


Figure 4.28: Contour plot showing the flow field of O_2 developed at the inlet during the 0.224 ms^{-1} steady state simulation case. The red zone in the contour plot represents maximum mass fraction of oxygen (0.168) while the dark blue zone represents the lowest oxygen mass fraction (0.0).

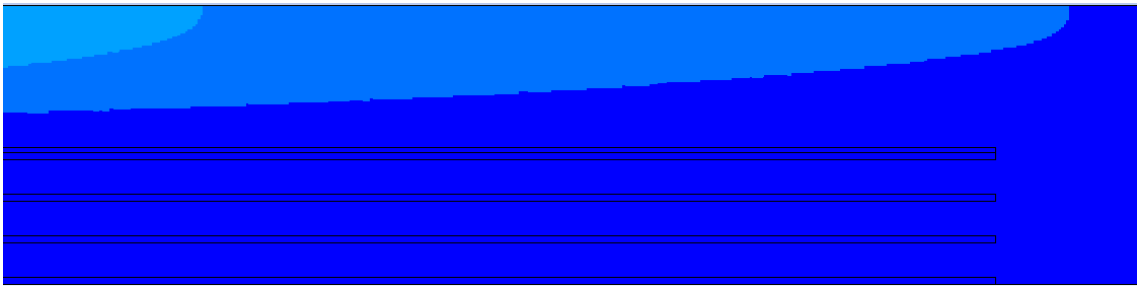


Figure 4.29: Contour plot showing the flow field of O_2 developed at the outlet during the 0.224 ms^{-1} steady state simulation case. The red zone in the contour plot represents maximum mass fraction of oxygen (0.168) while the dark blue zone represents the lowest oxygen mass fraction (0.0).

5

Conclusion and outlook

The aim of this thesis was to investigate the occurrence of steep temperature increases (thermal fronts) during soot oxidation in a DPF via an open flow-reactor. To do this, an experimental set-up for an open-flow reactor was developed using a part of a cordierite monolith as substrate. Experiments were then conducted under different conditions to provoke a thermal front. Furthermore, a CFD model was developed that could predict the temperatures in the reactor at hand. In the following, the main conclusions from this work concerning experimental result, CFD model and occurrence of thermal fronts will be summarized.

Soot oxidation experiments have been successfully conducted in the experimental set-up and temperature, pressure and production of CO and CO₂ can be recorded. The result showed significant peaks in temperatures for experiment 1 and experiment 3, where the highest temperature peak was measured towards the outlet of the reactor and the lowest towards the reactor inlet during the whole soot oxidation period. Experiment 2 (lowest O₂ concentration and soot mass) did not show a steep increase and it was concluded that the conditions used were not favorable for high temperature peaks in this case. Axial differences in temperature are always present in the current experimental set-up, where the temperature at the inlet is highest and the temperature at the outlet is lowest. Radial differences are small at steady state, but increase during soot oxidation.

Furthermore, a model for soot oxidation was developed. It was verified by comparison with results from a numerical study on DPF by Sarli and Benedetto (2015) and afterwards the model was used to simulate the open-flow reactor at hand. From verification of the model through comparison with results reported by Sarli and Benedetto (2015) it can be concluded that the model developed in this work is able to predict soot oxidation at low temperatures and/or low catalytic activity. The finding of Sarli and Benedetto (2015) that the soot in the filter acts as a pilot for the cake is supported by this work. However, divergence occurs when the temperature gets too high and the reaction rate is too high: hence the steep temperature increases that characterize a thermal front can not be captured. This is observed in both the comparison with Sarli and Benedetto (2015) and when developing the 2D model for simulation of the experiments: the simulation crashes when temperatures and reaction rates become too high. Possible reasons for these crashes can be numerical issues, as well as inappropriate model assumptions. For example, oversimplification of the structure and transient behaviour of the cake layer could be a problem. A temperature limit makes prediction of a steep temperature increase possible, but the result is affected: As observed from the simulation for $k_s = 5$, the consumption of soot is predicted to be more rapid as in comparison with the result

reported by Sarli and Benedetto (2015). Also, the limit has to be known and the limit value can have a great influence on the outcome of the simulation. In order to improve the simulation stability, it is recommended to further investigate to find more appropriate model inputs for the viscous resistance and porosity of cake and filter. Also, improvements could be made in how the equations are being solved to achieve better convergence. It also has to be mentioned that there are oscillations in the results by Sarli and Benedetto (2015) that are not explained in the paper and that do not seem to have a physical explanation. Also, their analysis is a fictive increase of catalytic activity and no validation of their model with experiments has been given. Hence, the simulation problem at hand can be regarded as generally very challenging and sensitive to all parameters in the system.

Prediction of the temperature pattern in the open flow reactor simulation was successful, however the pattern is shifted in time compared to the experiments and the simulation crashes as mentioned before. Also, the overall predicted temperatures are too high with the conditions used in the simulation. Hence, it is concluded that correct kinetic parameters that fit the experimental set-up at hand have a strong influence on the simulation predictions (Activation energy, pre-exponential factor, order of reaction for soot and oxygen). It is furthermore concluded that kinetics of Diesel soot and Printex U are different and that the kinetics fitting to the type of soot at hand have to be implemented to reproduce an experimental result. Another aspect that affects the accuracy of the simulations for the experiments is the assumption of full selectivity for CO_2 , whereas in reality CO is a big fraction of the oxidation products. For further improvement, the selectivity for CO respectively CO_2 should be taken into account. Furthermore, a more precise model for the soot cake layer could improve accuracy. Also, the simulation of the open flow case shows a swirl at the outlet that recirculates cold air from the outlet back into the substrate channels. In reality some of these channels are blocked by the thermocouples. This is not accounted for in the simulation.

From the findings of this work and the findings of Sarli and Benedetto (2015) it is concluded that a thermal front moves across the substrate as a result of depletion of soot or depletion of oxygen. If possible, a front moving across the substrate was desired in the experiments, since thermal fronts are likely to occur when a vehicle runs under high load and then drops to idle mode. Very low flow velocities and low cooling efficiency characterize the idle mode and a soot oxidation at this stage can result in low oxygen concentrations due to lack of transport of new oxygen to the reaction sites. The lack of oxygen or soot causes the front to move in direction of higher oxygen or soot availability. No moving front has been observed in the experiments; hence it is concluded that no depletion of soot or oxygen has been achieved that would have caused the front to move. This was supported by mass transfer assessment of the reactor for instantaneous reaction conditions: at $2 L_n/min$ there is a thick boundary layer towards the outlet, but no total oxygen depletion is achieved. Hence there will be no movement of the thermal front due to oxygen depletion at these conditions. It is furthermore observed from mass transfer studies on the open flow simulation set-up that oxygen depletion can be achieved at lower velocities, which supports the fact that thermal fronts are most likely to occur when the engine drops to idle mode. Such low velocities are however difficult to realize in the

current experiment set-up since decreasing the velocity would result into practical problems with the gas flow needed for the analyzers ($1.2 L_n/min$). Using a lower oxygen concentration as in experiment 1 did also not lead to a thermal front in the reactor for the given experimental conditions; However, the soot loading was lower for this experiment and hence further investigation should be conducted.

Coupling of the experimental result with the open-flow simulation revealed furthermore that the placement of the thermocouples in the substrate is important: The temperature registered in the thermocouple placed in the middle of the substrate in the middle channel in both experiments and simulation was between the temperature registered at the inlet and the temperature registered at the outlet. However, the reaction rate and temperature in the middle of the soot cake was found to be highest in the simulation. Hence, the thermocouples should be placed as close to the soot on the surface as possible, since the temperatures measured further down in the substrate are very much lower than those close to the surface. Inappropriate placement can thus result in a misleading thermal profile. Also, the swirl after the substrate that was found in the simulations could affect the temperatures in the substrate if it is present in reality; it could cause recirculation of flow back into the substrate channels at the outlet and hence influence the temperature there and maybe also further upstream in the substrate. This swirl is found to be more dominant when the flow velocity increases due to higher temperatures resulting from the reactions occurring in the domain.

Studies on DPF as Chen et al. (2009) found moving thermal fronts at similar conditions as used in the experiments of this work, however at a lower space velocity. Hence, further investigations could be made to be able to say if the open flow substrate can be used to observe a moving thermal front.

From the findings of this work it can be concluded that the occurrence of thermal fronts is very dependent on the operating conditions of the reactor used. It is also observed that the flow field of a DPF is very different from an open flow reactor flow field. Hence it is concluded that the conditions needed to provoke a thermal front in the open flow reactor are very different from those needed to achieve a thermal front in an actual DPF. Hence, the open flow reactor can not predict what will happen in a DPF under the same conditions. It is furthermore concluded that blocking the pathway of the gas in the DPF configuration may play a key-role in the evolution of a thermal front.

However, the open substrate could be used for kinetic studies if the temperature control unit is fine-tuned and if an isothermal axial temperature profile can be achieved. Further improvements can be made to make the experimental set-up more tight; for example, an alternative to the ceramic glue should be evaluated. This is especially important if oxidation via NO_x is considered. Also, calibration of the mass flow controllers as well as the pressure sensors should be considered for future work; this has not been done in this study, but is required for improved accuracy.

Bibliography

- ANSYS, I. (2013), 'Ansys fluent user's guide (release 15.0)'. Accessed: 2016-06-08.
URL: <http://148.204.81.206/Ansys/150/ANSYS%20Fluent%20Users%20Guide.pdf>
- Bennett, S. (2009), *Medium/heavy duty truck engines, fuel and computerized management systems*, 3 edn, Delmar Cengage Learning, Clifton Park, N.Y.
- Bennett, S. (2010), *Modern Diesel Technology: Diesel Engines*, Delmar Cengage Learning, Clifton Park, N.Y.
- Bronkhorst, H.-T. B. (2010), *Instructions manual*, Bronkhorst High-Tech B.V, AK Ruurlo, Netherlands.
- Bronkhorst, H.-T. B. (2016), 'Thermal mass flow measurement'. Accessed: 2016-06-15.
URL: http://www.bronkhorst.com/en/products/theory/thermal_mass_flow_measurement/
- Canu, P. (2001), 'Simulation and interpretation of catalytic combustion experimental data', *Catalysis Today* **64**(3-4), 239 – 252. Special Issue: Multiphase Catalytic Reactor Engineering.
- Chen, K., Martirosyan, K. S. and Luss, D. (2009), 'Soot combustion dynamics in a planar diesel particulate filter', *Industrial & Engineering Chemistry Research* **48**(7), 3323–3330.
- Darcy, P., Costa, P. D., Mellottée, H., Trichard, J.-M. and Djéga-Mariadassou, G. (2007), 'Kinetics of catalyzed and non-catalyzed oxidation of soot from a diesel engine', *Catalysis Today* **119**(1-4), 252 – 256. Air Pollution Abatement Catalysis (APAC) Symposium.
- DieselNet, E. I. (2000), 'Emission control catalysts'. Accessed: 2016-06-10.
URL: <https://www.dieselnet.com/tech/catalysts.php>
- DieselNet, E. I. (2012), 'Diesel oxidation catalyst'. Accessed: 2016-06-13.
URL: https://www.dieselnet.com/tech/dpf_wall-flow.php
- Ekstrom, F. (2005), *Catalytic converters for automotive exhaust applications : flow dynamics, mass transfer and optimization*, PhD thesis, Chalmers University of Technology.

- EPA (2001), ‘Latest findings on national air quality’, <https://www3.epa.gov/airtrends/aqtrnd01/summary.pdf>. Accessed: 2016-05-21.
- Fuller, E. N., Schettler, P. D. and Giddings, J. C. (1966), ‘New method for prediction of binary gas-phase diffusion coefficients’, *Industrial & Engineering Chemistry* **58**(5), 18–27.
- Gulati, S. T. (1986), Strength and thermal shock resistance of segmented wall-flow diesel filters, *in* ‘SAE Technical Paper’, SAE International.
- Hatch, S. V. (2012), *Computerized Engine Controls*, 9 edn, Cengage Learning, Inc., Clifton Park, N.Y.
- Hayes, R. E. and Kolaczkowski, S. (1994), ‘Mass and heat transfer effects in catalytic monolith reactors’, *Chemical Engineering Science* **49**(21), 3587–3599.
- Hayes, R. E. and Kolaczkowski, S. (1999), ‘A study of nusselt and sherwood numbers in a monolith reactor’, *Catalysis Today* **47**(1-4), 295–303.
- Heck, R. M., Farrauto, R. J. and Gulati, S. T. (2009), *Catalytic Air Pollution Control: Commercial Technology*, 3 edn, John Wiley and Sons, Inc., Hoboken, New Jersey.
- Horiba (1999), *Infrared analyzer AIA-110 and AIA-120*, 8 edn, Horiba Ltd.
- J. Jung, J. H. Lee, S. S. and Chun, K. M. (2008), ‘Measurement of soot oxidation with no₂-o₂-h₂o in a flow reactor simulating diesel engine dpf’, *International Journal of Automotive Technology* **9**(4), 423–428.
- Johnson, R. W. (2016), *Handbook of Fluid Dynamics*, 2 edn, CRC Press, Boca Ranton, Florida.
- Kim, S. C., Wang, J., Shin, W. G., Scheckman, J. H. and Pui, D. Y. H. (2009), ‘Structural properties and filter loading characteristics of soot agglomerates’, *Aerosol Science and Technology* **43**(10), 1033–1041.
- Kittelson, D. B. (1998), ‘Engines and nanoparticles: a review’, *Journal of Aerosol Science* **29**(5–6), 575 – 588.
- Koltsakis, G. C., Haralampous, O. A., Samaras, Z. C., Kraemer, L., Heimlich, F. and Behnk, K. (2007), Control strategies for peak temperature limitation in dpf regeneration supported by validated modeling, *in* ‘SAE Technical Paper’, SAE International.
- Konstandopoulos, A. G. (2003), Flow resistance descriptors for diesel particulate filters: Definitions, measurements and testing, *in* ‘SAE Technical Paper’, SAE International.
- Konstandopoulos, A. G. and Johnson, J. H. (1989), Wall-flow diesel particulate filters—their pressure drop and collection efficiency, *in* ‘SAE Technical Paper’, SAE International.
- Konstandopoulos, A. G., Kostoglou, M., Skaperdas, E., Papaioannou, E., Zarvalis, D. and Kladopoulou, E. (2000), Fundamental studies of diesel particulate filters:

- Transient loading, regeneration and aging, *in* 'SAE Technical Paper', SAE International.
- Konstandopoulos, A. G. and Papaioannou, E. (2008), 'Update on the science and technology of diesel particulate filters', *KONA Powder and Particle Journal* **26**, 36–65.
- Konstandopoulos, A. G., Skaperdas, E. and Masoudi, M. (2002), Microstructural properties of soot deposits in diesel particulate traps, *in* 'SAE Technical Paper', SAE International.
- Kuwabara, S. (1959), 'The forces experienced by randomly distributed parallel circular cylinders or spheres in a viscous flow at small reynolds numbers', *Journal of the Physical Society of Japan* **14**(4), 527–532.
- Lakshminarayanan, P. A. and Aghav, Y. V. (2010), *Modeling Diesel Combustion*, 1 edn, Springer Netherlands.
- Lee, K. W. and Gieseke, J. A. (1979), 'Collection of aerosol particles by packed beds', *Environmental Science & Technology* **13**(4), 466–470. Accessed: 2016-05-20.
- McQuarrie, Donald A., R. P. A. G. E. B. (2011), *General Chemistry (4th Edition)*, University Science Books.
- Mollenhauer, K. and Tschöke, H. (2010), *Handbook of Diesel Engines*, Springer, Heidelberg, Berlin.
- Neeft, J. P., Nijhuis, T., Smakman, E., Makkee, M. and Moulijn, J. A. (1997), 'Kinetics of the oxidation of diesel soot', *Fuel* **76**(12), 1129 – 1136.
- NIST (2016), 'Nist web book entry: Carbon dioxide'. Accessed: 2016-05-22.
URL: <http://webbook.nist.gov/cgi/cbook.cgi?ID=C124389&Mask=1>
- Pletcher, R. H., Tannehill, J. C. and Anderson, D. (2012), *Computational Fluid Mechanics and Heat Transfer*, 3 edn, CRC Press, Boca Ranton, Florida.
- RS (2013), *Data sheet: Mineral Insulated Thermocouples*, 14 edn.
- Sampara, C. S. (2008), Global Reaction Kinetics for Oxidation and Storage in Diesel Oxidation Catalysts, PhD thesis, The University of Michigan.
- Sarli, V. D. and Benedetto, A. D. (2015), 'Modeling and simulation of soot combustion dynamics in a catalytic diesel particulate filter', *Chemical Engineering Science* **137**, 69 – 78.
- Swanson, J., Watts, W., Kittelson, D., Newman, R. and Ziebarth, R. (2013), 'Filtration efficiency and pressure drop of miniature diesel particulate filters', *Aerosol Science and Technology* **47**(4), 452–461.
- Takeda, K. and Koike, H. (1995), *Motor exhaust gas analyzer MEXA 7000 series*, 11 edn, Horiba.
URL: <http://www.horiba.com/uploads/media/R011-05-025-E.pdf>

- Tardos, G. I., Gutfinger, C. and Abuaf, N. (1976), 'High pecllet number mass transfer to a sphere in a fixed or fluidized bed', *AIChE Journal* **22**(6), 1147–1150.
- Tronconi, E. and Forzatti, P. (1992), 'Adequacy of lumped parameter models for scr reactors with monolith structure', *AIChE Journal* **38**(2), 201–210.
- Twigg, M. V. (2007), 'Progress and future challenges in controlling automotive exhaust gas emissions', *Applied Catalysis B: Environmental* **70**.
- UNEP (2009), 'Pollutants: Particulate matter', <http://www.unep.org/tnt-unep/toolkit/pollutants/facts.html>. Accessed: 2016-05-21.
- Van Setten, B. A. A. L., Makkee, M. and Moulijn, J. A. (2001), 'Science and technology of catalytic diesel particulate filters', *Catalysis Reviews* **43**(4), 489–564.
- Wang-Hansen, C., Kamp, C. J., Skoglundh, M., Andersson, B. and Carlsson, P.-A. (2011), 'Experimental method for kinetic studies of gas-solid reactions: Oxidation of carbonaceous matter', *The Journal of Physical Chemistry C* **115**(32), 16098–16108.

A

Appendix A

A.1 Thermocouples

Type K thermocouples are base metal thermocouples made of two wire legs of different metals: Nickel Chromium and Nickel aluminium contained in a protective sheath and joined at a junction. Temperature changes at the junction create a voltage signal which is then converted to local temperature via a temperature voltage conversion equation. The 0.5mm probe diameter thermocouples have a probe temperature range of -40 °C to 750 °C and the 1mm probe diameter type K thermocouples have a probe temperature range of -40 °C to 1100 °C (RS , 2013). The thermocouples are calibrated as described in the following. They are calibrated using both 0 °C and 100 °C from which temperature correction factors are obtained for all the thermocouples given in tables A.1 and A.2.

A.1.1 Zero degree calibration

1. Thermocouples that are to be calibrated are fastened together using a thin wire so that they all have their probe tips at the same point
2. An ice-water mixture at 0⁰C containing ice cubes mixed with room temperature water is then prepared
3. The fastened thermocouples are then inserted into the ice-water mixture for 30minutes.
4. Temperature readings predicted by the thermocouples are then collected and an averaged of the collected data is calculated.
5. The correction factor the thermocouples will then be given by:
Correction factor = Set temperature - Average predicted temperature

A.1.2 100 degree calibration

1. Thermocouples that are to be calibrated are fastened together using a thin wire so that they all have their probe tips at the same point
2. Hot water at 100 °C is then prepared
3. The fastened thermocouples are then inserted into the hot water for 30minutes.
4. Temperature readings predicted by the thermocouples are then collected and an averaged of the collected data is calculated.
5. The correction factor the thermocouples will then be given by:
Correction factor = Set temperature - Average temperature predicted by the thermocouple

Tc0	Tc1	Tc2	Tc3	Tc4	Tc5	Tc6	Tc7	Tc8	Tc10
-1.26	-0.62	-0.58	-0.27	-0.42	-0.23	-0.98	-1.12	-1.02	-0.98

Table A.1: Temperature correction factors for thermocouples for 0°C reading

Tc0	Tc1	Tc2	Tc3	Tc4	Tc5	Tc6	Tc7	Tc8	Tc10
1.7	0.07	0.2	0.05	0.24	0.27	2.43	2.14	2.25	2.22

Table A.2: Temperature correction factors for thermocouples for 100°C reading

A.2 Mass flow controllers

In order to measure and control the gas flow into the reactor set up, Bronkhorst High-Tech B.V.'s EL-FLOW type mass flow controllers of capacity: $20 L_n/\text{min}$ and $2000 mL_n/\text{min}$ connected in series are used.

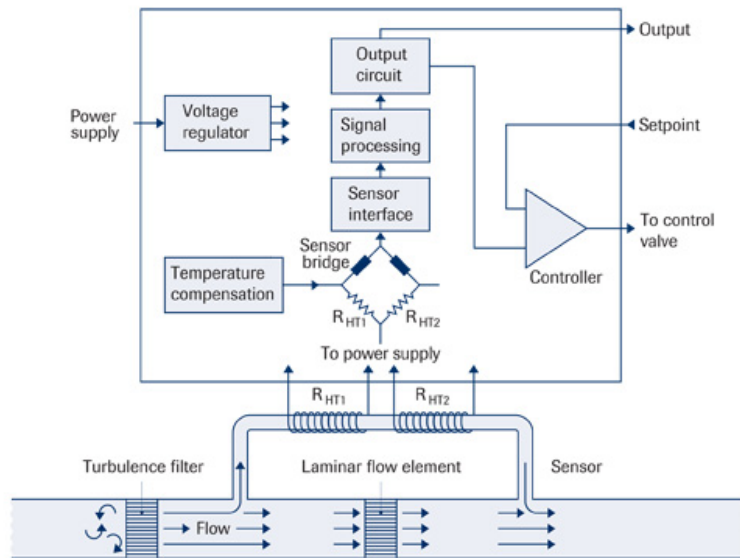


Figure A.1: Working principle Mass-flow controller (Bronkhorst, 2016)

The principle of operation used by these mass flow controllers is the by-pass measurement principle: part of the gas flow from the main stream is pushed by a laminar flow device into a capillary (see Figure A.1). This generates a pressure difference in the mass flow controller. Parts of the capillary are then heated inside the mass flow controller, as shown in Figure A.1, thereby creating a temperature difference between upstream and downstream of the capillary tube. The temperature difference is measured and depends upon the amount of heat taken up by the gas flow forced through it. The measured temperature difference is directly proportional to the mass flow, hence flow rates through the mass flow controller are then obtained by comparing flow conditions in the capillary tube to the flow conditions in the

laminar device. The measured signal from the mass flow controller is given in voltage and is connected to the mass flow and the heat capacity through Equation A.1 (Bronkhorst, 2010, 2016).

$$V_{signal} = K_{MFC}c_p\Phi_m \quad (\text{A.1})$$

V_{signal} is the measured voltage signal, K_{MFC} is a constant needed when other gases than the calibration gas is used, c_p is the heat capacity of the gas flow and Φ_m denotes the mass flow. The voltage signal measured is controlled via the temperature sensor whereby the flow through the laminar device from the capillary tube is varied until the right temperature difference that gives the desired voltage signal is got (Bronkhorst, 2010, 2016). The mass flow controllers are operated via Lab-view. Here a desired flow rate is set in Lab-view, this is then converted to a voltage signal sensed by the mass flow controllers while in return the actual output voltage reading from the mass flow controllers is sent to Lab-view where it is converted to the actual flow rate reading. The mass flow controllers are calibrated in order to ensure their accuracy. The 20 L_n/min capacity mass flow controller is calibrated on air at 5 bar, 20.25 °C pressure inlet and atmospheric pressure at the outlet. The 2000 mL_n/min capacity mass flow controller is also calibrated on air at 5 bar pressure inlet and atmospheric pressure at the outlet but at a temperature of 23.8 °C. In case a gas other than air is to be used on the mass flow controllers, a conversion factor has to be used in order to account for the varying specific heat and density of the gas with respect to the specific heat and density of air used to calibrate to the mass flow controllers. This is done so as to correct the output voltage signal from the mass flow controllers. The conversion factor C_{MFC} is given by:

$$C_{MFC} = c_{p1}\rho_1/c_{p2}\rho_2 \quad (\text{A.2})$$

Where c_p is the specific heat and ρ is the density at normal conditions while subscripts 1 and 2 represent gas calibrated and gas to be measured respectively. The calibration done on the mass flow controllers was to be used on gas flow specifications of 96% N_2 and 4% NH_3 which correspond to a conversion factor of 1.011. A flow mixture for Air/ N_2 mixture at 20 °C and 1 atm corresponds to a conversion factor of 1.

A.3 CO₂/CO gas analyzers

A Horiba infrared gas analyzer is used to measure and quantify the amount of CO₂ and CO released at the reactor outlet. This gas analyzer works at a gas flow rate of 1 L_n/min and temperature. Therefore the gas to be analyzed must be fed to the analyzer at these specified conditions. Infrared gas analyzer is an optical analyzer that utilizes optical absorption technique to measure the amount of CO₂ and CO present in the gas stream. It is equipped with a light source at the reference cell that produces infrared energy. The infrared energy is converted to intermittent light which passes through measurement cells before reaching the detector. Part of the intermittent light is absorbed by sample gas present in the sample cell. The amount of light absorbed is proportional to the amount of CO₂ and/or CO present in the gas

stream. The amount of CO₂ and CO present in the gas stream is then detected at the detector which detects the absorption of infrared energy of wavelength specific to the component measured (Takeda and Koike, 1995). Output signal from the detector is in voltage and this is sent to Lab-view where it is converted to ppm reading. In order to ensure accuracy of the CO₂/CO gas analyzers, the analyzers are calibrated before any experimental run as described below.

A.3.1 Calibration procedure CO/CO₂ analyzer

1. Make sure the NO/NO₂ analyzer including ozone destroyer and bypass pump is on and is ready to measure (MEAS), since the bypass pump draws the sample for both analyzers.
2. Connect N₂ to the T-junction where the sample is drawn and connect N₂ in the storage room to the N₂ bottle (line 3).
3. Check the flow rate on the excess gas MFC and adjust the pressure coming from the flask to give the working excess flow rate (in this case roughly 1 l/min excess).
4. Turn off the “REMOTE” on the instrument.
5. Select the ranges for CO and CO₂ that you will work on.
 - (a) Change the range with the up and down buttons
 - (b) This case: 3000 ppm for CO(L), using 2000 ppm calibration gas
 - (c) This case: 3% for CO₂, using 2.7% calibration gas
6. In menu ”DET SELECT” press the buttons “CO.L”, “CO.H” and “CO2” to select all detectors.
7. In menu “MODE” press “ZERO” and then “CAL”. This calibrates all channels to be zero when there is only inert gas.
8. Note down the voltage shown by Labview or record with Labview to know the zero voltage.
9. Deselect “CAL” and “ZERO”.
10. Turn off the gas bottle of N₂ with the wheel on the flask and disconnect the pipe from the T-junction.
11. Connect the CO pipe (line 1) to the T-junction and connect the line to the gas bottle (2000 ppm CO) and adjust the excess flow rate as before.
12. Deselect “CO.H” and “CO2” and check the measuring range again (unless you are calibrating with a higher ppm, then it might be “CO.H” instead that you need to keep).
13. In menu “SPAN SET” press “DISP” to show the current value set for CO(L). It should be the same as the concentration that you are calibrating with (2000 ppm in this case). If it is not, correct the value using “DIGIT” and press “SET” when you have the correct value.
14. In the “MODE” menu, press “SPAN” and “CAL” to calibrate the signal and check that the displayed signal is the ppm of the calibration gas that you are using. Also note or record the value on Labview, taking at least 10 measurements into account.
 - (a) TIPP: The maximum voltage is always 10 V and corresponds to the upper limit of your chosen range, whereas 0 V corresponds to 0 ppm.

In this case, 10 V correspond to 3000 ppm. The displayed value should approximately be the ratio of bottle value to maximum range value, so $2000/3000 = 2/3 \rightarrow 2/3 * 10 \text{ V} = 6.66 \text{ V}$.

15. Deselect “CAL” and “SPAN”, turn off the CO bottle and disconnect the CO pipe from the T-junction.
 16. Repeat for CO₂ from step 11 on.
- (Horiba, 1999)

B

Appendix B

B.1 Experimental set-up description

To begin with, the set-up at the outlet is assembled as shown in Figure B.1. Five 0.5 mm 'type K' thermocouples are then inserted through the thermocouple entrance at the outlet (Figure B.2). The thermocouples are pushed through a series of junctions leading from the air inlet and through the pressure measurement junction. The junctions at these points are then fastened to ensure that the set-up is air tight at these points. The thermocouples are pushed through another junction and then inserted through a 6 mm inner diameter measurement pipe leading to the reactor outlet. At this point the thermocouples are inserted through the holder at the reactor outlet and the holder connections at the holder are fastened. The thermocouples are adjusted in length in accordance with the thermocouple placement pattern presented in Figures B.3 and B.4 before they are inserted into the ceramic substrate. A pair of thermocouples is placed at the inlet and one at the outlet. The thermocouples of each pair are placed at the same axial points, but different radial points in order to measure the radial temperature differences. Another thermocouple is placed in the middle of the substrate. In this way, axial temperature differences in the substrate are measured. The adjusted thermocouples are fastened together at the thermocouple entrance using silicon and tape (Figure B.8). They are then inserted through the reactor substrate (Figure B.6).

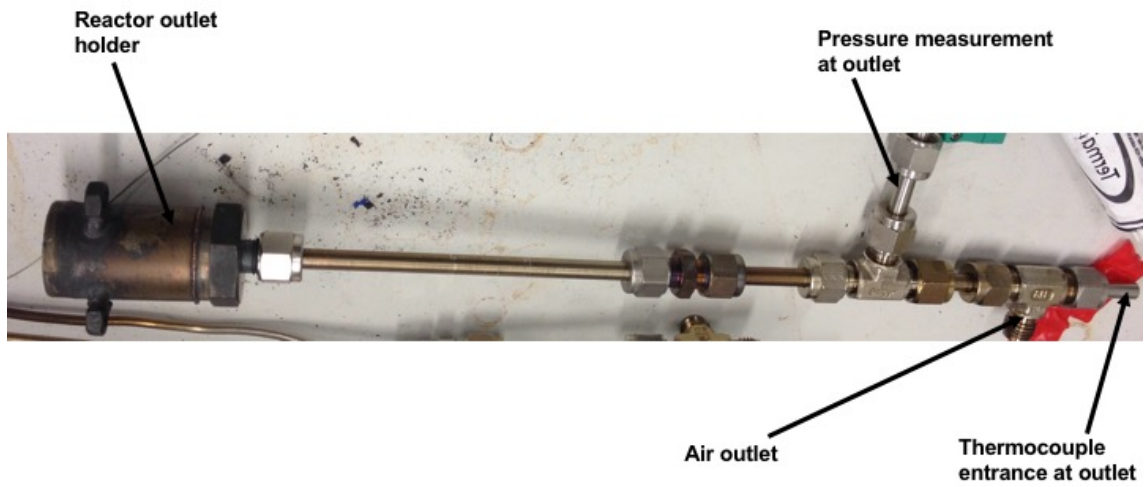


Figure B.1: Assembling of the experimental set-up at the inlet

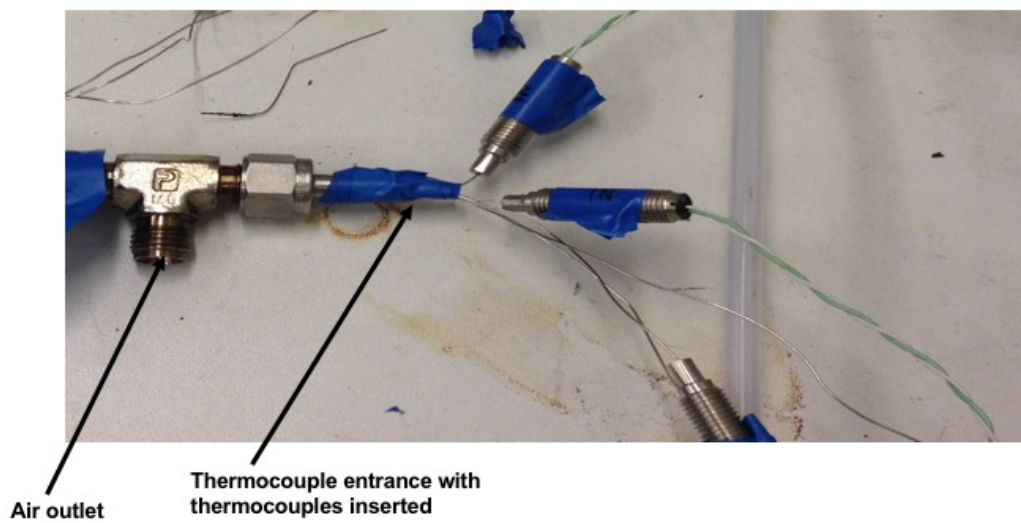


Figure B.2: Thermocouple inserted and fastened at the the thermocouple entrance.

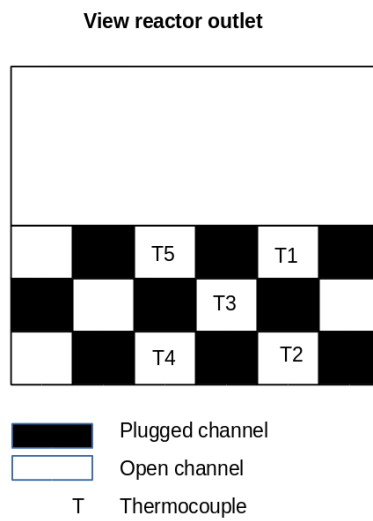


Figure B.3: Thermocouple placement in the substrate outlet

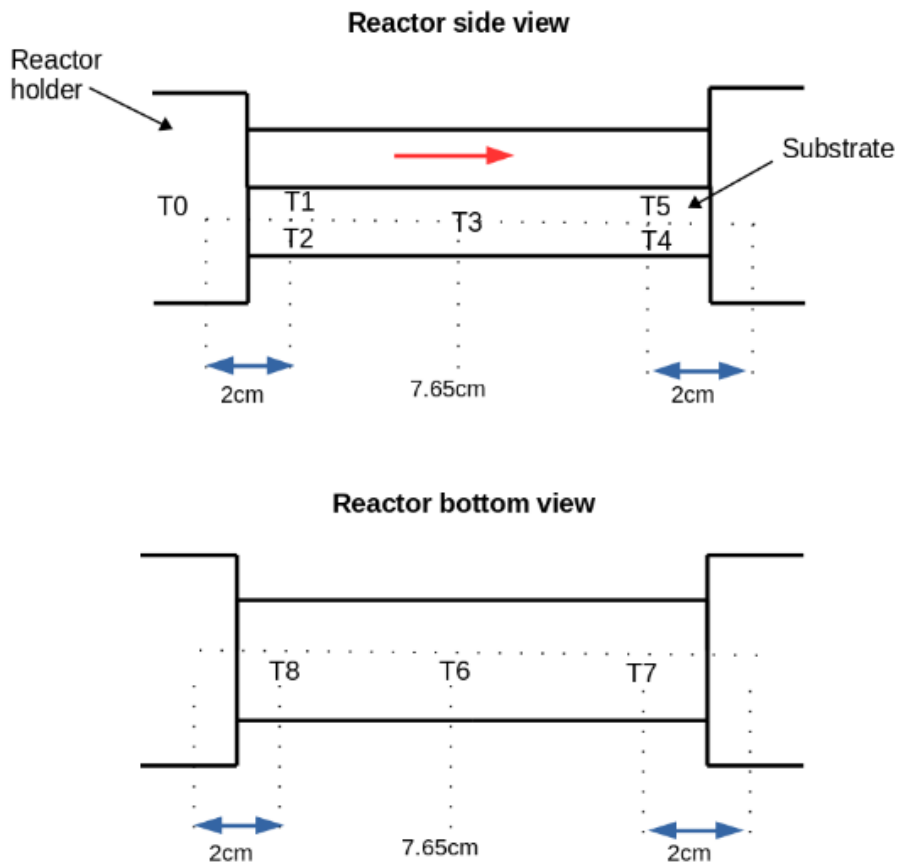


Figure B.4: Thermocouple placement view from side and bottom of the reactor. The red arrow indicates the flow direction.

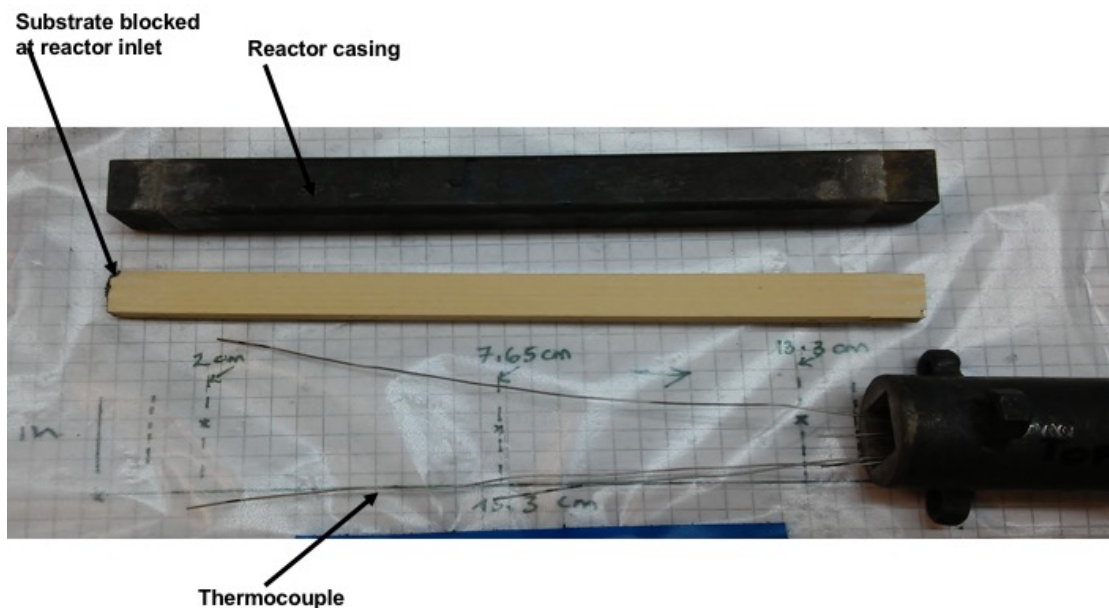


Figure B.5: Thermocouple in the reactor outlet holder adjusted to different lengths.

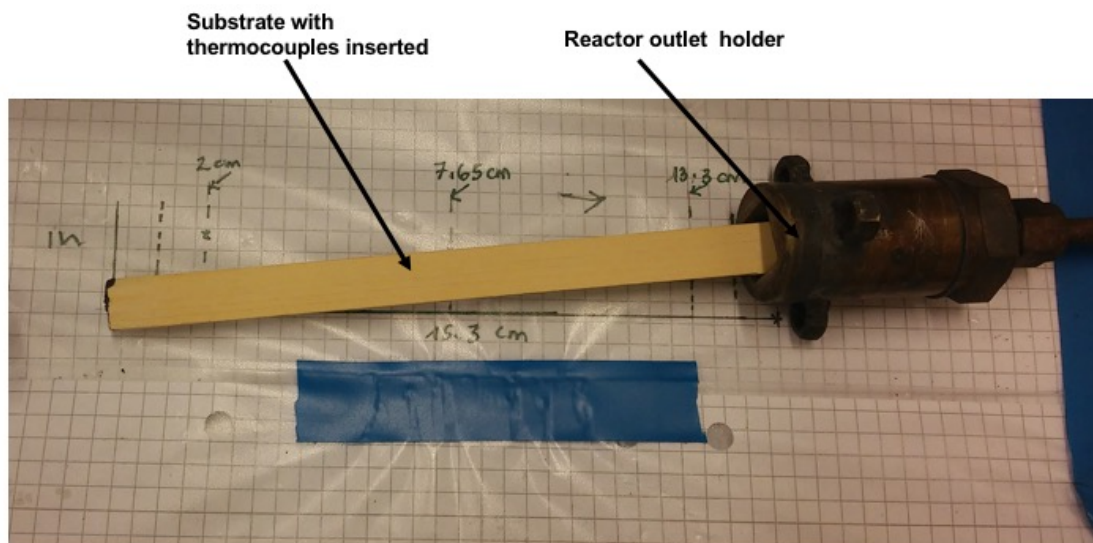


Figure B.6: Reactor substrate inserted into the reactor outlet holder.

The reactor casing is glued with ceramic glue at the edges that are to be inserted into the reactor outlet holder. The substrate with thermocouples inside is then inserted into the reactor casing which is then attached to the the reactor outlet holder (Figure B.7).

The reactor is then attached to the reactor holder at the inlet. Three 6 inch screws are then used to hold the reactor set up in place. The reactor set up is then glued

using ceramic glue at the outside where the the reactor is attached to the holders in order to make the set up air tight at these points (Figure B.9). Three 1mm thermocouples are then attached to the reactor bottom at axial positions as presented in Figure B.3. This is done in order to determine the temperature profile at the wall of the reactor and also to determine how efficient heat is transferred from the reactor oven through the reactor wall to the reactor substrate. The thermocouple connectors at the outlet are then fastened to a metal plate that holds them in place and ensures minimal bending of the thermocouples.

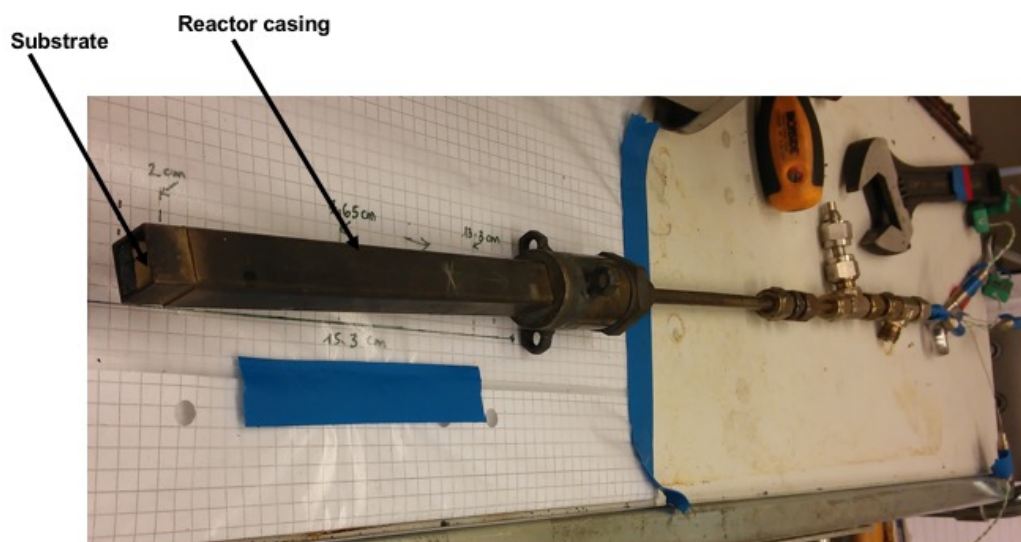


Figure B.7: Reactor substrate inserted into the reactor casing

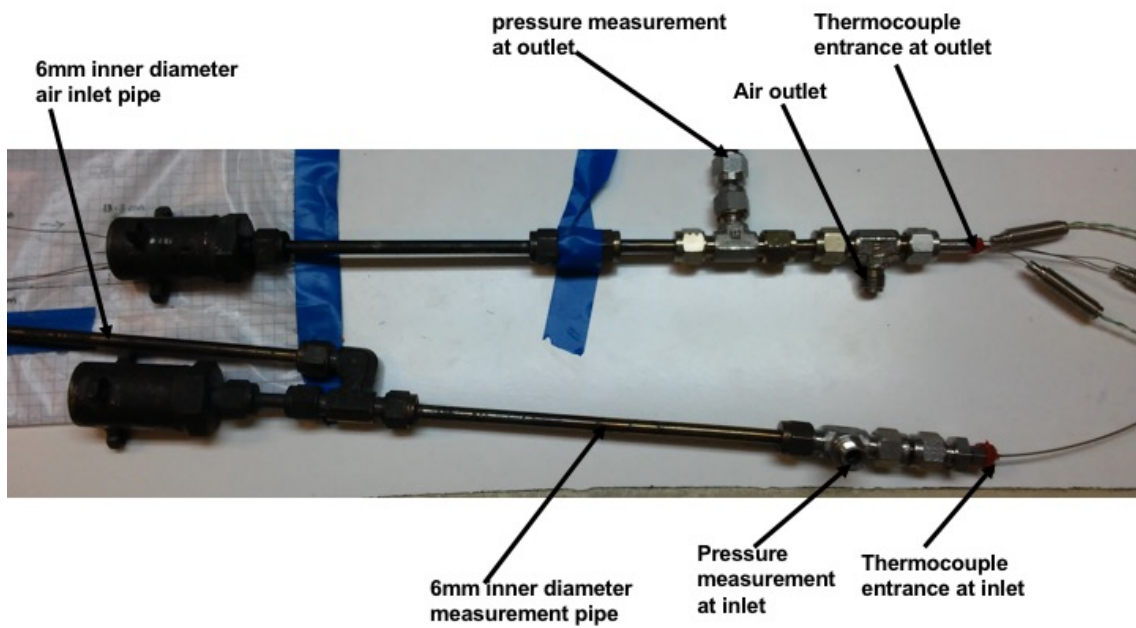


Figure B.8: Thermocouple entrance at the outlet(top) and inlet(bottom)

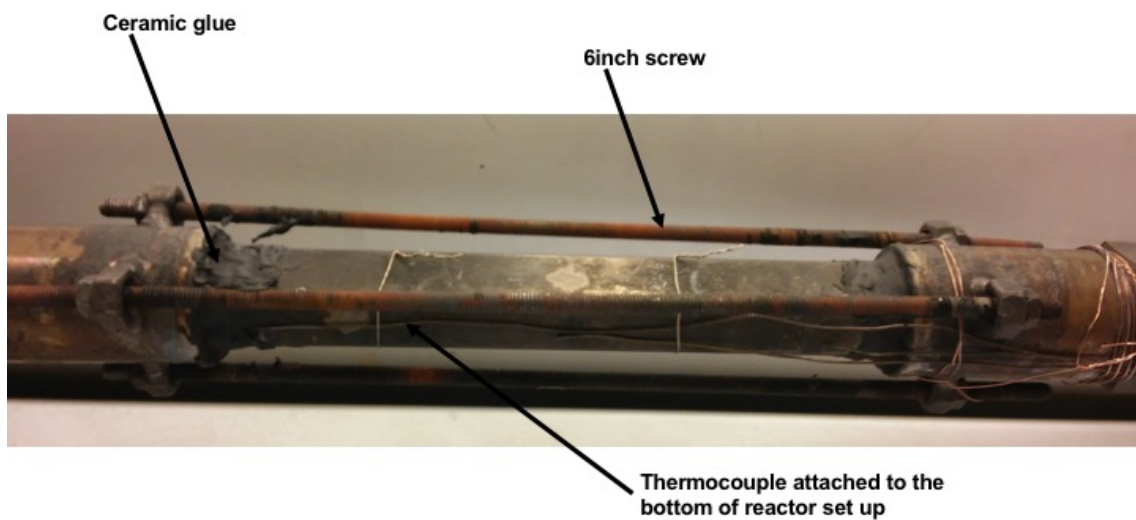


Figure B.9: Reactor set up fastened and glued to the reactor holders with reactor surface thermocouples attached

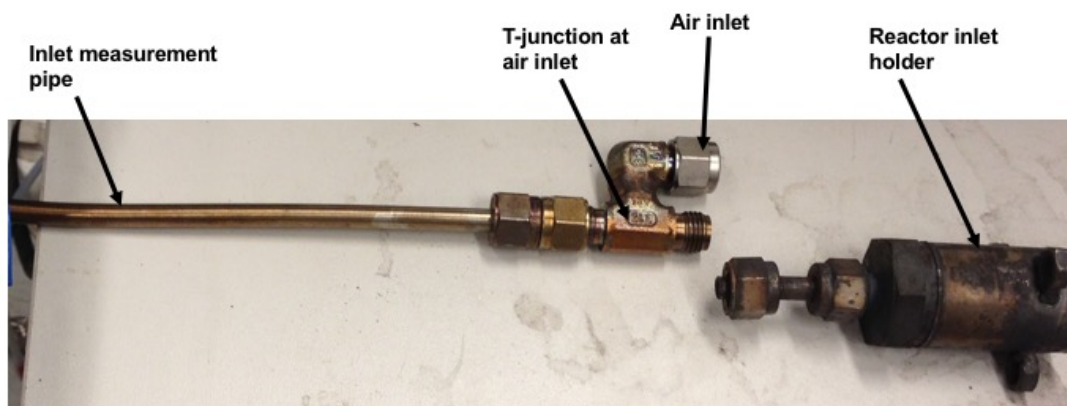


Figure B.10: Reactor set up at the inlet

The reactor set up at the inlet is assembled as shown in Figure B.10. Here a 6 mm inner diameter measurement pipe is attached to a t-junction which provides three way connection to a 6mm inner diameter air inlet pipe, a measurement pipe and connection to the reactor set up.

A 1mm 'type k' thermocouple is then inserted through the 6mm measurement pipe and through the t-junction (see Figure B.3). This is then fastened with silicon and tape at the point where it enters the 6 mm measurement pipe. This is used to measure the inlet air temperature at the reactor inlet. Another 1 mm 'type k' thermocouple is attached on the outside of the t-junction (see Figure B.3). This is then fastened with wires and the connectors of both thermocouples at the inlet are then held in secured on a metal plate that holds them in place and ensures minimal bending and thus damage to the thermocouples (Figures B.11 and B.12).

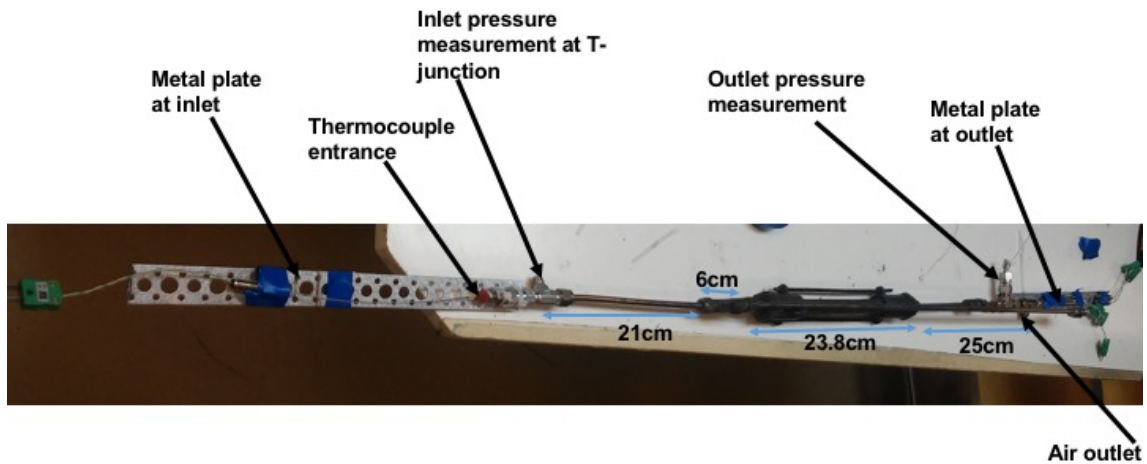


Figure B.11: Reactor set up with all thermocouples attached

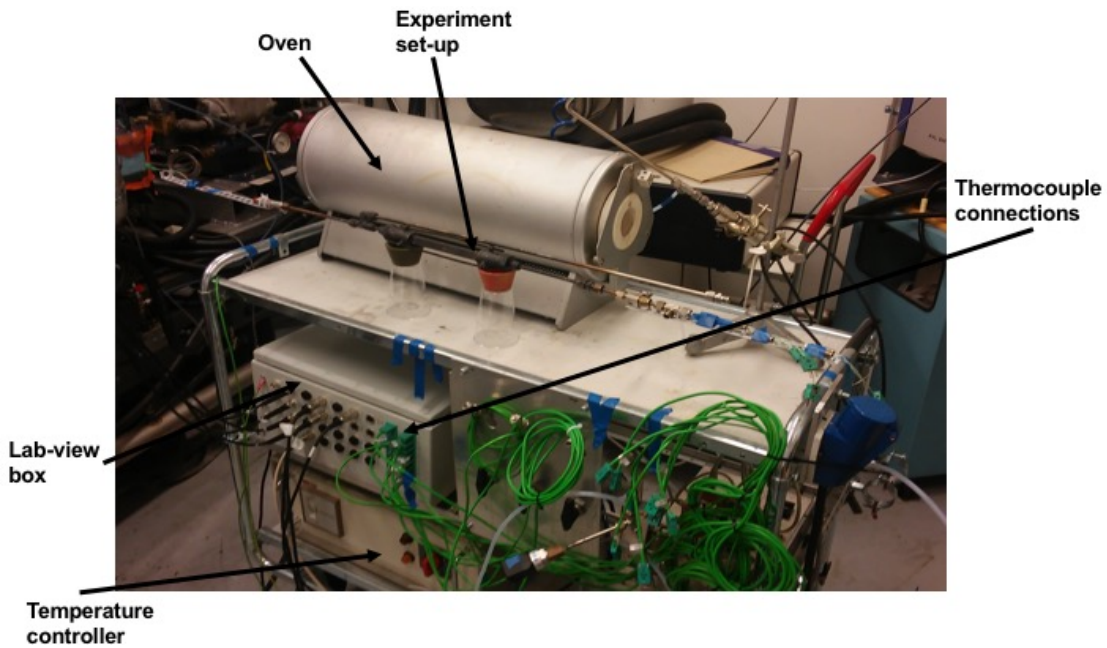


Figure B.12: Reactor set up with all thermocouples attached including view of oven and Lab-view box

Before the experimental set up shown in Figures B.11 and B.12 is inserted into the oven, it is insulated using glass wool at the points corresponding to oven outlet and inlet (Figure B.13). At the oven outlet, glass wool is attached between reactor outlet holder and the pressure measurement junction. While at the point corresponding to the oven inlet, glass wool is attached between air inlet junction and the pressure measurement junction at the inlet. The glass wool is fastened at these positions

using some wires.

The insulated reactor set up is then put in the oven. Before carrying out the experiment, the air inlet is connected to the mass flow controllers through a Teflon pipe that carries the air or gas mixture to be used at the inlet. The air or gas mixture is first heated up due to passing the oven through the inlet pipe before it enters the reactor at the reactor inlet. The flow rate to the reactor is controlled via mass flow controllers connected to Lab-view as described in Section A.2. The outlet of the reactor is connected to the gas analyzer rig through a Teflon pipe that runs from the reactor outlet to the t-junction connection at the gas analyzer rig. At this t-junction, part of the outlet gas is pumped to the CO₂/CO gas analyzer while the rest (excess gas) is sent to ventilation. Pressure sensors measuring pressure drop across the reactor are then connected at the inlet (ap2-AI1-skydd) and outlet (ap4-M3-A10-gas) of the reactor set-up. The different thermocouples used in the reactor set up are connected to Lab-view through thermocouple connectors connected to the Lab-view box. Figure B.14 summarizes the experimental set-up used. The experiment set-up is then ready to use. Modifications are however needed depending on the type of experiment that is to be conducted i.e. either flow or soot oxidation.

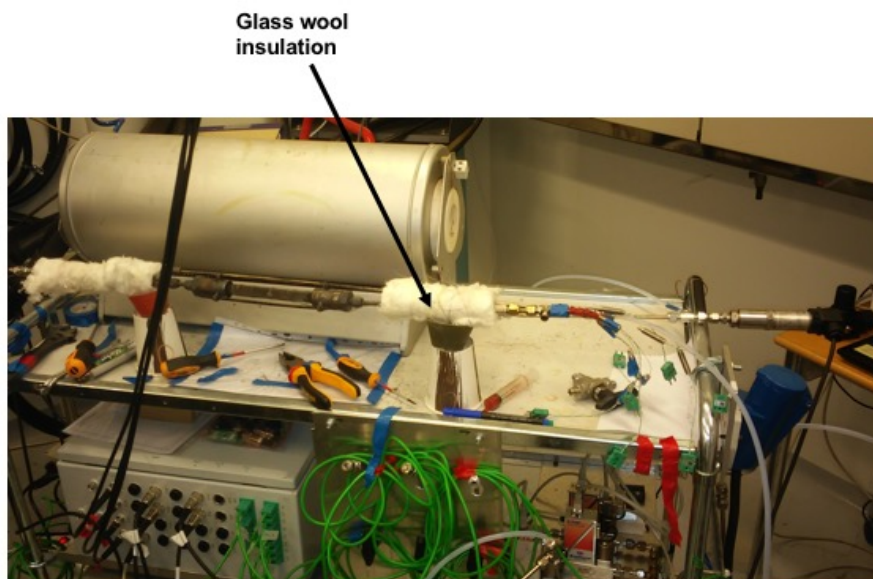


Figure B.13: Insulated reactor set-up

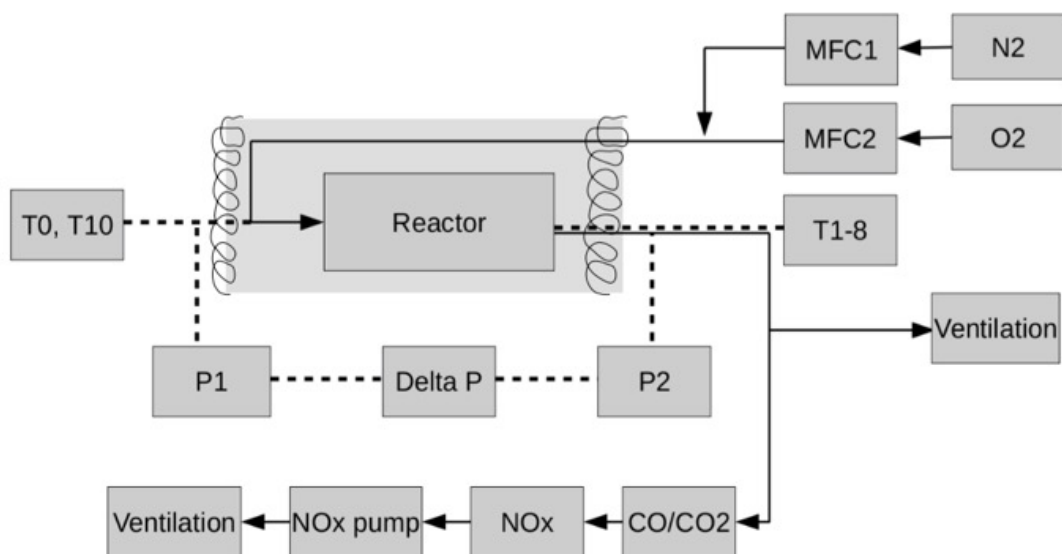


Figure B.14: Flow diagram showing the experiment set-up used

C

Appendix C

C.1 Result from the flow experiments

Conditions: 2 L/min , pressurized air at 4 bar, no soot

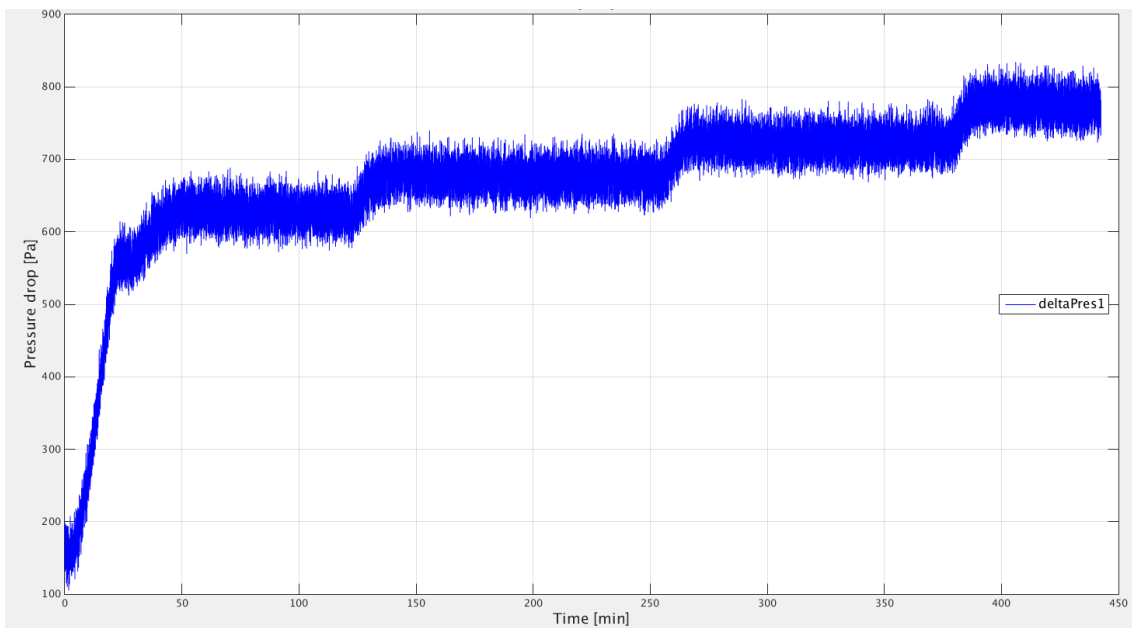


Figure C.1: Pressure drop flow experiment

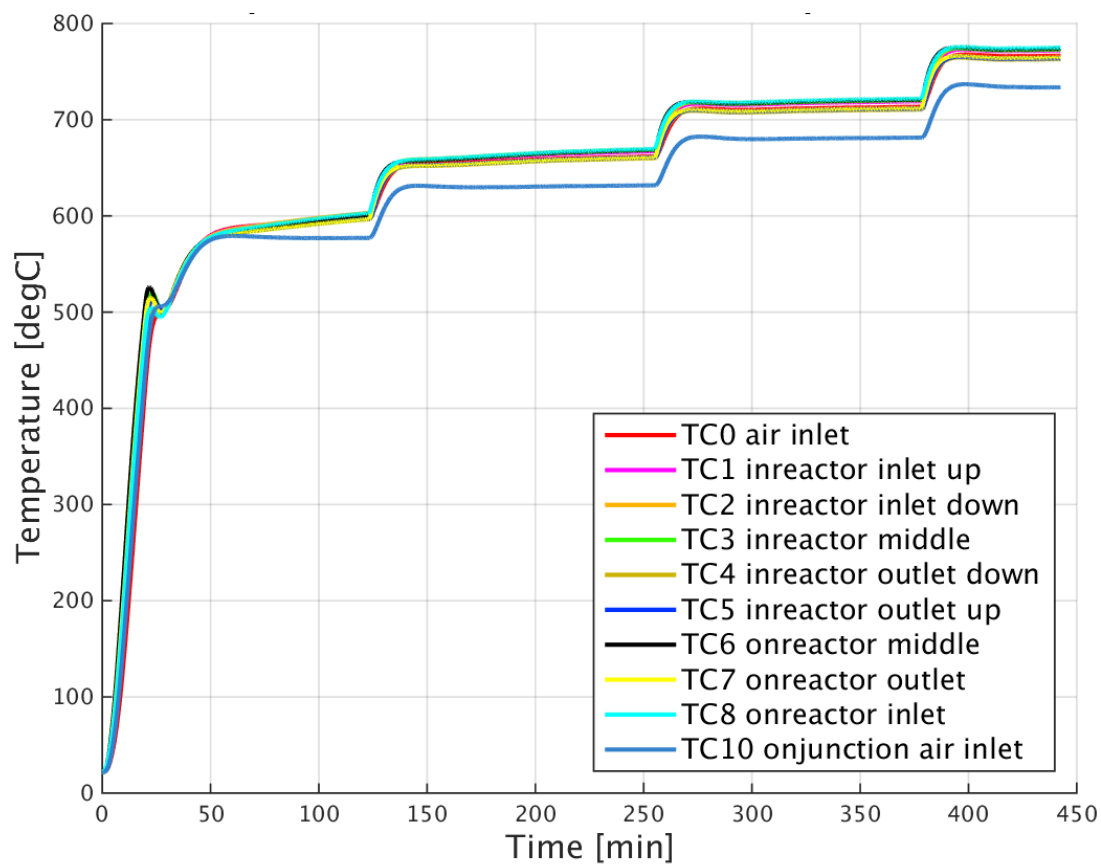


Figure C.2: Temperature flow experiment

Temperature overview (Element K) exp 20160413

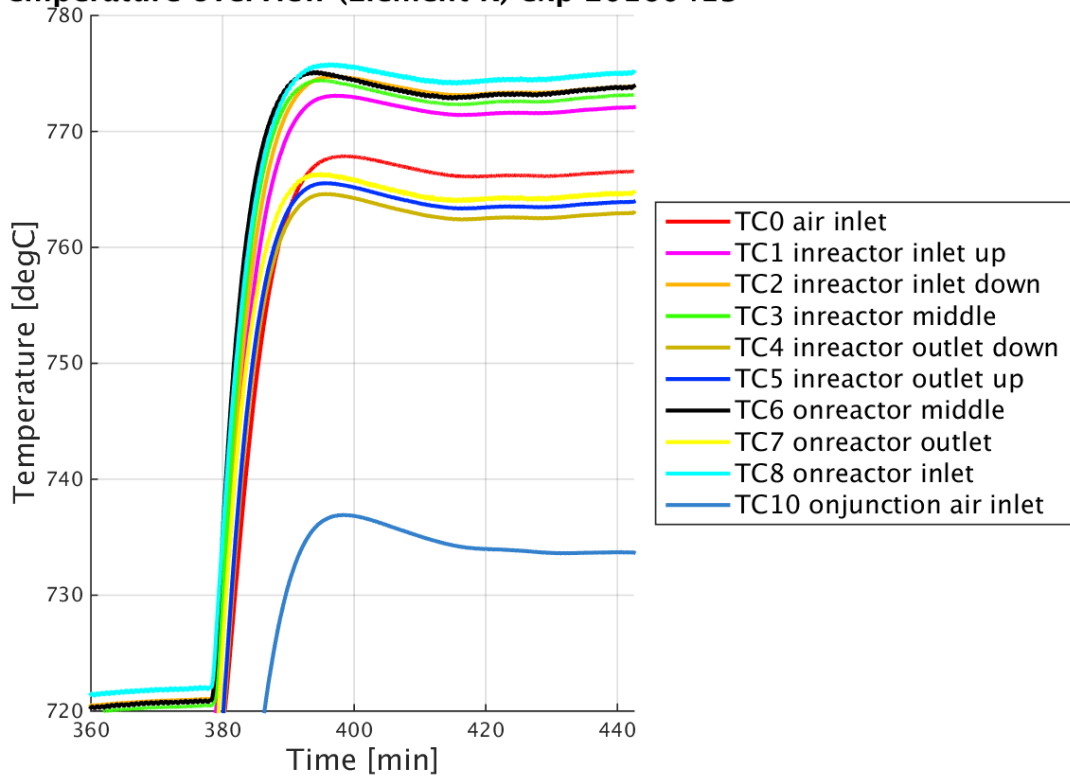


Figure C.3: Zoomed temperatures for flow experiment, showing radial and axial differences

D

Appendix D

D.1 Calculation for mass of soot used

In order to calculate mass of soot that will be applied on the surface of the substrate, the amount of soot loading per filter reported by both Sarli and Benedetto (2015) and Chen et al. (2009) of $10 \text{ kg}/\text{m}^3$ per filter which corresponds to $200 \text{ kg}/\text{m}^3$ soot loading in cake in the Sarli and Benedetto (2015) case is used. In this case, one filter corresponds to two substrate channels with one on top of the other as shown in figure D.1. Only the filters at the top surface of the substrate are considered in calculating the amount of soot that makes a cake on the surface of the substrate.

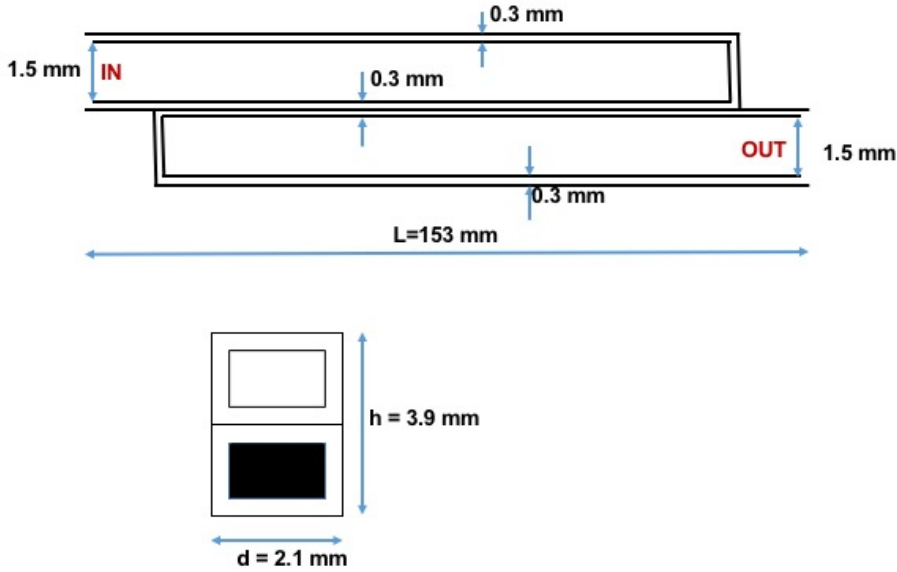


Figure D.1: Side view of one filter showing inlet/outlet channels (top), back view of inlet/outlet channels (bottom)

Volume of one filter for open flow case

$$V_{filter} = (2.1 \times 3.9 \times 153) \text{mm}^3 = 1.2531 \times 10^{-6} \text{m}^3 \quad (\text{D.1})$$

Soot mass in one filter

$$m_{soot,filter} = 10 \text{kg}/\text{m}^3 \times 1.2531 \times 10^{-6} \text{m}^3 = 12.531 \text{mg} \quad (\text{D.2})$$

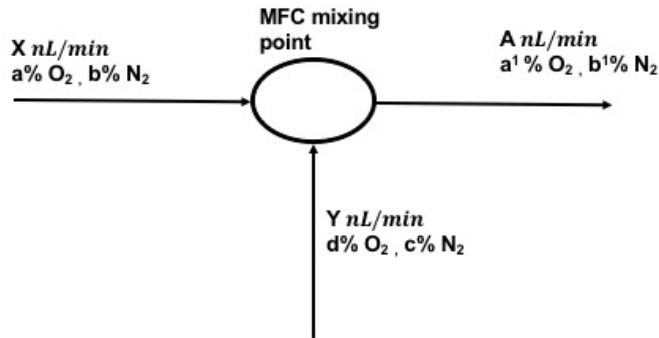
Total amount of soot

$$m_{soot,total} = 12.531mg \times 6 = 75.186mg \quad (D.3)$$

E

Appendix E

E.1 Calculation for gas mixture flow rate



Let X represent the flow rate of air, Y represent the flow rate of Pure Nitrogen and A represent the low rate of the air /N₂ gas mixture after coming out of the mass flow controller.

Let a and b represent the composition in volume percent of O₂ and N₂ respectively in air .

Let c and d represent the composition in volume percent of O₂ and N₂ respectively in pure Nitrogen.

Let a^1 and b^1 represent the composition in volume percent of O₂ and N₂ respectively in the air /N₂ gas mixture.

From mass balance of oxygen:

$$a \times X + d \times Y = a^1 \times A \quad (\text{E.1})$$

$$X = (a^1 \times A - d \times Y)/a \quad (\text{E.2})$$

$$d = 0 \tag{E.3}$$

$$A = 2000L_n/min \tag{E.4}$$

$$Y = A - X \tag{E.5}$$

F

Appendix F

F.1 Results from the DPF experiment

The temperature profile shown in Figure F.1 is obtained, using 2.5 mol% oxygen, 2 L/min and 650 °C. At 12 minutes, a higher oxygen concentration is used in order to see whether and where soot is left that has not yet been oxidized. It can be seen that a very high temperature peak occurs in the middle of the substrate, which is composed of three minor peaks. Also the peak in the outlet exhibits a divided peak. The temperature in the inlet exhibits just one peak. The divided peaks could be due to a temperature front moving in the reactor.

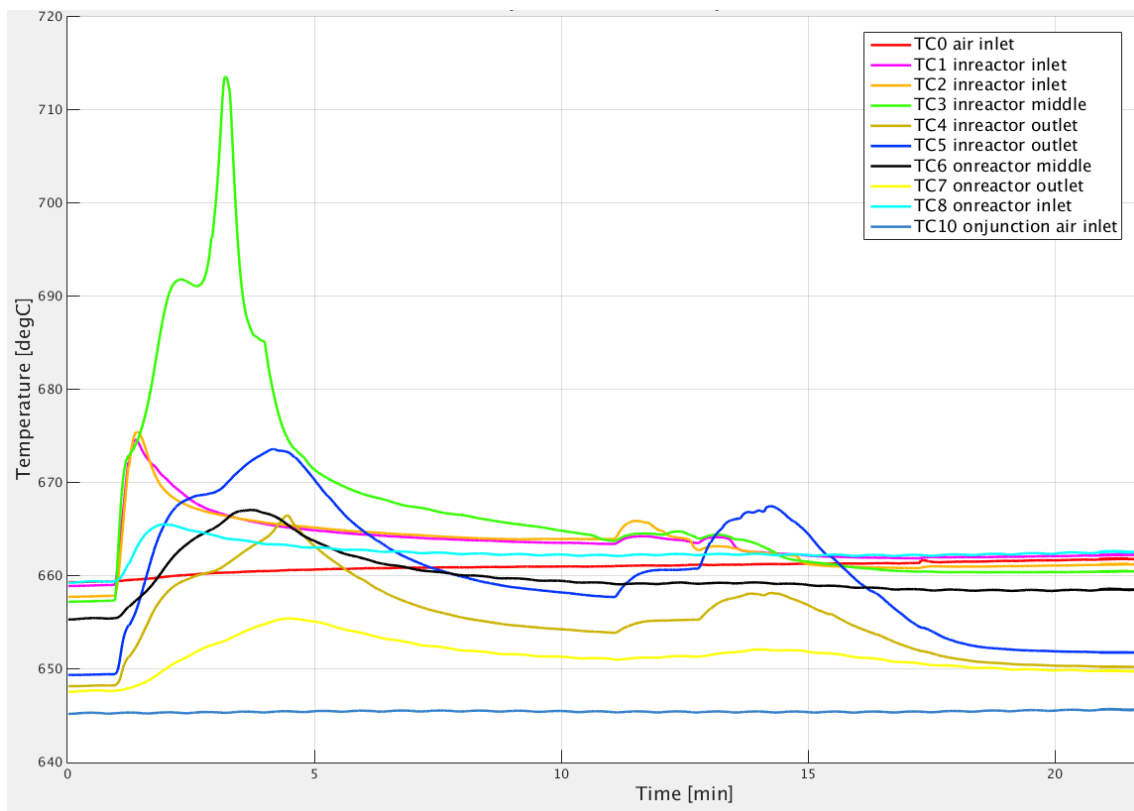


Figure F.1: Temperature plots for thermocouples in a DPF substrate

The pressure sensor readings are not reliable when it comes to the values in this experiment, since a problem occurred and could not be fixed. However, the trend is also observed from the two absolute pressure readings before and after the reactor;

hence, it is concluded that the trend is correct. It is in accordance with expectations: The soot layer causes the pressure drop to be high and as it is consumed, the pressure drop decreases. This is also in accordance with results reported by Konstandopoulos and Papaioannou (2008).

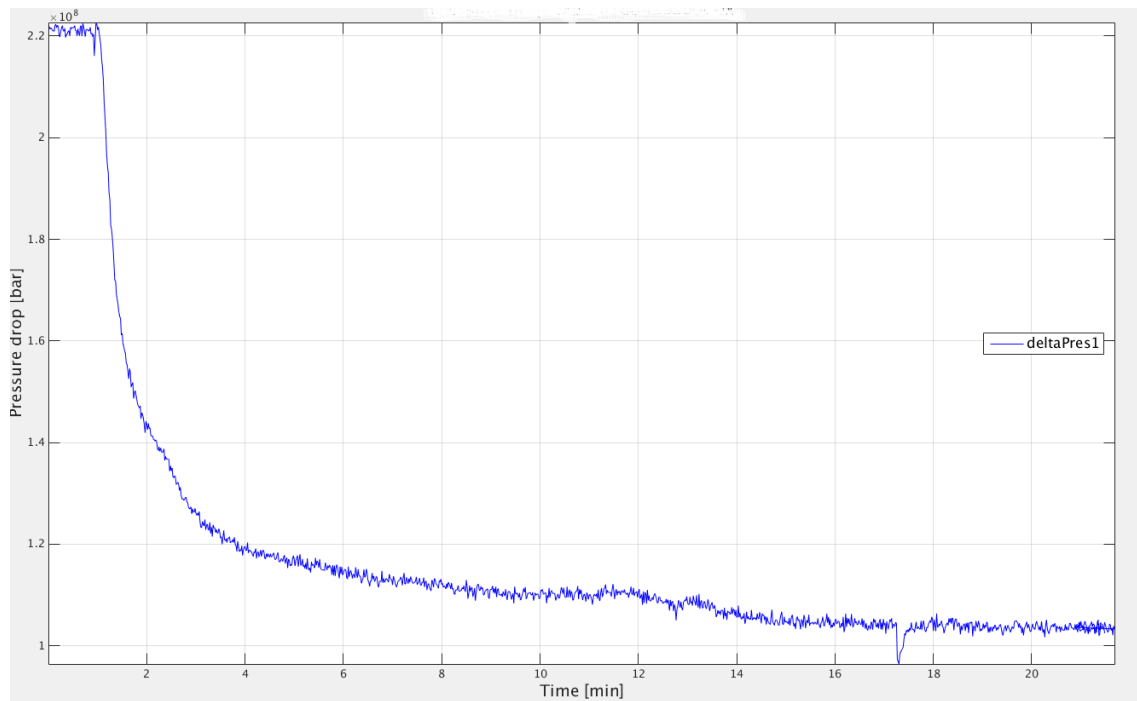


Figure F.2: Pressure drop in a DPF substrate. The sensor was broken so that the reading is erroneous for this experiment. However it can be seen as a qualitative result.

G

Appendix G

G.1 Gas mixture thermal conductivity

$$k(T) = 3.919 \times 10^{-4} + 9.816 \times 10^{-5}T - 5.067 \times 10^{-8}T^2 + 1.504 \times 10^{-11}T^3 \quad (\text{G.1})$$

G.2 Gas mixture viscosity

$$\mu(T) = 0.7632 \times 10^{-6}T^{0.58823} \frac{1}{1 + \frac{67.75}{T}} \quad (\text{G.2})$$

H

Appendix H

H.1 Additional graphs soot experiment 1

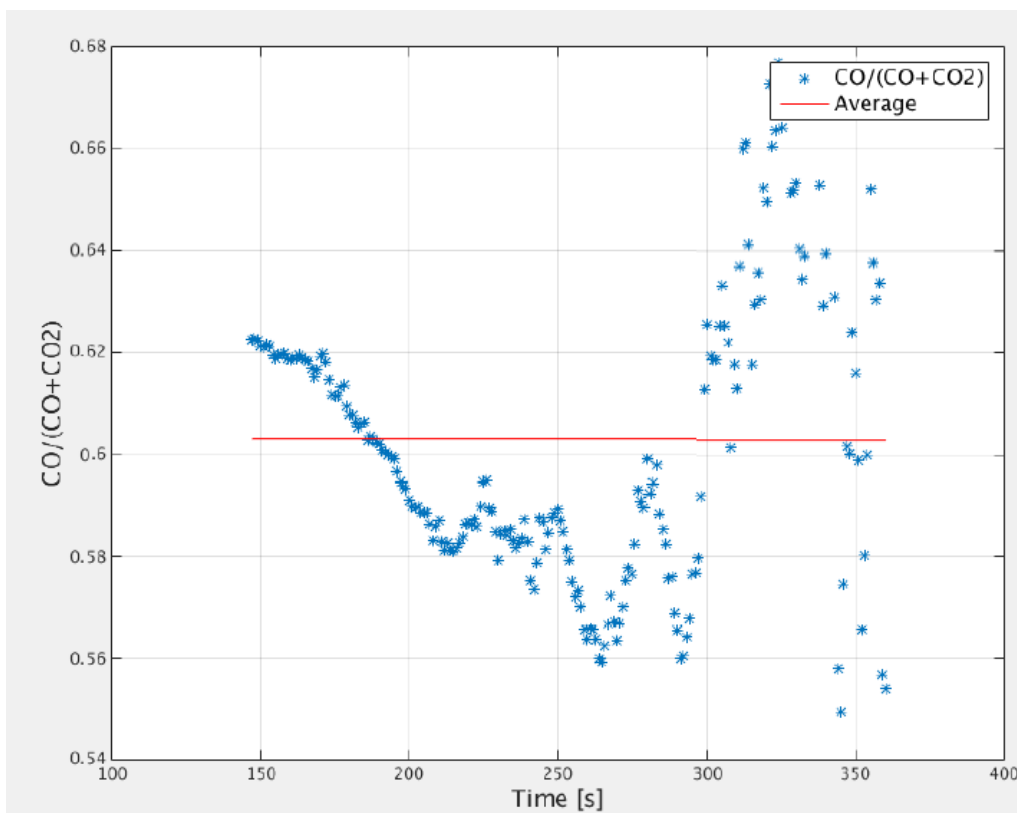


Figure H.2: Ratio $CO/(CO+CO_2)$ taken between 147 and 360 seconds during soot oxidation and average.

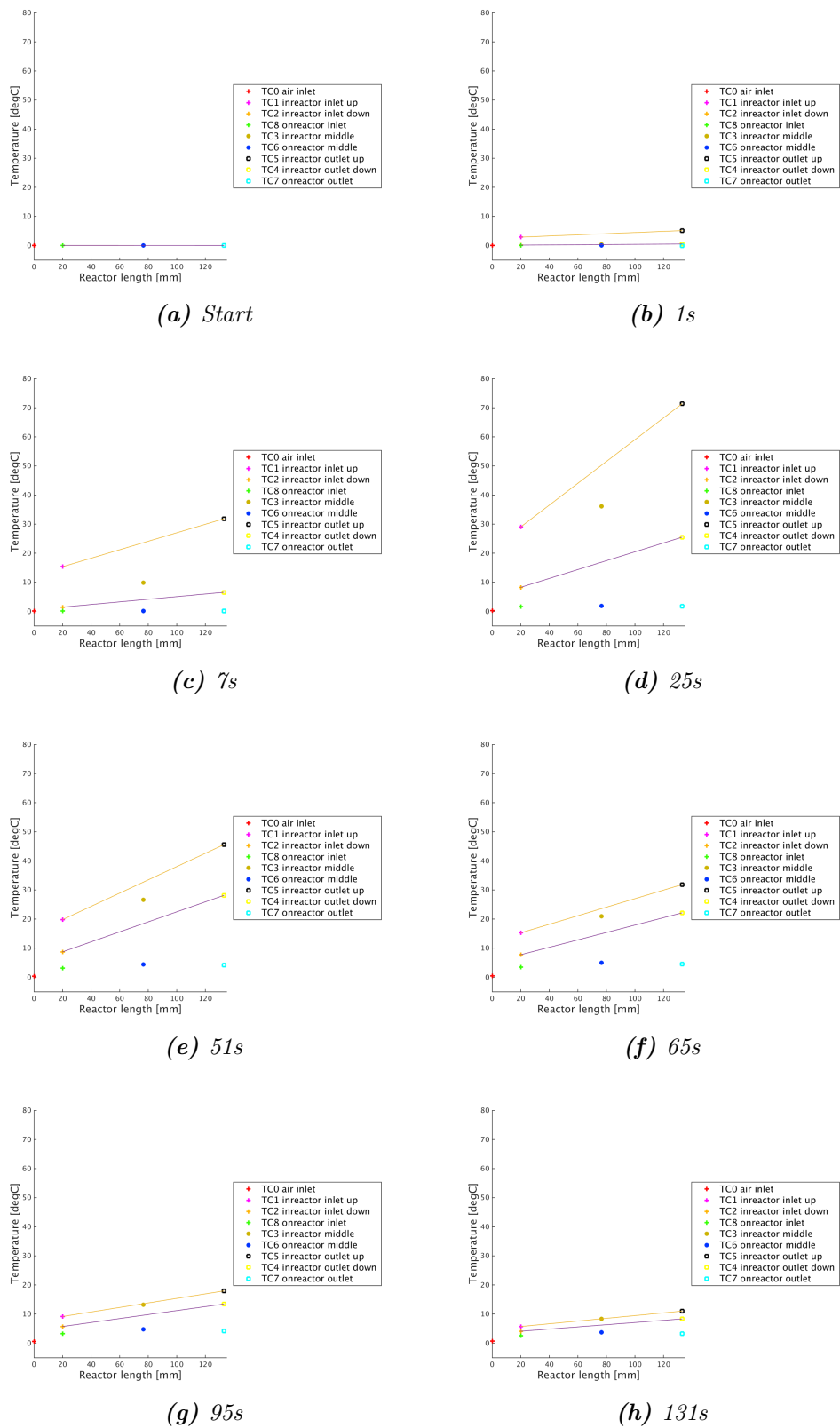


Figure H.1: Development of the axial temperature profile during the thermal front

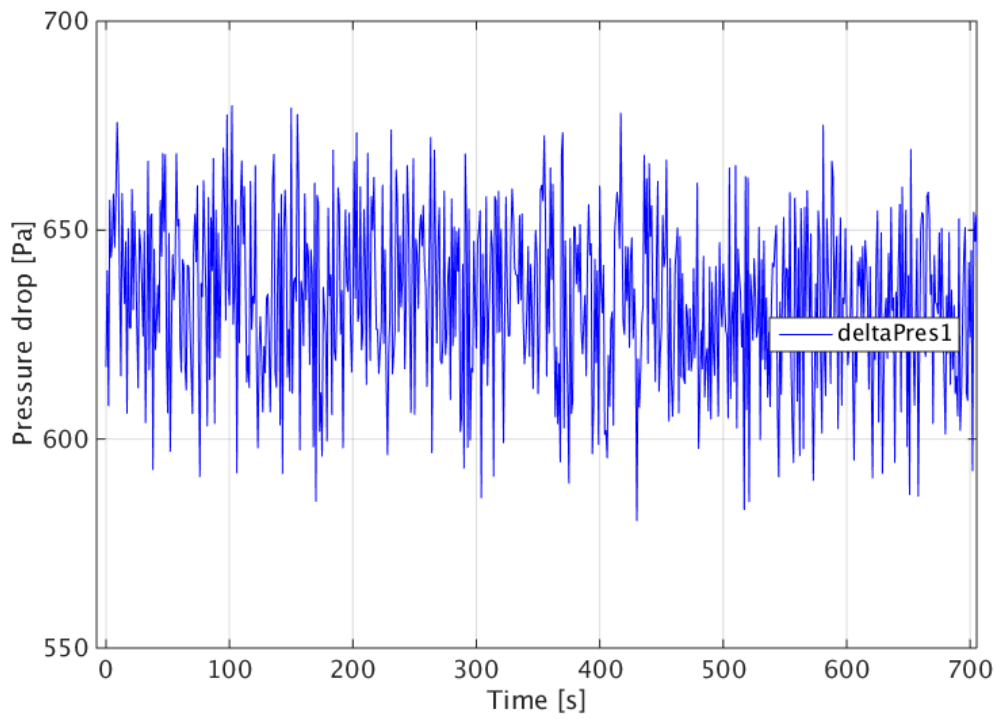


Figure H.3: Pressure drop measured during soot oxidation (plot starts after the correct synthetic air concentration is reached, before the pressure drop is constant around 615 Pa).

I

Appendix I

I.1 Resulting plots from experiment 3

Conditions: 73.9 mg soot, 650 °C, 2 L/min, 15% O₂

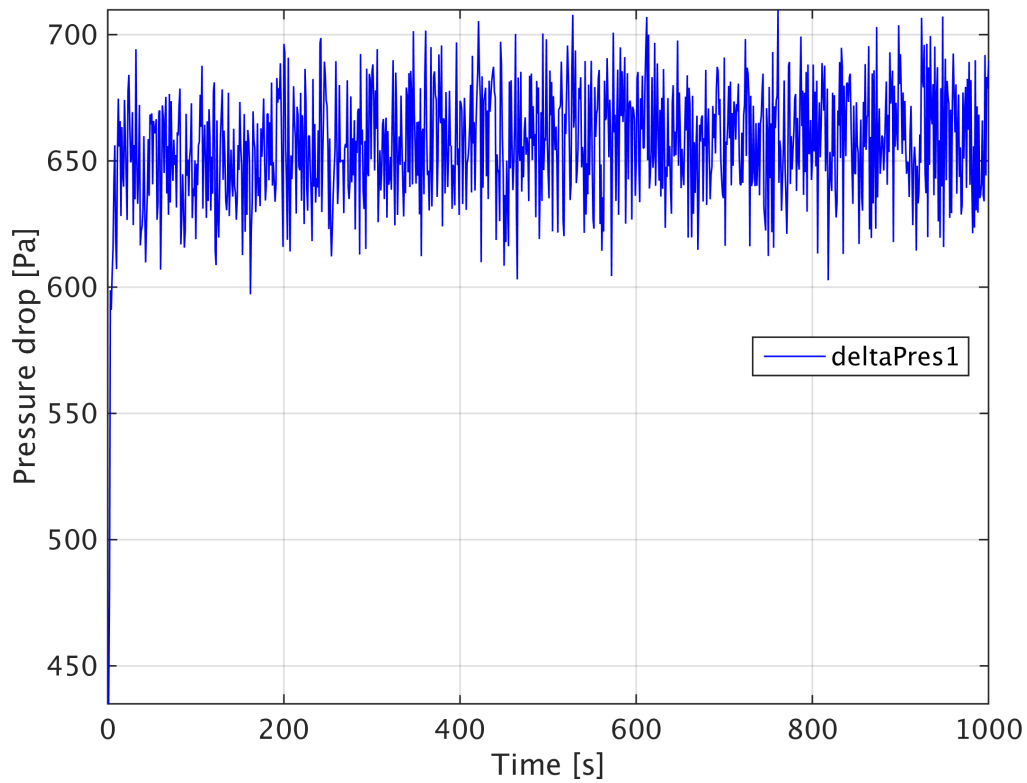


Figure I.1: Pressure drop during soot oxidation in experiment 3

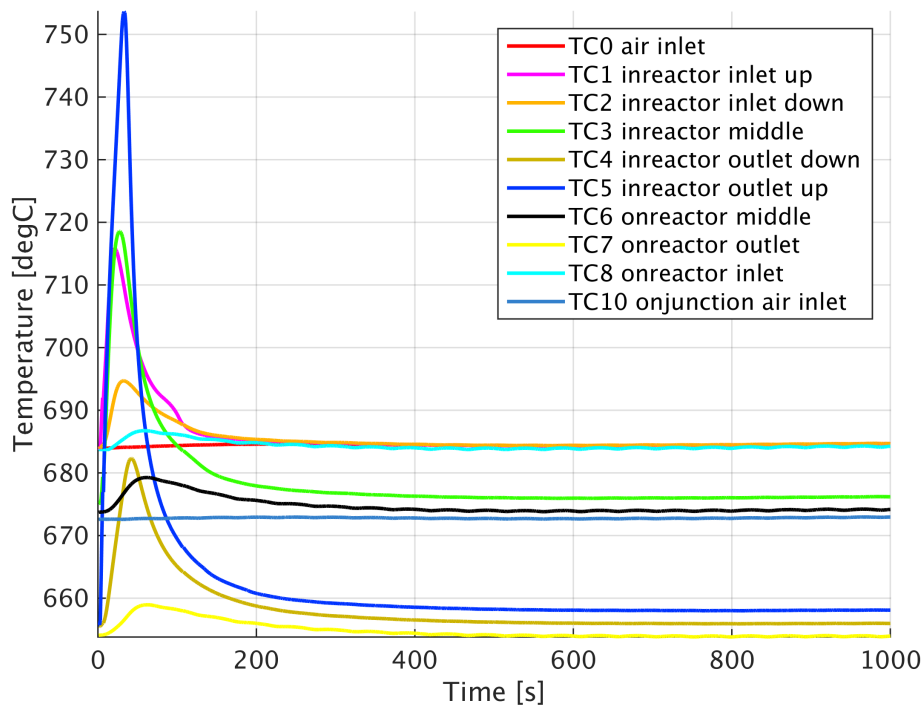


Figure I.2: Temperature during soot oxidation in experiment 3

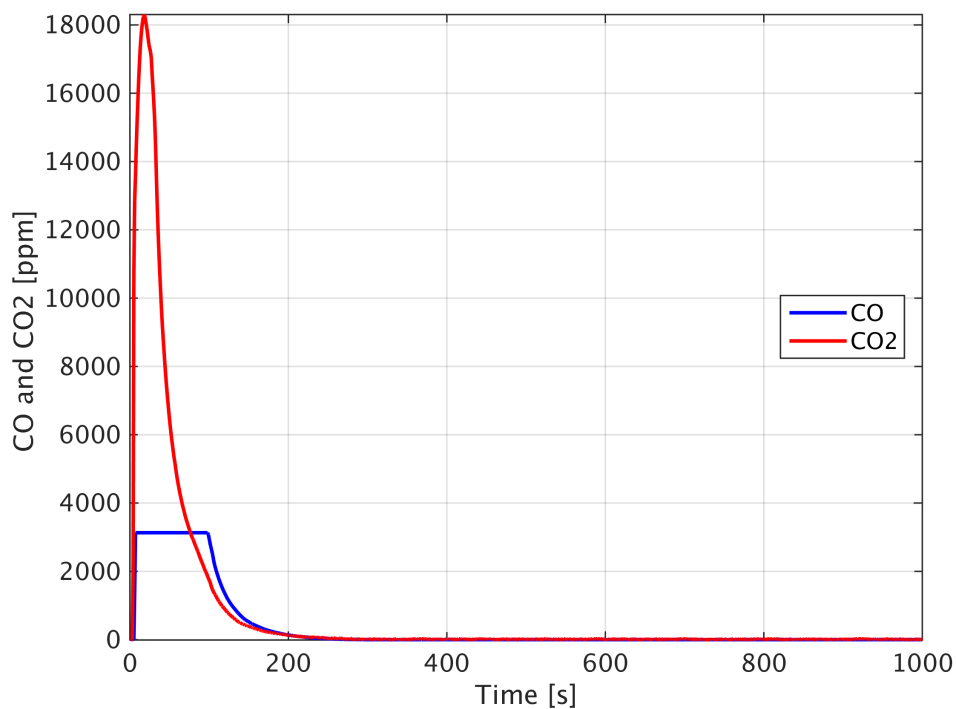


Figure I.3: CO and CO₂ during soot oxidation in experiment 3

J

Appendix J

J.1 Sherwood number calculation

Calculation of Sherwood number from CFD steady state simulation using 15vol% oxygen and soot oxidation temperature of 663.62⁰C soot oxidation temperature. In this case the concentration of oxygen at the reaction surface is assumed to be zero i.e. a very fast reaction rate is assumed. The binary gas mixture is made of nitrogen (B) that constitutes the bulk and oxygen (A).

$$D_{AB} = \frac{1.00 \times 10^{-8} T^{1.75} \left(\frac{1}{MW_A} + \frac{1}{MW_B} \right)^{1/2}}{p [(\sum \nu_A)^{1/3} + (\sum \nu_B)^{1/3}]^2} \quad (\text{J.1})$$

MW _A	MW _B	ν_O	ν_N	T	p
32g/mol	28g/mol	5.48	5.69	663.62 ⁰ C	1 bar

Since O₂ contains two oxygen atoms, the atomic volume of one oxygen atom (ν_O) is multiplied by 2 in order to calculate the atomic volume of O₂ (ν_A) as shown below:

$$\nu_A = 2x\nu_O \quad (\text{J.2})$$

The atomic volume of one nitrogen atom (ν_O) is multiplied by 2 in order to calculate the atomic volume of N₂ (ν_B) this is done since N₂ contains two nitrogen atoms.

$$\nu_B = 2x\nu_N \quad (\text{J.3})$$

$$D_{AB} = 1.152 \times 10^{-4} m^2/s \quad (\text{J.4})$$

$$N = \frac{F_{A,in} - F_{A,out}}{A_{shell}} \quad (\text{J.5})$$

$$A_{shell} = 0.153 m^2 \quad (\text{J.6})$$

J.1.1 0.7408 m/s case

$$F_{A,in} = 0.000555 X \frac{1000}{MW_A} mol/s \quad (\text{J.7})$$

$$F_{A,out} = 0.000189X \frac{1000}{MW_A} mol/s \quad (J.8)$$

$$N = 7.48 \times 10^{-2} mol/m^2s \quad (J.9)$$

$$C_{b,A} = 1.95 mol/m^3 \quad (J.10)$$

$$C_{s,A} = 0 mol/m^3 \quad (J.11)$$

$$k_c = \frac{N}{C_{b,A}} \quad (J.12)$$

$$k_c = 3.84 \times 10^{-2} m/s \quad (J.13)$$

$$Sh = \frac{k_c d_h}{D_{AB}} \quad (J.14)$$

$$Sh = 2.01 \quad (J.15)$$

J.1.2 15.3 m/s case

$$F_{A,in} = 0.0114947X \frac{1000}{MW_A} mol/s \quad (J.16)$$

$$F_{A,out} = 0.0100468X \frac{1000}{MW_A} mol/s \quad (J.17)$$

$$N = 2.96 \times 10^{-1} mol/m^2s \quad (J.18)$$

$$C_{b,A} = 1.95 mol/m^3 \quad (J.19)$$

$$C_{s,A} = 0 mol/m^3 \quad (J.20)$$

$$k_c = \frac{N}{C_{b,A}} \quad (J.21)$$

$$k_c = 1.5 \times 10^{-1} m/s \quad (J.22)$$

$$Sh = \frac{k_c d_h}{D_{AB}} \quad (J.23)$$

$$Sh = 8 \quad (J.24)$$

J.1.3 0.224 m/s case

$$F_{A,in} = 0.000167x \frac{1000}{MW_A} mol/s \quad (J.25)$$

$$F_{A,out} = 6.06 \times 10^{-6}x \frac{1000}{MW_A} mol/s \quad (J.26)$$

$$N = 0.0337 mol/m^2s \quad (J.27)$$

$$C_{b,A} = 1.95 mol/m^3 \quad (J.28)$$

$$C_{s,A} = 0 mol/m^3 \quad (J.29)$$

$$k_c = \frac{N}{C_{b,A}} \quad (J.30)$$

$$k_c = 0.0173 m/s \quad (J.31)$$

$$Sh = \frac{k_c d_h}{D_{AB}} \quad (J.32)$$

$$Sh = 0.91 \quad (J.33)$$

K

Appendix K

K.1 Space Velocity calculation for open flow case

$$SpaceVelocity = \frac{Q}{V_r} = \frac{v}{L} \quad (K.1)$$

$$v = \frac{Q}{A} \quad (K.2)$$

Q	L	H	D
3.333×10^{-05} m^3/s	0.153 m	0.012 m	0.012 m

Where L, H and D represent the length, height and depth of the reactor respectively. Q represents the volumetric flow rate at room temperature. Space Velocity = 10893.2 h^{-1}

Residence time at room temperature = $(1/\text{Space Velocity}) = 0.33 \text{ s}$